POLITECNICO DI TORINO

Department of Electronics and
Telecommunications
Master of Science in Nanotechnologies for ICTs

Master Thesis:

Full-band NEGF Analysis of Nanostructured Devices for Optoelectronics

Presented by:
Jesús Alberto González Montoya

Supervisor:
Prof. Francesco Bertazzi
Correlator:
Prof. Michele Goano

Turin, Italy
December 2018

Acknowledgments

Thanks God for giving me the opportunity to conclude this stage of my life, for giving me hope and faith in my capabilities and for giving me the strength to keep going all this way.

I would like to express my sincere gratitude to my advisor Prof. Francesco Bertazzi for offering me the opportunity to work in such an interesting field, for his continuous support and patience. He was always available to discuss my work and his guidance helped me in all the time of research and writing of this thesis. Personally I deeply appreciate his genuine interest not only in my academic work but also in my personal life.

I wish to offer my deepest gratitude to Prof. Michele Goano for his continuous support in all the problems I encountered out of the academic framework, for his friendly and valuable advices. I am grateful for the opportunity he and Prof. Bertazzi provided me, when they chose me for the research position I currently have. Special thanks also to Dr. Alberto Tibaldi, for his support with various technical issues.

Finally, I want to thank all those persons that have given me support and belief, specially to my friends and family, whose presence have filled my life with motivation, happiness and love, along with strength to move forward and achieve my goals. Thank you to my beloved Camila Ortegon, for being at my side during these two years, for her endless patience and love.

Abstract

This thesis aims to present a full-band description for the modeling and simulation of optoelectronic devices. To do this, the nonequilibrium Green's function (NEGF) formalism is used to accurately describe the quantum processes affecting carrier dynamics within the device, everything coupled through a self-consistent (SC) loop which is iterated to achieve the correct device properties under the given input conditions.

Simulation of nanoscale devices should take into account several quantum processes that dominate the device behavior at these dimensions. Consequently, quantum models have acquired such a great importance nowadays in the modeling of microelectronic and optoelectronic devices, specially in the case of LED's and solar cells, whose many problems arising from the low efficiency and losses make it imperative to understand what are the real phenomena behind them.

In order to obtain a high fidelity representation of the device behavior, the empirical tight-binding (ETB) basis is used to obtain a multi-band model of the device dispersion. This representation is essential so that one is able to simulate intra or inter-band transition due to quasi particle absorption/emission, which are some of the central phenomena involved in the operation of photo-detectors and LEDs. Subsequently, carrier dynamics are obtained in the NEGF formalism by solving the Dyson's equation of motion in steady-state conditions to obtain the device Green's function, and particle interactions are included in the device through the corresponding self-energies. Enormous complexity of the used model makes it necessary to keep a rather simple approach, including just the most important interactions to model scattering processes: electron-photon and electron-phonon interactions, being the later with both acoustic and optical phonons. It is remarkable that the self-energies included are enough to model most of the fundamental quantum phenomena in optoelectronics, like photogeneration, transport, relaxation and recombination of carriers. The Green's functions and the self-energies are then computed self consistently within the so called self-consistent Born approximation (SCBA), and the effects of coupling the device to semi-infinite contacts is taken into account using boundary self-energies.

The theory presented in this work is used to simulate different nanostructured devices which are found in literature and which allow to clearly see all the capabilities of the NEGF

formalism. In particular, three examples are considered: an AlGaAs/GaAs quantum well heterostructure, a type-two InAs/GaSb superlattice absorber, and an InAlGaAs/InGaAs interband tunnel-junction. These structures were chosen due to their rather simple configuration, which allows to perform multi-band computations within a reasonable simulation time, and due to their great importance in optoelectronic applications. Device performance is also studied by varying geometrical and simulation parameters, taking special attention to the transport mechanisms, the localization of carriers, and the formation of minibands and localized states along the device area. Finally, two different approaches were described to be implemented in future works, which will help to speed up and enhance the computational capabilities of the present implementation.

Keywords: Nonequilibrium Green's function, Empirical Tight-Binding model, $\mathbf{k \cdot p}$ model, Quantum transport, Superlattice heterostructure, Optoelectronic devices, Low rank approximation, Pulay method.

Content

Chapter 1

Introduction

In the last few decades, advances in the field of microelectronics has experienced an ever increasing tremendous development, leading to the reduced devices we see nowadays and which opens the door to hundreds of new applications. Although the dimensions of the transistors today fabricated seem to have reached a dead end at 14 nm [1], because of the proximity to the atomic dimensions and the difficulties it imposes in the processes of fabrication, continuous scientific effort have shed light to other approaches to overcome scaling limits and still achieve better device performances , e.g. 3D stacking and technology integration. Even in the field of optoelectronics, many new problems arise apart from the one imposed by miniaturization, covering the many fundamental aspects behind the physics of generating/absorbing light devices. In fact, the difficulty to easily model optical processes in complex devices has taken the attention of many researchers and industries who seek to develop reliable CAD tools able to represent accurately this devices and improve efficiency and efficacy.

In the above picture, it becomes absolutely imperative to develop reliable computational tools that help in the simulation of microelectronic devices in order to be able to really understand the physics behind them and represent the underlying phenomena with a high degree of fidelity. Quantum transport techniques come into play thanks to the developed of theories like nonequilibrium Green's (NEGF) function [2] and density matrix (DM) [3] theory, suitable for the modelling of nanostructured devices in steady state and transient regimes, respectively. It was Keldysh in 1964 [4] who fistly presented his theory of NEGF and opened the gate for this formalism to become a real computational tool. Just recently NEGF has gained such great popularity in the simulation of optoelectronic devices, since previous fabrication techniques didn't required such powerful simulation models. Recent technological processes of fabrication permitted to produce full-operative complex optoelectronic devices like quantum cascade lasers (QCL) or vertical-cavity surface-emitting lasers (VCSEL), which brought the need of realistic simulation tools.

In this work we provide a deep insight into the relevant aspects of the NEGF theory, and describe how this can be employed to simulate optoelectronic devices, specifically oriented to photo-detection applications. The theory will be presented under a multi-band approach, focusing our attention on two of the main basis models used nowadays in NEGF simulations: the $\mathbf{k} \cdot \mathbf{p}$ [5] and the tight binding basis. Both of them result very effective and accurate in describing the main features of nanostructured devices, provided the proper parameters are used to model each of the constituent materials. Other basis models like the Maximally Localized Wannier Functions [6], first introduced by *Wannier* in 1937 [7], have also evolved and become very useful in describing large, periodic nanostructures. The tight binding model results particularly interesting since its an atomistic model, hence able to provide full Brillouin zone simulations, which in turns is not possible for the $\mathbf{k} \cdot \mathbf{p}$ that is based on expansion of Bloch functions around the Brillouin zone center. This, and the fact that TB basis is orthogonal, make it a much superior method, though much more resource demanding from the simulation standpoint.

This thesis is divided up in four chapters, which are described as follows: in the second chapter, we will deal mainly with presenting most of the relevant theory that was used to develop the NEGF implementation. On the one hand, we will first present the theoretical aspects NEGF, in the Keldysh formalism, and we will derive all the main equations that will be used in the later chapters. After this, the discretization model, namely the Empirical Tight Binding (ETB), will be presented along with all the equations regarding tight-binding Hamiltonian and main device properties as computed in this basis. The $\mathbf{k} \cdot \mathbf{p}$ basis will be also presented in a brief manner, theory which will also serve to perform one example implementation.

In the third chapter, we will be concerned with the simulation of three nanostructures which will serve as examples to demonstrate the tremendous potential of the NEGF theory. First we will take a look to a simple quantum well heterostructure made of AlGaAs/GaAS, in which confined states can be used to absorb light with a well-defined wavelength. We will observe here the effect of including phonon scattering as well as photon absorption through photon scattering. An interband tunnel junction, made of InAlGaAs/AlGaAs will be also studied with special attention to the quantum effects that make possible for the electrons to travel between the contact. In particular we will observe how doping induced potential wells lead to the appearance of confined states not accessible from the contacts and which will need the help of optical phonon scattering to be accessible for carriers. We will also consider a type-two superlattice composed of GaSb/InAs, which is used as photon absorber in the mid-IR range in many optoelectonic applications. In this case we will be interested in observing how minibands are formed through the structure and how these change as we vary geometrical parameters of the nanostructure. All this simulations will be carried out with a two-band tight binding model, since the trade-off between simplicity and accuracy for this

model is sufficient for the purpose of observing the capabilities of the NEGF approach.

After this simulations, two models will be presented, aimed improve the computational capabilities of the NEGF implementation. First, we describe the reduced order model, a novel approach proposed in this work to reduce the computational size of the basis used to discretize the device Hamiltonian. In this model, NEGF equations are projected into a reduced order-basis composed by a subset of the noninteracting Hamiltonian wavefunctions. This wavefunctions are used to diagonalize the position operator in order to obtain maximally localized, orthogonal basis functions. Wavefunctions not included in the new basis are accounted in an effective way by means of an extra self-energy term. In the second part, we will show how to apply the Pulay method, also known as Direct Inversion in the Iterative Subspace, in order improve the convergence of the inner loop. The main motivation of this is to employ it in devices in which achieving convergence of the inner loop is particularly slow and difficult, like is the case of the tunnel junction in the previous examples.

Chapter 2

Nonequilibrium Green's Function Device Simulation

Device simulations at nanoscale dimension should take into account several quantum processes that occur at this dimensions and dominate the behavior of the device. Classical models like the drift-diffusion give a good insight into the device performance, but lack the capability to reproduce important quantum phenomena like light absorption, or Auger processes, which are very important in order to simulate devices like LEDs or photodetectors. In order to improve this deficiencies, quantum models need to be implemented, which are capable of solving the Schrödinger equation and extract important quantities as statistical average properties of the device. In this chapter, we will review the basic theory concerning the Nonequilibrium Green's Function approach for device transport simulation, and we will derive expressions to obtain physical quantities such as carrier densities and current density.

2.1. Contour-ordered nonequilibrium Green's function

We start this chapter by considering a system described by the Hamiltonian

$$\hat{\mathcal{H}} = \hat{H} + \hat{H}^{ext}(t) = \hat{H}_0 + \hat{H}^i + \hat{H}^{ext}(t), \tag{2-1}$$

where the time-independent Hamiltonian $\hat{H} = \hat{H}_0 + \hat{H}^i$ describes the isolated system, $\hat{H}_0$ is the simple part that contains the lattice and the electrostatic potential, and $\hat{H}^i$ is the complicated part inter-particle interactions. On the other hand, $\hat{H}^{ext}(t)$ is a time-dependent perturbation that drives the system out of equilibrium, applied at times $t > t_0$, and that could be, e.g., an electric field, a light excitation pulse, or an imbalance of the chemical potentials of the reservoirs coupled to the system.

The properties of the system can be described by means of the single-particle nonequilibrium

Green's function, which is defined as the nonequilibrium ensemble average of contour-ordered field operators [8]

$$\begin{aligned} G(\mathbf{r},t;\mathbf{r}',t') &= -\frac{i}{\hbar}\langle \hat{T}_C\{\hat{\Psi}_{\mathcal{H}}(\mathbf{r},t)\hat{\Psi}^{\dagger}_{\mathcal{H}}(\mathbf{r}',t')\}\rangle \\ &= -\frac{i}{\hbar}\left(\theta_C(t,t')\langle\hat{\Psi}_{\mathcal{H}}(\mathbf{r},t)\hat{\Psi}^{\dagger}_{\mathcal{H}}(\mathbf{r}',t')\rangle \mp \theta_C(t',t)\langle\hat{\Psi}^{\dagger}_{\mathcal{H}}(\mathbf{r}',t')\hat{\Psi}_{\mathcal{H}}(r,t)\rangle\right), \end{aligned} \tag{2-2}$$

where the function $\theta_C(t,t')$ is the Heaviside step function defined on the contour C,

$$\theta_C(t,t') = \begin{cases} 1 & \text{if } t \text{ later on } C \\ 0 & \text{otherwise} \end{cases} \tag{2-3}$$

and $\hat{\Psi}_{\mathcal{H}}(\mathbf{r},t)$ ($\hat{\Psi}^{\dagger}_{\mathcal{H}}(\mathbf{r}',t')$) is the field operator in the Heisenberg picture, that annihilates (creates) a particle at position $\mathbf{r}$ ($\mathbf{r}'$) and at time t (t'). The minus (plus) sign stands for fermions (bosons).

Expanding the average [9] provides the starting point of the perturbation expansion of the nonequilibrium Green's function[1]

$$G(\mathbf{r},t;\mathbf{r}',t') = -\frac{i}{\hbar}\frac{\langle \hat{T}_{\tilde{C}}\left\{\exp\left[-\frac{i}{\hbar}\int_{\tilde{C}} d\tau \hat{H}^{i}_{H_0}(\tau)\right]\exp\left[-\frac{i}{\hbar}\int_{\tilde{C}} d\tau \hat{H}^{ext}_{H_0}(\tau)\right]\hat{\Psi}_{H_0}(\mathbf{r},t)\hat{\Psi}^{\dagger}_{H_0}(\mathbf{r}',t')\right\}\rangle_0}{\langle \hat{T}_{\tilde{C}}\left\{\exp\left[-\frac{i}{\hbar}\int_{\tilde{C}} d\tau \hat{H}^{i}_{H_0}(\tau)\right]\exp\left[-\frac{i}{\hbar}\int_{\tilde{C}} d\tau \hat{H}^{ext}_{H_0}(\tau)\right]\right\}\rangle_0}, \tag{2-4}$$

where now all the quantities are expressed in the interaction picture, as indicated by the subscript H_0. Since we are just interested in the steady-state of the system, initial correlations will be neglected and the integrals will be taken over the Schwinger-Keldysh contour $\tilde{C} \approx C = C_t \cup C_{\bar{t}}$ [10], which is shown in figure **2-1**.

The main goal is to derive the equations of motion of $G(\mathbf{r},t;\mathbf{r}',t')$ with respect to the times t and t', for which we will consider a Hamiltonian $\mathcal{H}$ with carrier-carrier interaction $\hat{H}^{i} = \hat{V}$, and a single-particle potential $\hat{H}^{ext} = \hat{U}$, which in second quantization reads

$$\begin{aligned} \hat{\mathcal{H}}(t) &= \int d\mathbf{r}\, \hat{\Psi}^{\dagger}_{\mathcal{H}}(\mathbf{r},t)[H_0(\mathbf{r}) + U(\mathbf{r},t)]\hat{\Psi}_{\mathcal{H}}(\mathbf{r},t) \\ &+\frac{1}{2}\int d\mathbf{r}\int d\mathbf{r}'\hat{\Psi}^{\dagger}_{\mathcal{H}}(\mathbf{r},t)\hat{\Psi}^{\dagger}_{\mathcal{H}}(\mathbf{r}',t)V(\mathbf{r}-\mathbf{r}')\hat{\Psi}_{\mathcal{H}}(\mathbf{r}',t)\hat{\Psi}_{\mathcal{H}}(\mathbf{r},t). \end{aligned} \tag{2-5}$$

[1] This formula results from moving field operators in (2-2) from the Heisenberg to the interaction picture. This is performed by multiplying the operators by the propagators observed in (2-4), which depend on the interaction part of the Hamiltonian. A more detailed derivation is presented in [10].

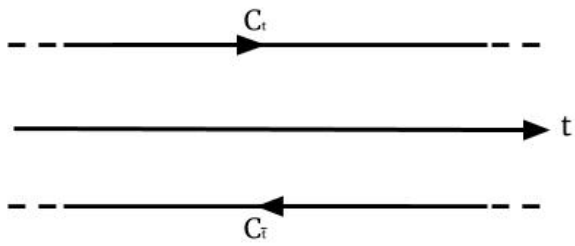

Figure 2-1: *The Schwinger-Keldysh contour, composed by the chronological* $C_t = (-\infty, \infty)$ *and antichronological* $C_{\bar{t}} = (\infty, -\infty)$ *branches. Small shift from real axis is just to distinguish the integration direction.*

This representation of the Hamiltonian is called *normal-ordered*, i.e., all annihilation operators appear to the right of any creation operator. Taking into account the anti-commutation property

$$\left[\hat{\Psi}_{\mathcal{H}}(\mathbf{r},t), \hat{\Psi}^{\dagger}_{\mathcal{H}}(\mathbf{r}',t)\right]_{+} = \delta(\mathbf{r}-\mathbf{r}'), \tag{2-6}$$

the time derivative of the contour-ordered pair of Heisenberg field operators is

$$\begin{aligned}\frac{\partial}{\partial t}\langle \hat{T}_C\{\hat{\Psi}_{\mathcal{H}}(\mathbf{r},t)\hat{\Psi}^{\dagger}_{\mathcal{H}}(\mathbf{r}',t')\}\rangle &= \left\langle \hat{T}_C\left\{\left[\frac{\partial}{\partial t}\hat{\Psi}_{\mathcal{H}}(\mathbf{r},t)\right]\hat{\Psi}^{\dagger}_{\mathcal{H}}(\mathbf{r}',t')\right\}\right\rangle + \delta_C(t,t')\left[\hat{\Psi}_{\mathcal{H}}(\mathbf{r},t)\hat{\Psi}^{\dagger}_{\mathcal{H}}(\mathbf{r}',t')\right]_{+} \\ &= \left\langle \hat{T}_C\left\{\left[\frac{\partial}{\partial t}\hat{\Psi}_{\mathcal{H}}(\mathbf{r},t)\right]\hat{\Psi}^{\dagger}_{\mathcal{H}}(\mathbf{r}',t')\right\}\right\rangle + \delta_C(t,t')\delta(\mathbf{r}-\mathbf{r}'). \end{aligned} \tag{2-7}$$

The time derivative of the annihilation operator can be derived from the corresponding Heisenberg equation of motion

$$\begin{aligned} i\hbar\frac{\partial}{\partial t}\hat{\Psi}_{\mathcal{H}}(\mathbf{r},t) &= \left[\hat{\Psi}_{\mathcal{H}}(\mathbf{r},t), \hat{\mathcal{H}}(t)\right]_{-} \\ &= [H_0(\mathbf{r}) + U(\mathbf{r},t)]\hat{\Psi}_{\mathcal{H}}(\mathbf{r},t) + \int d\mathbf{r}' V(\mathbf{r}-\mathbf{r}')\hat{\Psi}^{\dagger}_{\mathcal{H}}(\mathbf{r}',t)\hat{\Psi}_{\mathcal{H}}(\mathbf{r}',t)\hat{\Psi}_{\mathcal{H}}(\mathbf{r},t) \end{aligned} \tag{2-8}$$

Replacing in (2-7) the time derivative (2-8) gives the equation of motion of the Green's function relative to t_1 (a similar procedure gives the derivative relative to $t_{1'}$)

$$\left[i\hbar\frac{\partial}{\partial t_1} - H_0(\mathbf{r}_1) - U(1)\right] G(11') = \delta(11') - i\hbar\int_C d2V(1-2)G^{(2)}(121'2^{+}) \tag{2-9a}$$

$$\left[-i\hbar\frac{\partial}{\partial t_{1'}} - H_0(\mathbf{r}) - U(1')\right] G(11') = \delta(11') - i\hbar\int_C d2V(1'-2)G^{(2)}(12^{-}1'2) \tag{2-9b}$$

where the two-particle Green's function is defined as

$$G^{(2)}(121'2') = \left(-\frac{i}{\hbar}\right)^2 \left\langle \hat{T}_C\{\hat{\Psi}_{\mathcal{H}}(1)\hat{\Psi}_{\mathcal{H}}(2)\hat{\Psi}^{\dagger}_{\mathcal{H}}(2')\hat{\Psi}^{\dagger}_{\mathcal{H}}(1')\}\right\rangle, \tag{2-10}$$

and the notation $2^{\pm}$ stands for a time argument of $\hat{\Psi}^{\dagger}_{\mathcal{H}}(2)$ infinitesimally larger or smaller than t_2 [11]. In equation (2-9), we have also used the short-hand notation $G(\mathbf{r}_1, t_1; \mathbf{r}_{1'}, t_{1'}) = G(11')$, $\int_C d1 = \int_C dt_1 \int d\mathbf{r}_1$, and

$$\delta(12) = \delta_C(t_1, t_2)\delta(\mathbf{r}_1 - \mathbf{r}_2) \tag{2-11}$$

$$V(1-2) = V(\mathbf{r}_1 - \mathbf{r}_2)\delta(t_1 - t_2). \tag{2-12}$$

Equation (2-9) present an infinite hierarchy of coupled equations involving Green's Functions of ever increasing order, hence presenting a problem in the direct evaluation of the dynamics of the Green's function. However, this hierarchy approach can be avoided by approximating the two-particle Green's function by means of the self-energy $\Sigma(11')$ encoding interaction effects of all particles on the single-particle dynamics

$$\left[i\hbar\frac{\partial}{\partial t_1} - H_0(\mathbf{r}) - U(1)\right] G(11') = \delta(11') + \int_C d3\Sigma(13)G(31') \tag{2-13a}$$

$$\left[-i\hbar\frac{\partial}{\partial t_{1'}} - H_0(\mathbf{r}') - U(1')\right] G(11') = \delta(11') + \int_C d3G(13)\Sigma(31'). \tag{2-13b}$$

The self-energy may be obtained to different levels of approximations by a perturbative expansion of the exponential terms in equation (2-4), where the help of Feynman diagrammatic description of the resulting equations result in a simple an natural way to arrive to the formal derivation of the self-energy term. Finally, integrating over one of the times to eliminate the δ functions, results in integral form of the Dyson's equations

$$G(11') = G_0(11') + \int_C d2 \int_C d3\, G_0(12)\Sigma(23)G(31') \tag{2-14a}$$

$$G(11') = G_0(11') + \int_C d2 \int_C d3\, G(12)\Sigma(23)G_0(31'), \tag{2-14b}$$

where

$$G_0(11') = \left[i\hbar\frac{\partial}{\partial t_1} - H_0(\mathbf{r}) - U(1)\right]^{-1} \delta(11'), \tag{2-15}$$

is the noninteracting Green's function.

2.1.1. Analytic Continuation

Difficulties arising from the complex contour integration in the Green's function definition are overcome by defining $G(11')$ as a piecewise analytic function of four new Green's functions with real-time arguments

$$G(11') = -\frac{i}{\hbar}\langle \hat{T}_C\{\hat{\psi}_{\mathcal{H}}(1)\hat{\psi}^{\dagger}_{\mathcal{H}}(1')\}\rangle = \begin{cases} G^{t}(11') & t_1, t_{1'} \in C_t \\ G^{\bar{t}}(11') & t_1, t_{1'} \in C_{\bar{t}} \\ G^{<}(11') & t_1 \in C_t, t_{1'} \in C_{\bar{t}} \\ G^{>}(11') & t_1 \in C_{\bar{t}}, t_{1'} \in C_t \end{cases} \tag{2-16}$$

which are named the chronological, antichronological, lesser, and greater Green's functions, respectively, and are defined by

$$G^{t}(11') = -\frac{i}{\hbar}\langle \hat{T}_t\{\hat{\Psi}_{\mathcal{H}}(1)\hat{\Psi}^{\dagger}_{\mathcal{H}}(1')\}\rangle \tag{2-17}$$

$$G^{\bar{t}}(11') = -\frac{i}{\hbar}\langle \hat{T}_{\bar{t}}\{\hat{\Psi}_{\mathcal{H}}(1)\hat{\Psi}^{\dagger}_{\mathcal{H}}(1')\}\rangle \tag{2-18}$$

$$G^{<}(11') = +\frac{i}{\hbar}\langle \hat{\Psi}^{\dagger}_{\mathcal{H}}(1')\hat{\Psi}_{\mathcal{H}}(1)\rangle \tag{2-19}$$

$$G^{>}(11') = -\frac{i}{\hbar}\langle \hat{\Psi}_{\mathcal{H}}(1)\hat{\Psi}^{\dagger}_{\mathcal{H}}(1')\rangle \tag{2-20}$$

The chronological and antichronological Green's functions are usually replaced by the retarded and advanced Green's functions

$$G^{R}(11') = \theta(t-t')[G^{>}(11') - G^{<}(11')] \tag{2-21}$$

$$G^{A}(11') = -\theta(t'-t)[G^{>}(11') - G^{<}(11')] \tag{2-22}$$

Subtracting the last two equations, we have

$$G^{R}(11') - G^{A}(11') = G^{>}(11') - G^{<}(11'), \tag{2-23}$$

which shows that only three of the Green's functions are linearly independent. Equations of motion for the above Green's function can be derived by means of the Langreth rules [12] applied to the contour integrals in (2-14)

$$D^{R(A)}(t_1,t_2) = \int_{-\infty}^{+\infty} d\tau_1 \int_{-\infty}^{+\infty} d\tau_2\, A^{R(A)}(t_1,\tau_1)B^{R(A)}(\tau_1,\tau_2)C^{R(A)}(\tau_2,t_2) \tag{2-24}$$

$$\begin{aligned} D^{\lessgtr}(t_1,t_2) = \int_{-\infty}^{+\infty} d\tau_1 \int_{-\infty}^{+\infty} d\tau_2\, [&A^{R}(t_1,\tau)B^{R}(\tau,t_2)C^{\lessgtr}(\tau,t_2) \\ &+ A^{R}(t_1,\tau)B^{\lessgtr}(\tau,t_2)C^{A}(\tau,t_2) + A^{\lessgtr}(t_1,\tau)B^{A}(\tau,t_2)C^{A}(\tau,t_2)], \end{aligned} \tag{2-25}$$

leading to the equations of motion of the real-time Green's functions[2]

$$G^{R(A)}(11') = G_0^{R(A)}(11') + \int d2 \int d3 G_0^{R(A)}(12)\Sigma^{R(A)}(23)G^{R(A)}(3,1') \tag{2-26}$$

$$G^{\lessgtr}(11') = \int d2 \int d3 G^{R}(12)\Sigma^{\lessgtr}(23)G^{A}(31'), \tag{2-27}$$

with

$$\int d1 = \int d\mathbf{r}_1 \int_{-\infty}^{+\infty} dt_1. \tag{2-28}$$

2.1.2. Steady-state formulation

For steady-state calculations, only the time difference $\tau = t - t'$ is meaningful. Hence, assuming a steady state time dependence of the Green's functions $G^\alpha(\mathbf{r}, t; \mathbf{r}', t') = G^\alpha(\mathbf{r}; \mathbf{r}', t - t')$ and Fourier transforming $O^\alpha = G^\alpha, \Sigma^\alpha$ $(\alpha = R, A, <, >)$ to energy coordinates

$$O^\alpha(\mathbf{r}_1, \mathbf{r}_2, E) = \int_{-\infty}^{+\infty} d\tau e^{\frac{i}{\hbar}E\tau} O^\alpha(\mathbf{r}_1, \mathbf{r}_2, \tau) \tag{2-29}$$

$$O^\alpha(\mathbf{r}_1, \mathbf{r}_2, \tau) = \frac{1}{2\pi\hbar} \int_{-\infty}^{+\infty} dE e^{-\frac{i}{\hbar}E\tau} O^\alpha(\mathbf{r}_1, \mathbf{r}_2, E), \tag{2-30}$$

leads to the steady state representation of the Green's functions

$$G^{\lessgtr}(\mathbf{r}_1, \mathbf{r}_{1'}, E) = \int d\mathbf{r}_2 \int d\mathbf{r}_3\, G^R(\mathbf{r}_1, \mathbf{r}_2, E)\Sigma^{\lessgtr}(\mathbf{r}_2, \mathbf{r}_3, E)G^A(\mathbf{r}_3, \mathbf{r}_{1'}, E) \tag{2-31a}$$

$$\begin{aligned} G^{R(A)}(\mathbf{r}_1, \mathbf{r}_{1'}, E) &= G_0^{R(A)}(\mathbf{r}_1, \mathbf{r}_{1'}, E) \\ &+ \int d\mathbf{r}_2 \int d\mathbf{r}_3 G_0^{R(A)}(\mathbf{r}_1, \mathbf{r}_2, E)\Sigma^{R(A)}(\mathbf{r}_2, \mathbf{r}_3, E)G^{R(A)}(\mathbf{r}_3, \mathbf{r}_{1'}, E), \end{aligned} \tag{2-31b}$$

with the noninteracting Green function given by

$$G_0^{R(A)}(\mathbf{r}_1, \mathbf{r}_{1'}, E) = [E + (-)i\eta - H_0(r_1)]^{-1}\delta(\mathbf{r}_1 - \mathbf{r}_{1'}). \tag{2-32}$$

The small $\eta \to 0^+$ parameter provides the correct analytical properties. Time reversal symmetry implies

[2] In the case of $G^{\lessgtr}$ some terms have been neglected, as can be seen when comparing (2-25) with (2-27). It can be demonstrated that these extra terms vanish for steady-state systems. Thus, in general keeping the shown term is usually sufficient. More information can be found in [12].

$$G^R(\mathbf{r}_1, \mathbf{r}_{1'}, E) = [G^A(\mathbf{r}_1, \mathbf{r}_{1'}, E)]^\dagger, \tag{2-33a}$$
$$G^{\lessgtr}(\mathbf{r}_1, \mathbf{r}_{1'}, E) = -[G^{\lessgtr}(\mathbf{r}_1, \mathbf{r}_{1'}, E)]^\dagger, \tag{2-33b}$$

which reduces the number of independent Green's functions to two.

2.2. Spatial discretization

Given a suitable finite basis $\{\phi_\nu(\mathbf{r}, \sigma)\}$, characterized by a set of quantum numbers ν, the Green's function needs to be discretized in order to numerically evaluate the Dyson's equation. This is obtained by expanding the field operators as linear combination of the given basis,

$$\hat{\Psi}_{\mathcal{H}}(\mathbf{r}, t) = \sum_\nu \phi_\nu(\mathbf{r}, \sigma)\hat{c}_\nu(t) \tag{2-34a}$$
$$\hat{\Psi}^\dagger_{\mathcal{H}}(\mathbf{r}, t) = \sum_\nu \phi^*_\nu(\mathbf{r}, \sigma)\hat{c}^\dagger_\nu(t) \tag{2-34b}$$

which leads to two representations of the discrete Green's function. On one hand, the *contravariant* representation in steady state conditions, is defined by the matrix $\mathbf{G} = \{G_{\nu,\mu}(E)\}$, such that

$$G(\mathbf{r}, \mathbf{r}'; E) = \sum_{\nu,\mu} \phi_\nu(\mathbf{r}, \sigma)G_{\nu,\mu}(E)\phi^*_\mu(\mathbf{r}', \sigma). \tag{2-35}$$

On the other hand, the *covariant* representation is given by the matrix $\tilde{\mathbf{G}} = \{\tilde{G}_{\nu,\mu}(E)\}$, such that

$$\tilde{G}_{\nu,\mu}(E) = \int d\mathbf{r} \int d\mathbf{r}' \phi^*_\nu(\mathbf{r}, \sigma)G(\mathbf{r}, \mathbf{r}'; E)\phi_\mu(\mathbf{r}', \sigma), \tag{2-36}$$

where both representations are related by the following equivalence, in matrix notation

$$\tilde{\mathbf{G}} = \mathbf{MGM}. \tag{2-37}$$

The same definitions are used to represent the self-energy $\Sigma(\mathbf{r}, \mathbf{r}'; E)$ in contravariant ($\mathbf{\Sigma}$) and covariant representation ($\tilde{\mathbf{\Sigma}}$). The matrix $\mathbf{M} = \{M_{\nu,\mu}\}$ is called the *overlap matrix*, and its given by

$$M_{\nu,\mu} = \int d\mathbf{r}\phi^*_\nu(\mathbf{r}, \sigma)\phi_\mu(\mathbf{r}, \sigma). \tag{2-38}$$

It is clear that, in the case of a orthonormal basis, the matrix $\mathbf{M}$ is the identity matrix and both representations of the Green's function are equivalent. As we will see later, this is the

case of the tight binding method, in which this feature brings the advantage of simplifying equations and reducing the number of matrix multiplications.

To derive the quantum kinetic equation in discrete form, we start from the steady state Dyson's equation for the retarded Green's function (2-31b), and using (2-35) we obtain,

$$\begin{aligned}
\sum_{\nu,\mu}\phi_\nu(\mathbf{r},\sigma)G^R_{\nu,\mu}(E)\phi^*_\mu(\mathbf{r}',\sigma) &= \sum_{\nu,\mu}\phi_\nu(\mathbf{r},\sigma)\{\mathbf{G}^R_0\}_{\nu,\mu}(E)\phi^*_\mu(\mathbf{r}',\sigma)\\
&+\int d\mathbf{r}_2\int d\mathbf{r}_3\sum_{\nu_1,\mu_1}\phi_{\nu_1}(\mathbf{r},\sigma)\{\mathbf{G}^R_0\}_{\nu_1,\mu_1}(E)\phi^*_{\mu_1}(\mathbf{r}_2,\sigma)\\
&\times\sum_{\nu_2,\mu_2}\phi_{\nu_2}(\mathbf{r}_2,\sigma)\Sigma^R_{\nu_2,\mu_2}(E)\phi^*_{\mu_2}(\mathbf{r}_3,\sigma)\\
&\times\sum_{\nu_3,\mu_3}\phi_{\nu_3}(\mathbf{r}_3,\sigma)G^R_{\nu_3,\mu_3}(E)\phi^*_{\mu_3}(\mathbf{r}',\sigma) \qquad (2\text{-}39)\\
&=\sum_{\nu,\mu}\phi_\nu(\mathbf{r},\sigma)\{\mathbf{G}^R_0\}_{\nu,\mu}(E)\phi^*_\mu(\mathbf{r}',\sigma)\\
&+\sum_{\nu_1,\mu_1}\sum_{\nu_2,\mu_2}\sum_{\nu_3,\mu_3}\phi_{\nu_1}(\mathbf{r},\sigma)\{\mathbf{G}^R_0\}_{\nu_1,\mu_1}(E)\Sigma^R_{\nu_2,\mu_2}(E)G^R_{\nu_3,\mu_3}(E)\phi^*_{\mu_3}(\mathbf{r}',\sigma)\\
&\times\underbrace{\int d\mathbf{r}_2\phi^*_{\mu_1}(\mathbf{r}_2,\sigma)\phi_{\nu_2}(\mathbf{r}_2,\sigma)}_{M_{\mu_1,\nu_2}}\underbrace{\int d\mathbf{r}_3\phi^*_{\mu_2}(\mathbf{r}_3,\sigma)\phi_{\nu_3}(\mathbf{r}_3,\sigma)}_{M_{\mu_2,\nu_3}} \qquad (2\text{-}40)\\
&=\sum_{\nu,\mu}\phi_\nu(\mathbf{r},\sigma)\{\mathbf{G}^R_0\}_{\nu,\mu}(E)\phi^*_\mu(\mathbf{r}',\sigma)+\sum_{\nu_1,\mu_1}\sum_{\nu_3,\mu_3}\phi_{\nu_1}(\mathbf{r},\sigma)\{\mathbf{G}^R_0\}_{\nu_1,\mu_1}(E)\\
&\times\underbrace{\left(\sum_{\nu_2,\mu_2}M_{\mu_1,\nu_2}\Sigma^R_{\nu_2,\mu_2}(E)M_{\mu_2,\nu_3}\right)}_{\tilde{\Sigma}_{\mu_1,\nu_3}(E)}G^R_{\nu_3,\mu_3}(E)\phi^*_{\mu_3}(\mathbf{r}',\sigma) \qquad (2\text{-}41)\\
&=\sum_{\nu,\mu}\phi_\nu(\mathbf{r},\sigma)\left\{\mathbf{G}^R_0(E)+\mathbf{G}^R_0(E)\tilde{\mathbf{\Sigma}}(E)\mathbf{G}^R(E)\right\}_{\nu,\mu}\phi^*_\mu(\mathbf{r}',\sigma)\\
&\qquad (2\text{-}42)
\end{aligned}$$

yielding the matrix equation,

$$\mathbf{G}^R(E)=\mathbf{G}^R_0(E)+\mathbf{G}^R_0(E)\tilde{\mathbf{\Sigma}}(E)\mathbf{G}^R(E) \qquad (2\text{-}43)$$

which is equivalent to,

$$[\{\mathbf{G}^R_0(E)\}^{-1}-\tilde{\mathbf{\Sigma}}(E)]\mathbf{G}^R(E)=\mathbb{1}. \qquad (2\text{-}44)$$

In a similar way, the discrete kinetic equation for the correlation functions can be obtained from (2-31a), yielding the Keldysh equation in its discretized form

$$\mathbf{G}^{\lessgtr}(E) = \mathbf{G}^{R}(E)\tilde{\mathbf{\Sigma}}^{\lessgtr}(E)\mathbf{G}^{A}(E) \tag{2-45}$$

with the noninteracting Green's function given by,

$$\mathbf{G}_0^R(E) = [E\mathbf{M} - \mathbf{H}]^{-1} \tag{2-46a}$$

$$\{\mathbf{H}\}_{\nu,\mu} = \int d\mathbf{r}\phi_\nu^*(\mathbf{r},\sigma)H(\mathbf{r})\phi_\mu(\mathbf{r},\sigma) \tag{2-46b}$$

The fluctuation-dissipation theorem allows us to relate all Green's functions in equilibrium conditions

$$\mathbf{G}^{<}(E) = if_{FD}(E - E_F)\mathbf{A}(E) \tag{2-47a}$$

$$\mathbf{G}^{>}(E) = i[f_{FD}(E - E_F) - 1]\mathbf{A}(E) \tag{2-47b}$$

where

$$\mathbf{A}(E) = i[\mathbf{G}^R(E) - \mathbf{G}^A(E)] = i[\mathbf{G}^>(E) - \mathbf{G}^<(E)] \tag{2-48}$$

is the spectral function, and f_{FD} is the Fermi-Dirac distribution. A similar expression holds for the self-energies

$$\mathbf{\Sigma}^{<}(E) = if_{FD}(E - E_F)\mathbf{\Gamma}(E) \tag{2-49a}$$

$$\mathbf{\Sigma}^{>}(E) = i[f_{FD}(E - E_F) - 1]\mathbf{\Gamma}(E) \tag{2-49b}$$

where

$$\mathbf{\Gamma}(E) = i[\mathbf{\Sigma}^R(E) - \mathbf{\Sigma}^A(E)] = i[\mathbf{\Sigma}^>(E) - \mathbf{\Sigma}^<(E)] \tag{2-50}$$

is the broadening function. From now on, for simplicity we will use $\mathbf{\Sigma}$ to refer to the covariant representation of the self-energy, unless the contrary is stated.

2.3. Physical observables from NEGF

For a generic one-body operator $O(\mathbf{r},t) = \{O_{\sigma,\sigma'}(\mathbf{r},t)\}$ expressed in second quantization notation

$$\hat{\mathcal{O}}(\mathbf{r},t) = \sum_{\sigma,\sigma'} \hat{\Psi}^\dagger_{\mathcal{H}}(\mathbf{r},t,\sigma)O_{\sigma,\sigma'}(\mathbf{r},t)\hat{\Psi}_{\mathcal{H}}(\mathbf{r},t,\sigma'), \tag{2-51}$$

the ensemble average can be written as

$$\begin{aligned}\langle\hat{\mathcal{O}}(\mathbf{r},t)\rangle &= \mathrm{Tr}[\hat{\rho}\hat{\mathcal{O}}(\mathbf{r},t)] \\ &= \sum_{\sigma,\sigma'} \mathrm{Tr}[\hat{\rho}\hat{\Psi}^{\dagger}_{\mathcal{H}}(\mathbf{r},t,\sigma)O_{\sigma,\sigma'}(\mathbf{r},t)\hat{\Psi}_{\mathcal{H}}(\mathbf{r},t,\sigma')] \\ &= \lim_{\mathbf{r}'\to\mathbf{r}}\lim_{t'\to t^+}\sum_{\sigma,\sigma'} O_{\sigma,\sigma'}(\mathbf{r},t)\mathrm{Tr}[\hat{\rho}\hat{\Psi}^{\dagger}_{\mathcal{H}}(\mathbf{r}',t',\sigma)\hat{\Psi}_{\mathcal{H}}(\mathbf{r},t,\sigma')] \\ &= \lim_{\mathbf{r}'\to\mathbf{r}}\lim_{t'\to t^+}\sum_{\sigma,\sigma'} O_{\sigma,\sigma'}(\mathbf{r},t)\langle\hat{\Psi}^{\dagger}_{\mathcal{H}}(\mathbf{r}',t',\sigma)\hat{\Psi}_{\mathcal{H}}(\mathbf{r},t,\sigma')\rangle \\ &= -i\hbar\lim_{\mathbf{r}'\to\mathbf{r}}\lim_{t'\to t^+}\mathrm{Tr}[O(\mathbf{r},t)G^{<}(\mathbf{r},t;\mathbf{r}',t')] \end{aligned} \tag{2-52}$$

where in the last line, the trace is taken over spin indices.

2.3.1. Carrier densities

Taking the particle number operator in second quantization notation,

$$\hat{n}(\mathbf{r},t) = \sum_{\sigma}\hat{\Psi}^{\dagger}_{\mathcal{H}}(\mathbf{r},t,\sigma)\hat{\Psi}_{\mathcal{H}}(\mathbf{r},t,\sigma) \tag{2-53}$$

the average particle density at position $\mathbf{r}$ and time t is given by,

$$\begin{aligned} n(\mathbf{r},t) &= \langle\hat{n}(\mathbf{r},t)\rangle \\ &= \sum_{\sigma}\langle\hat{\Psi}^{\dagger}_{\mathcal{H}}(\mathbf{r},t,\sigma)\hat{\Psi}_{\mathcal{H}}(\mathbf{r},t,\sigma)\rangle \\ &= -i\hbar\lim_{\mathbf{r}'\to\mathbf{r}}\lim_{t'\to t^+}\sum_{\sigma} G^{<}_{\sigma,\sigma}(\mathbf{r},t;\mathbf{r}',t'). \end{aligned} \tag{2-54}$$

In steady state conditions, the Green's function can be Fourier transformed with respect to the time difference $t-t'$, yielding

$$\begin{aligned} n(\mathbf{r}) &= -i\hbar\lim_{\mathbf{r}'\to\mathbf{r}}\lim_{t'\to t^+}\sum_{\sigma} G^{<}_{\sigma,\sigma}(\mathbf{r},\mathbf{r}';t-t') \\ &= -i\hbar\lim_{\mathbf{r}'\to\mathbf{r}}\lim_{t'\to t^+}\sum_{\sigma}\int\frac{dE}{2\pi\hbar}e^{i\frac{E}{\hbar}(t-t')}G^{<}_{\sigma,\sigma}(\mathbf{r},\mathbf{r}';E) \\ &= -i\sum_{\sigma}\int\frac{dE}{2\pi}G^{<}_{\sigma,\sigma}(\mathbf{r},\mathbf{r};E). \end{aligned} \tag{2-55}$$

Similarly, for the holes we can write

$$p(\mathbf{r}) = i\sum_{\sigma}\int\frac{dE}{2\pi}G^{>}_{\sigma,\sigma}(\mathbf{r},\mathbf{r};E). \tag{2-56}$$

2.3.2. Local density of states

From the equilibrium relation (2-47a), equation (2-55) for the electron density can be written as

$$n(\mathbf{r}) = \sum_{\sigma} \int \frac{dE}{2\pi} f_{FD}(E - E_F) A_{\sigma,\sigma}(\mathbf{r}, \mathbf{r}; E), \tag{2-57}$$

hence defining the local density of states (LDOS) in the following way

$$LDOS(\mathbf{r}, E) = \frac{1}{2\pi} \sum_{\sigma} A_{\sigma,\sigma}(\mathbf{r}, \mathbf{r}; E), \tag{2-58}$$

where $A(\mathbf{r}, \mathbf{r}; E)$ is the spectral function as defined in equation (2-48).

2.3.3. Current

Starting from the Dyson's equation, it is possible to derive an expression for the current density. Here, we recall just the result, as presented in [10] for the steady state current density

$$J(\mathbf{r}) = \lim_{\mathbf{r}' \to \mathbf{r}} \frac{i}{2} [\mathbf{v}(\mathbf{r}') - \mathbf{v}(\mathbf{r})] \sum_{\sigma} \int \frac{dE}{2\pi} G^{<}_{\sigma,\sigma}(\mathbf{r}, \mathbf{r}'; E), \tag{2-59}$$

where $\mathbf{v}(\mathbf{r}) = -\frac{i}{\hbar}[\mathbf{r}, H]$ is the velocity, and the current divergence

$$\begin{aligned} \nabla \cdot J(\mathbf{r}) = -\int \frac{dE}{2\pi\hbar} \int d\mathbf{r}' \mathrm{Tr}[&\Sigma^R(\mathbf{r}, \mathbf{r}'; E) G^<(\mathbf{r}', \mathbf{r}; E) + \Sigma^<(\mathbf{r}, \mathbf{r}'; E) G^A(\mathbf{r}', \mathbf{r}; E) \\ &- G^R(\mathbf{r}, \mathbf{r}'; E) \Sigma^<(\mathbf{r}', \mathbf{r}; E) - G^<(\mathbf{r}, \mathbf{r}'; E) \Sigma^A(\mathbf{r}', \mathbf{r}; E)], \end{aligned} \tag{2-60}$$

where the trace is done over spin indices. It is also useful to define the *spectrally resolved current density*, which from equation (2-59) and ignoring the energy integration, can be written as

$$J(\mathbf{r}, E) = \lim_{\mathbf{r}' \to \mathbf{r}} \frac{i}{2} [\mathbf{v}(\mathbf{r}') - \mathbf{v}(\mathbf{r})] \sum_{\sigma} G^{<}_{\sigma,\sigma}(\mathbf{r}, \mathbf{r}'; E). \tag{2-61}$$

2.4. Boundary conditions and boundary self-energy

When coupling a device to a contact that acts as electron reservoir, boundary conditions are inserted in the device Green's function through the inclusion of boundary self-energies. In the next, we present a simple derivation for the boundary self-energies.

Consider first the Dyson's equation for the retarded Green's function of the whole device-contact system in its discretized form, as presented in equation (2-44). In the absence of particle interaction ($\mathbf{\Sigma}^{scat.} = 0$), this matrix equation can be written in the following way

$$\begin{bmatrix} E\mathbf{M}_D - \mathbf{H}_D & -\tau \\ -\tau^\dagger & E\mathbf{M}_R - \mathbf{H}_R \end{bmatrix} \begin{bmatrix} \mathbf{G}_D^R & \mathbf{G}_{DR}^R \\ \mathbf{G}_{RD}^R & \mathbf{G}_R^R \end{bmatrix} = \begin{bmatrix} \mathbb{1} & \mathbf{0} \\ \mathbf{0} & \mathbb{1} \end{bmatrix}, \tag{2-62}$$

where $\tau = \mathbf{H}_{DR}$ is the coupling between device and reservoir, and $\mathbf{H}_R$ and $\mathbf{H}_D$ are the hamiltonians of the isolated reservoir and device, respectively. The energy dependence of the matrices have been also omitted for simplicity.

Since our interest is just devoted to the device Green's function $\mathbf{G}_D^R$, we can use above matrix equation to derive an expression for it. In fact, making the block multiplication, we arrive to the following set of equations

$$(E\mathbf{M}_D - \mathbf{H}_D)\mathbf{G}_D^R - \tau\mathbf{G}_{DR}^R = \mathbb{1} \tag{2-63a}$$

$$(E\mathbf{M}_R - \mathbf{H}_R)\mathbf{G}_{DR}^R - \tau^\dagger\mathbf{G}_D^R = \mathbf{0}. \tag{2-63b}$$

Consider now the isolated contact Green's function $\mathbf{g}_R^R$, defined by the equation

$$(E\mathbf{M}_R - \mathbf{H}_R)\mathbf{g}_R^R = \mathbb{1}. \tag{2-64}$$

Finally, we can substitute $\mathbf{g}_R^R$ from (2-64) in (2-63b), and $\mathbf{G}_{DR}^R$ from (2-63b) in (2-63a), to obtain

$$(E\mathbf{M}_D - \mathbf{H}_D - \mathbf{\Sigma}^{RB})\mathbf{G}_D^R = \mathbb{1} \tag{2-65}$$

$$\mathbf{\Sigma}^{RB} = \tau\mathbf{g}_R^R\tau^\dagger. \tag{2-66}$$

The lesser and greater boundary self-energies can be obtained from $\mathbf{\Sigma}^{RB}$ using equations (2-49a) and (2-49b), where $\mathbf{\Sigma}^{AB} = \{\mathbf{\Sigma}^{RB}\}^{-1}$.

2.5. Particle interactions

In this section, the interactions between particles is studied within the NEGF formalism, by the introduction of scattering *self-energies*. Below, we present just the results, but further information about the complete derivation of the self-energy expressions can be found in Appendix A.

2.5.1. Electron-phonon self-energy

The electron-phonon Fock self-energy term, assuming an equilibrium phonon population N_q and that phonons are not affected by confinement (bulk phonon modes), is given by

$$\Sigma^{\gtrless}_{\nu,\mu}(\mathbf{k},E) = \sum_{\mathbf{Q}} |U_Q|^2 e^{iq_z(z_i-z_j)} \cdot \left\{ M \left[N_Q G^{\gtrless}(\mathbf{k}-\mathbf{q}, E \pm \hbar\omega_Q) + (N_Q+1) G^{\gtrless}(\mathbf{k}-\mathbf{q}, E \mp \hbar\omega_Q) \right] M \right\}_{\nu,\mu} \quad (2\text{-}67)$$

$$\Sigma^{R}(\mathbf{k},E) = \frac{1}{2}(\Sigma^{>}(\mathbf{k},E) - \Sigma^{<}(\mathbf{k},E)) - i\mathcal{P}\int \frac{dE'}{2\pi} \frac{\Sigma^{<}(\mathbf{k},E') - \Sigma^{>}(\mathbf{k},E')}{E-E'}. \quad (2\text{-}68)$$

where $\mathbf{Q} = (\mathbf{q}, q_z)$ is the 3D phonon wavevector, U_Q is the scattering strength in energetic units, $\mathcal{P}$ denotes the principal value and z_j is the position of the discretized mesh points. The principal part in equation (2-68) leads to a negligible energy renormalization and is usually neglected obtaining the following approximate expression for the retarded self-energy

$$\Sigma^{R}(\mathbf{k},E) \approx \frac{1}{2}(\Sigma^{>}(\mathbf{k},E) - \Sigma^{<}(\mathbf{k},E)). \quad (2\text{-}69)$$

Acoustic phonons

For acoustic phonons, a linear dispersion relation is assumed $\omega_Q = Qu_l$, and the scattering strength is given by [13]

$$U_Q = \sqrt{\frac{\hbar D_a^2}{2V\rho u_l} Q} \quad (2\text{-}70)$$

where u_l is the longitudinal sound velocity in the material, D_a is the deformation potential, $V = \mathcal{A} \times \mathcal{L}$ is the normalization volume and ρ is the (mass) density. At sufficiently high temperature, $\hbar\omega_Q$ is much smaller than k_BT, allowing to approximate the phonon occupation number $N_Q = \dfrac{1}{e^{\frac{\hbar\omega_Q}{k_BT}} - 1} \approx \frac{k_BT}{\hbar\omega_Q} \approx N_Q + 1$. Using this result and equation (2-67), the acoustic phonon self-energy yields

$$\Sigma^{\gtrless,R}_{\nu,\mu}(\mathbf{k},E) = \frac{1}{\Delta_{ij}} \frac{D_a^2 k_B T}{V\rho u_l^2} \sum_{\mathbf{q}} \left\{ M G^{\gtrless,R}(\mathbf{k}-\mathbf{q},E) M \right\}_{\nu,\mu} \quad (2\text{-}71)$$

with

$$\frac{1}{\Delta_{ij}} = \sum_{q_z} e^{iq_z(z_i - z_j)} = \frac{\mathcal{L}}{2\pi} \int_{-\pi/a_L}^{\pi/a_L} dq_z \, e^{iq_z(z_i - z_j)} = \frac{\mathcal{L}}{\pi} \frac{\sin \frac{\pi}{a_L}(z_i - z_j)}{z_i - z_j}, \tag{2-72}$$

and a_L the lattice constant in the transport direction.

Note that in (2-71) we have used that $0 < \hbar\omega_Q \ll 1$ for acoustic phonons, hence $G^{\gtrless,R}(\mathbf{k} - \mathbf{q}, E \pm \hbar\omega_Q) \approx G^{\gtrless,R}(\mathbf{k} - \mathbf{q}, E)$, which simply means that the scattering is essentially elastic.

Polar optical phonons

For optical phonons, a dispersion-less longitudinal phonon energy is assumed $\hbar\omega_{LO}$, with characteristic frequency ω_{LO}. The scattering strength term is given by [13]

$$U_Q = \sqrt{\frac{e^2\hbar\omega_{LO}}{2V}\left(\frac{1}{\epsilon_\infty} - \frac{1}{\epsilon_s}\right)} \frac{Q}{Q^2 + q_0^2}, \tag{2-73}$$

where ϵ_s and ϵ_∞ are the static and optical dielectric constants of the material, respectively, and $q_0 = \sqrt{\dfrac{e^2 n}{\epsilon_s k_B T}}$ is the inverse Debye-Hückel screening length. Assuming isotropy in the transverse direction (axial approximation), and after some simplifications, the final form of the lesser and greater self-energies for polar optical phonons can be written as follows

$$\begin{aligned}\Sigma^{\gtrless}_{\nu,\mu}(\mathbf{k}, E) = {} & \frac{e^2\hbar\omega_{LO}}{4\pi^2}\left(\frac{1}{\epsilon_\infty} - \frac{1}{\epsilon_s}\right) \int dq \, qF(q, s_{ij}, k) \\ & \cdot \left\{ M \left[N_{LO} G^{\gtrless}(\mathbf{q}, E \pm \hbar\omega_{LO}) + (N_{LO} + 1) G^{\gtrless}(\mathbf{q}, E \mp \hbar\omega_{LO}) \right] M \right\}_{\nu,\mu}\end{aligned} \tag{2-74}$$

where $N_{LO} = \left(e^{\frac{\hbar\omega_{LO}}{kT}} - 1\right)^{-1}$ is the phonon occupation number, $s_{ij} = z_i - z_j$ and

$$\begin{aligned}F(q, s_{ij}, k) = {} & \int_0^{\pi/a_L} dq_z \cos(q_z s_{ij}) \\ & \cdot \left[\frac{1}{\sqrt{(q_z^2 + q^2 + q_0^2 + k^2)^2 - 4k^2q^2}} - q_0^2 \frac{q_z^2 + q^2 + q_0^2 + k^2}{((q_z^2 + q^2 + q_0^2 + k^2)^2 - 4k^2q^2)^{3/2}} \right].\end{aligned} \tag{2-75}$$

with a_L the lattice parameter of the material.

The retarded self-energy can be then calculated using equation (2-69).

2.5.2. Electron-photon self-energy

The electron-phonon Fock self-energy term is obtained in a similar way as done for the phonon self-energy. A complete derivation for this self energy can be found in Appendix A. Assuming a photon population $N_{Q,\lambda}$, with (3D) wavevector $\mathbf{Q}$, energy $\hbar\omega_Q$ and polarization λ, the self-energy terms read in matrix notation

$$\Sigma^{\gtrless}(\mathbf{k},E) = \sum_{\mathbf{Q},\lambda} M^{\gamma}(\mathbf{k},\mathbf{Q},\lambda)\cdot[N_{Q,\lambda}\,G^{\gtrless}(\mathbf{k},E\pm\hbar\omega_Q) + (N_{Q,\lambda}+1)\,G^{\gtrless}(\mathbf{k},E\mp\hbar\omega_Q)]M^{\gamma}(\mathbf{k},\mathbf{Q},\lambda) \tag{2-76}$$

$$\Sigma^{R}(\mathbf{k},E) = \frac{1}{2}(\Sigma^{>}(\mathbf{k},E)-\Sigma^{<}(\mathbf{k},E)) - i\mathcal{P}\int\frac{dE'}{2\pi}\frac{\Sigma^{<}(\mathbf{k},E')-\Sigma^{>}(\mathbf{k},E')}{E-E'}. \tag{2-77}$$

where the matrix $M^{\gamma}(\mathbf{k},\mathbf{Q},\lambda)$, in the dipole approximation [10], is defined by

$$M^{\gamma}_{\nu,\mu}(\mathbf{k},\mathbf{Q},\lambda) = \frac{e}{m_0}\mathbf{A}_0(\mathbf{Q},\lambda)\cdot\mathbf{p}_{\nu,\mu}(\mathbf{k}) \tag{2-78}$$

with the field operator[3],

$$\mathbf{A}_0(\mathbf{Q},\lambda) = \sqrt{\frac{\hbar}{2\epsilon_0\omega_Q V}}\epsilon_{\mathbf{Q},\lambda}, \tag{2-79}$$

the mommentum matrix element given by

$$\mathbf{p}_{\nu,\mu}(\mathbf{k}) = \int d\mathbf{r}\phi^{*}_{\nu}(\mathbf{r},\sigma,\mathbf{k})\hat{\mathbf{p}}(\mathbf{r})\phi_{\mu}(\mathbf{r},\sigma,\mathbf{k}). \tag{2-80}$$

and $\epsilon_{\mathbf{Q},\lambda}$ being the polarization of the photon.

As in the case of phonons, that the principal part in (2-77) contributes only in an energy renormalization which is negligible compared with the total value of the retarded self-energy, and hence can be neglected leading to the same expression exposed in (2-69). Using the *Feynman-Hellman* theorem, the momentum matrix element can be computed directly from the Hamiltonian, in the following way,

$$\mathbf{p}_{\nu,\mu} = \frac{m_0}{\hbar}\nabla_{\mathbf{k}}H_{\nu,\mu} \tag{2-81}$$

It is important to note that the photon self-energy is not unique, but depends on the type of radiation source used to illuminate the device, through the corresponding field operator.

[3]Vector pontential opertor here is written for a monochromatic source of light of wavelength λ and polarization vector $\epsilon_{\mathbf{Q},\lambda}$.

2.6. Poisson Equation

The last ingredient in the NEGF simulation of electronic devices is the Poisson equation, which is solved self-consistently in what is usually called the *outer-loop*. The Poisson equation

$$\partial_z(\epsilon(z)\partial_z\phi(z)) = -\rho(z) \tag{2-82}$$

where $\epsilon(z)$ is the (position dependent) static dielectric constant and

$$\rho(z) = e[p(z) - n(z) + N_{dop}(z)], \tag{2-83}$$

relates the Hartree potential $\phi(z)$ to the carrier and doping densities. Equation (2-82) together with equations (2-55) and (2-56) for the carrier densities, and the Dyson's equation (2-44) form a closed set of equations that can be solved self-consistently. The iteration steps for both inner and outer-loop are described in figure **2-2**. The inner self-consistency loop connects the equations for the Green's functions and self-energies, while the outer loop provides the update of the Hartree potential from the solution of Poisson's equation. An initial condition is used at the first step of the process, being this $\mathbf{G}_0$ chosen to be the the Green's function at ballistic conditions (with just the boundary self-energy included). Although this seems to be a good choice, it does not always results to be the best, as convergence (of both inner and outer loop) strongly depend on the initial condition.

2.7. Choice of basis

2.7.1. Thight-binding model for layered semiconductors

Thight-binding model is an atomistic model, in which basis functions are represented as Bloch sums of localized atomic orbitals (LAO). In the case of symmetrically orthogonalized atomic orbitals, called Löwdin orbitals, this basis has the additional advantage of simplifying computational operations due to the fact that the overlap matrix correspond with the identity matrix.

In relation to layered semiconductors, crystalline properties in the transverse direction are exploited, leading to the formulation of the so called *planar orbitals*, which we will use as our basis functions. In this sense, a layer will be defined as a collection of atomic planes perpendicular to the growth direction (which will be considered to be the z direction) which themselves form a unit cell when seen as a linear chain in the same direction. The orbitals α in the i^{th} atomic plane of a given layer L form the so called *planar orbital*, as a sum of atomic orbitals $|\alpha i, L, \mathbf{R}_{||}\rangle$ located at $\mathbf{R} = (\mathbf{R}_{||} + \mathbf{v}^i_{||}, L\Delta + v^i_z)$, and wighted by the phase factor $e^{i\mathbf{k}\cdot(\mathbf{R}_{||}+\mathbf{v}^i_{||})}$, e.i.

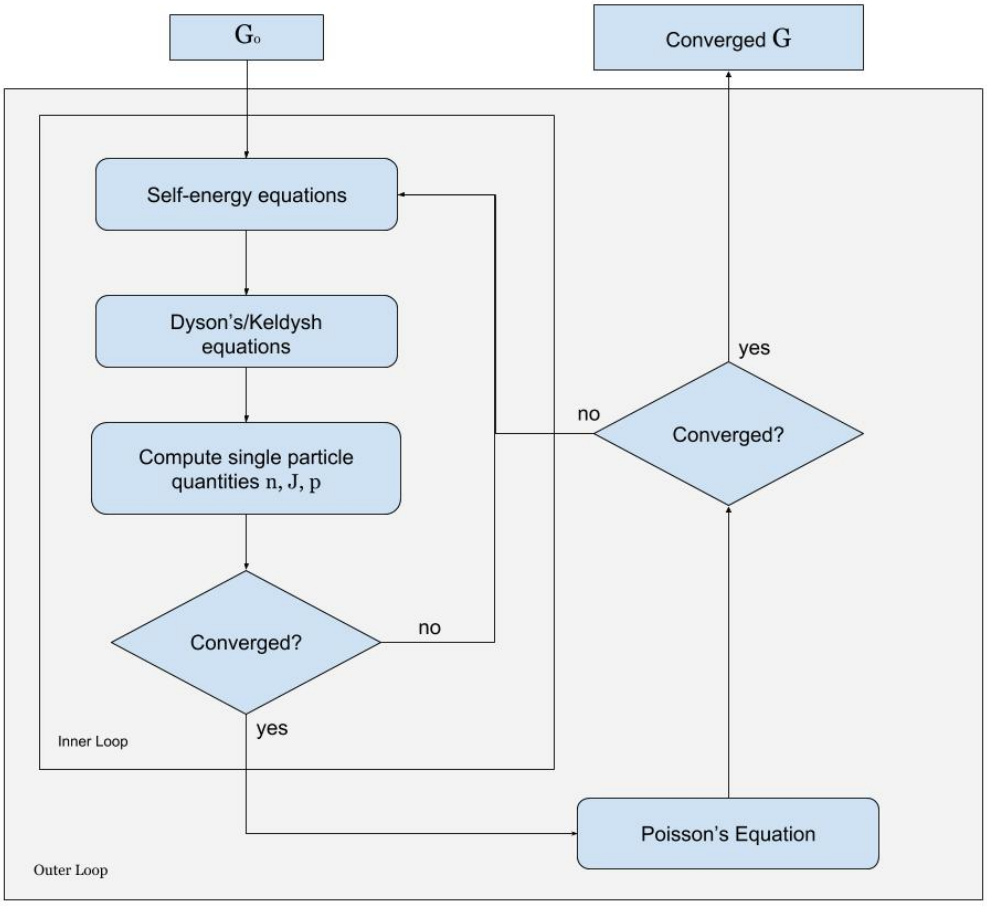

Figure 2-2: *Flowchart for the calculation of physical quantities from Green's functions.*

$$|\alpha i, L, \mathbf{k}\rangle = \frac{1}{\sqrt{N_{||}}} \sum_{\mathbf{R}_{||}} e^{i\mathbf{k}\cdot(\mathbf{R}_{||}+\mathbf{v}^i_{||})} |\alpha i, L, \mathbf{R}_{||}\rangle \tag{2-84}$$

where $\mathbf{k}$ and $R_{||}$ are the transversal component of the wavevector and position, respectively, the vector $\mathbf{v}^i = (\mathbf{v}^i_{||}, v^i_z)$ is the position of atom i in the unit cell, and $N_{||}$ is the number of points in the transverse Brillouin zone. Referring to the notation used in section 2.2, these basis functions are characterized by the set of quantum numbers $\nu = (\alpha, i, L, \mathbf{k})$.

In the planar-orbital basis, the Hamiltonian matrix elements of the isolated system are written using empirical parameters, which are selected to fit the effective masses and bandgap of a specific material. In our case, we will use the parameter presented by *Volg et al.* [14] for the spinless case, and those presented by *Wei et al.* [15] for the models including spin. The Hamiltonian can be written in the following general form:

$$\langle \alpha i, L, \mathbf{k}|H|\alpha i', L', \mathbf{k}\rangle = (D_{\alpha i,\alpha i';L}(\mathbf{k}) + U_L \mathbb{1}_{2b})\delta_{L,L'} - t_{\alpha i,L;\alpha i';L'}(\mathbf{k})(1-\delta_{L,L'}) \tag{2-85}$$

where U_L is the electrostatic potential at layer L, and b is the number of orbitals per atom. In the following, to simplify notation, both atom and orbital type information will be condensed into a single index α, e.i., $\alpha i \equiv \alpha$.

In the simplest model, the s model, the functions $D_L(\mathbf{k})$ and $t_{L,L'}(\mathbf{k})$ are scalar functions of the wavevector $\mathbf{k}$. In general, for a material composed of two basis atoms (cation and anion), diagonal and off-diagonal block elements of the non-interacting Hamiltonian, in the nearest neighbor approximation, can be written as,

$$D_L = \begin{pmatrix} E_c & U_{ca} \\ U_{ac} & E_a \end{pmatrix}, \quad t_{L,L+1} = \begin{pmatrix} 0 & 0 \\ V_{ac} & 0 \end{pmatrix}, \quad t_{L,L-1} = \begin{pmatrix} 0 & V_{ca} \\ 0 & 0 \end{pmatrix} \tag{2-86}$$

where E_c, E_a, U_{ac}, V_{ac} are block matrices of dimension b, and $U_{ac} = U_{ca}^\dagger$ and $V_{ac} = V_{ca}^\dagger$, due to hermiticity of the Hamiltonian.

Single band model

In the single band model, a single s-orbital per lattice site is used, and the contribution of the various atoms in the lattice is lumped in this single orbital. The expression for the diagonal and off-diagonal element can be shown to be [16]

$$t_{L,L'} = -\frac{\hbar^2}{(m_L^* + m_{L'}^*)\Delta^2}, \tag{2-87}$$

$$D(\mathbf{k}) = \frac{\hbar^2}{2\Delta^2}\left(\frac{1}{m^-} + \frac{1}{m^+}\right) + \frac{\hbar^2 k^2}{2m_L^*}, \tag{2-88}$$

$$m^- = \frac{m_{L-1}^* + m_L^*}{2} \quad \text{and} \quad m^+ = \frac{m_L^* + m_{L+1}^*}{2}, \tag{2-89}$$

where m_L^* is the effective mass at layer L and $\Delta = a_L/2$ is the layer width, a_L being the lattice constant.

Diatomic two-band model

The simplest model to represent the conduction and valence band structure of a direct band gap semiconductor is the diatomic model or sp_z model. In this model, we place an s-type orbital in the cation and a p_z-type orbital in the anion, in order to reproduce a two-band dispersion. In this case, diagonal and off-diagonal elements can be written in terms of the on-site energies E_s, for the cation, and E_p, for the anion, and the inter-orbital coupling V_{sp}

$$D_L = \begin{pmatrix} E_s + \frac{\hbar^2 k^2}{2m^*_{e,L}} & -V_{sp} \\ -V_{sp} & E_p - \frac{\hbar^2 k^2}{2m^*_{h,L}} \end{pmatrix}, \; t_{L,L+1} = \begin{pmatrix} 0 & 0 \\ -V_{sp} & 0 \end{pmatrix}, \; t_{L,L-1} = \begin{pmatrix} 0 & -V_{sp} \\ 0 & 0 \end{pmatrix} \quad (2\text{-}90)$$

where $m^*_{e,L}$ and $m^*_{h,L}$ are the electron and hole effective masses in layer L, respectively. Using equation (2-81), the momentum matrix element can be shown to be [10]

$$p^z_{\alpha,L;\alpha',L'}(\mathbf{k}) = \frac{m_0}{i\hbar}[(L'-L)\Delta + v_z^{\alpha'} - v_z^{\alpha}]H_{\alpha,L;\alpha',L'}(\mathbf{k}) \quad (2\text{-}91)$$

for longitudinal polarization, and

$$\mathbf{p}^{||}_{\alpha,L;\alpha',L'}(\mathbf{k}) = \delta_{L,L'}(-1)^{\delta_{\alpha,a}}\frac{im_0}{2\hbar}a_L V_{sp}\cos(\mathbf{k}\frac{a_L}{4}) \quad (2\text{-}92)$$

for transversal polarization, where the quantity v_z^{α}, for a two-atom basis material, will be defined in the following way

$$v_z^{\alpha} = \begin{cases} 0 & \alpha = c \\ \dfrac{\Delta}{2} & \alpha = a \end{cases} \quad (2\text{-}93)$$

where a/c stand for anion/cation.

sp_3s^* model

This model allows to reproduce with reasonable accuracy the band structure of semiconductors, by using $sp3$ orbitals with an extra excited s^* orbital to improve the fit in the conduction band. This five orbitals are placed in both anion and cation, allowing to reproduce a ten-band dispersion. More advantageous is the fact that spin-orbit coupling can be included in the model to accurately represent band structure effects due to spin, like the separation of the split-off band from heavy and light hole bands at the Γ point. In the simple spinless case, elements in equation (2-86) can be written in the following way [10]

$$E_\alpha = \begin{pmatrix} E_{s\alpha} & & & & \\ & E_{p\alpha} & & & \\ & & E_{p\alpha} & & \\ & & & E_{p\alpha} & \\ & & & & E_{s^*\alpha} \end{pmatrix}, \quad \alpha = a, c, \tag{2-94a}$$

$$U_{ac} = \begin{pmatrix} V_{ss}c_- & iV_{sapc}s_- & -iV_{sapc}s_- & -V_{sapc}c_- & 0 \\ -iV_{pasc}s_- & V_{xx}c_- & -V_{xy}c_- & -iV_{xy}s_- & -iV_{pas^*c}s_- \\ iV_{pasc}s_- & -V_{xy}c_- & V_{xx}c_- & iV_{xy}s_- & iV_{pas^*c}s_- \\ V_{pasc}c_- & -iV_{xy}s_- & iV_{xy}s_- & V_{xx}c_- & V_{pas^*c}c_- \\ 0 & iV_{s^*apc}s_- & -iV_{s^*apc}s_- & -V_{s^*apc}c_- & 0 \end{pmatrix}, \tag{2-94b}$$

$$V_{ac} = \begin{pmatrix} V_{ss}c_+ & iV_{sapc}s_+ & iV_{sapc}s_+ & V_{sapc}c_+ & 0 \\ -iV_{pasc}s_+ & V_{xx}c_+ & V_{xy}c_+ & iV_{xy}s_+ & -iV_{pas^*c}s_+ \\ -iV_{pasc}s_+ & V_{xy}c_+ & V_{xx}c_+ & iV_{xy}s_+ & -iV_{pas^*c}s_+ \\ -V_{pasc}c_+ & iV_{xy}s_+ & iV_{xy}s_+ & V_{xx}c_+ & -V_{pas^*c}c_+ \\ 0 & iV_{s^*apc}s_+ & iV_{s^*apc}s_+ & V_{s^*apc}c_+ & 0 \end{pmatrix}, \tag{2-94c}$$

with $c_\pm = \frac{1}{2}\cos(\mathbf{k}\cdot\mathbf{d}_\pm)$, $s_\pm = \frac{1}{2}\sin(\mathbf{k}\cdot\mathbf{d}_\pm)$, and $\mathbf{d}_\pm = (1, \pm 1)\frac{a_L}{4}$.

When including spin-coupling in the model, some modifications are done to the blocks E_c, and E_a, and new blocks are added to the non-interacting Hamiltonian blocks D_L and $t_{L,L'}$ [15]

$$E_\alpha = \begin{pmatrix} E_{s\alpha} & & & & \\ & E_{p\alpha} & -i\frac{\Delta_\alpha}{3} & & \\ & i\frac{\Delta_\alpha}{3} & E_{p\alpha} & & \\ & & & E_{p\alpha} & \\ & & & & E_{s^*\alpha} \end{pmatrix}, \quad \alpha = a, c, \tag{2-95}$$

$$D_L = \begin{pmatrix} H_c & H_{ca} \\ H_{ca}^\dagger & H_a \end{pmatrix}, \quad t_{L,L+1} = \begin{pmatrix} 0 & 0 \\ H_{ac} & 0 \end{pmatrix}, \quad t_{L,L-1} = \begin{pmatrix} 0 & H_{ac}^\dagger \\ 0 & 0 \end{pmatrix}, \tag{2-96}$$

with the new block matrices defined as

$$H_\alpha = \begin{pmatrix} E_\alpha & E_{\alpha,so} \\ E_{\alpha,so}^\dagger & E_\alpha^* \end{pmatrix}, \quad \alpha = a, c, \tag{2-97a}$$

$$H_{ca} = \begin{pmatrix} U_{ca} & 0 \\ 0 & U_{ca} \end{pmatrix}, \quad H_{ac} = \begin{pmatrix} V_{ac} & 0 \\ 0 & V_{ac} \end{pmatrix} \tag{2-97b}$$

$$E_{\alpha,so} = \begin{pmatrix} 0 & 0 & 0 & 0 & 0 \\ 0 & 0 & 0 & \frac{\Delta_\alpha}{3} & 0 \\ 0 & 0 & 0 & -i\frac{\Delta_\alpha}{3} & 0 \\ 0 & -\frac{\Delta_\alpha}{3} & i\frac{\Delta_\alpha}{3} & 0 & 0 \\ 0 & 0 & 0 & 0 & 0 \end{pmatrix}, \quad \alpha = a, c, \tag{2-98}$$

and the matrices U_{ca} and V_{ac} are defined as before in equation (2-94).

For the tight binding parameters, we will use those presented by *Volg et al.* [14] for the spinless case, and those proposed by *Wai et al.* [15] for the spin-coupling case, and all these parameters can be found in tables **2-1** and **2-2**, respectively.

The momentum matrix element can be found by means of equation (2-81), by taking the derivative of block elements (2-94) with respect to $\mathbf{k}_{||}$ for the transversal polarization case, which results in making the following substitution to the above block elements

$$c_\pm \to -s_\pm \mathbf{d}_\pm \qquad s_\pm \to c_\pm \mathbf{d}_\pm. \tag{2-99}$$

For the case of longitudinal polarization, the result is the same as that obtained for the sp_z model, which is shown in equation (2-91). In the band basis, the momentum operator represents transitions between different bands, and its elements can be computed with equations (2-100) [17], with $C^n_{\alpha,L}$ the expansion coefficients of the state of a electron in band n. Figure **2-3** shows the (band) momentum matrix element $|\mathbf{p}_{nm}|^2$, computed for bulk GaAs and x-polarization.

$$\mathbf{p}_{n,m} = \sum_{\alpha,L,\alpha',L'} C^n_{\alpha,L}(\mathbf{k})^* \mathbf{p}_{\alpha,L;\alpha',L'} C^m_{\alpha',L'}(\mathbf{k}) \tag{2-100}$$

Boundary self-energy in the Tight-binding basis

In the tight binding basis, the general form of the boundary self-energy for the left contact, accounting for the openness of the system, can be written in terms of the eigenmodes of the infinite isolated lead. Here we state just the result, whose derivation can be seen in [10].

$$\Sigma^{RB}_{1,1} = -t_{1,0}(U_- \Lambda_z^{-1} U_-^{-1})^{-1} \tag{2-101a}$$
$$\Sigma^{RB}_{N,N} = -t_{N,N+1} U_+ \Lambda_z U_+^{-1} \tag{2-101b}$$

where $t_{1,0}$ and $t_{N,N+1}$ are the hopping elements between device and contact,

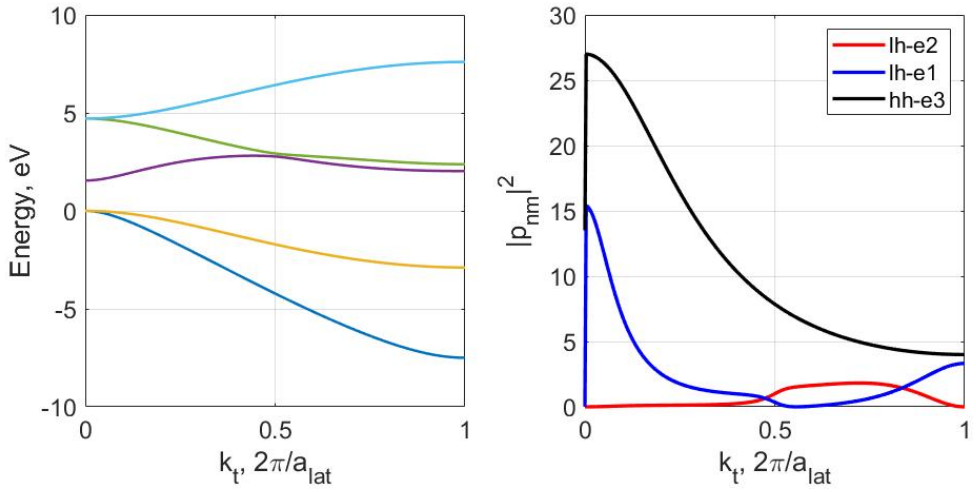

Figure 2-3: *Left: Bulk band structure. Right: Momentum transition matrix elements computed for different band pairs.*

$$U_{\pm} = \left(\begin{array}{c|c} \phi^1_{\pm,c} \cdots \phi^b_{\pm,c} & \mathbf{0} \\ \hline \mathbf{0} & \phi^1_{\pm,a} \cdots \phi^b_{\pm,a} \end{array}\right) \tag{2-102}$$

is a matrix whose columns correspond to the left $(-)$ or right $(+)$ propagating (decaying) Bloch states of the lead, and

$$\Lambda_z = \left(\begin{array}{ccc|ccc} e^{ik_z^1\Delta} & & 0 & & & \\ & \ddots & & & \mathbf{0} & \\ 0 & & e^{ik_z^b\Delta} & & & \\ \hline & & & e^{ik_z^1\Delta} & & 0 \\ & \mathbf{0} & & & \ddots & \\ & & & 0 & & e^{ik_z^b\Delta} \end{array}\right) \tag{2-103}$$

is a diagonal matrix whose elements correspond to propagating factors.

In order to compute self-energy for a given energy E, the eigenmodes of the infinite lead need to be computed and sorted, together with their corresponding wavevector $k_z = k_z(E)$, hence the complex band structure problem needs to be solved for the lead. To this end, we follow the approach shown in [18], by solving the Schrödinger equation for the isolated left lead system

$$H\phi^{\alpha} = E\phi^{\alpha} \tag{2-104}$$

Table 2-1: Spinless ETB material parameters for GaAs, InAs, GaSb and InSb at 300 K, taken from [14].

Parameters	GaAs	InAs	GaSb	InSb
E_{sa}	-8.3431	-9.5381	-7.3207	-8.0157
E_{pa}	1.0414	0.9099	0.8554	0.6738
E_{sc}	-2.6569	-2.7219	-3.8993	-3.4643
E_{pc}	3.6686	3.7201	2.9146	2.9162
E_{s^*a}	8.5914	7.4099	6.6354	6.4530
E_{s^*c}	6.7386	6.7401	5.9846	5.9362
V_{ss}	-6.4513	-5.6052	-6.1567	-5.5193
V_{xx}	1.9546	1.8398	1.5789	1.4018
V_{xy}	5.0779	4.4693	4.1285	3.8761
V_{sapc}	4.4800	3.0354	4.9601	3.7880
V_{pasc}	5.7839	5.4389	4.6675	4.5900
V_{s^*apc}	4.8422	3.3744	4.9895	3.5666
V_{pas^*c}	4.8077	3.9097	4.2180	3.4048

where α designates one of the N_α eigenmodes with energy E, and H is the tight binding Hamiltonian of the lead.

In the following, we will focus on the left lead, whose nodes are labeled starting from 0 to $-\infty$, and we will assume that couplings from device to lead are set to zero (which for TB imply that the block element of the total device-lead Hamiltonian $[H]_{1,0} = \mathbf{0}$). For a block-tridiagonal tight binding Hamiltonian of the form shown in (2-86), equation (2-104) takes the form

$$(D - E)\phi^\alpha_{-1} + t_l\phi^\alpha_0 + t_u\phi^\alpha_{-2} = 0, \tag{2-105}$$

with t_l the lower diagonal hopping element, t_u the upper diagonal hopping element, D the diagonal element, ϕ^α_0 the surface mode, and

$$\phi^\alpha_L = \begin{pmatrix} \phi^\alpha_{L,c} \\ \phi^\alpha_{L,a} \end{pmatrix} \qquad c \equiv \text{cation},\ a \equiv \text{anion}. \tag{2-106}$$

Replacing D, t_l and t_u from equation (2-86) in (2-105), and taking into account the translational invariance of the system that connects the wavefunctions at different positions via the relation[4]

[4]Here, (2-107) is stated as an assumption, but it appears naturally from the definition (2-84), when writing the matrix elements of the Hamiltonian equation (2-104) in the POB. See [19].

Table 2-2: ETB material parameters for GaAs, InAs, GaSb and InSb at 77 K, taken from [15].

Parameters	GaAs	InAs	GaSb	InSb
E_{sa}	-9.2664	-9.3562	-6.0493	-9.3378
E_{pa}	1.4866	1.8201	0.91157	0.39352
E_{sc}	-4.3504	-3.9611	-4.0712	-3.3248
E_{pc}	3.2136	3.1842	2.6352	2.0791
E_{s^*a}	8.7826	7.0432	7.8753	6.6378
E_{s^*c}	5.8765	6.1232	4.8565	5.3807
V_{ss}	-7.9480	-6.5393	-5.7762	-5.8320
V_{xx}	2.3069	2.5491	1.8244	1.2596
V_{xy}	5.0305	5.4700	5.3733	4.0026
V_{sapc}	2.7777	4.3607	4.4761	4.1129
V_{pasc}	10.005	7.0849	8.2748	7.5769
V_{s^*apc}	3.6271	3.0007	5.0079	3.4448
V_{pas^*c}	7.0071	5.4020	6.3813	5.8873
Δ_a	0.4210	0.4200	0.9730	0.9730
Δ_c	0.1740	0.3930	0.1740	0.3930

$$\phi_L^\alpha = e^{ik_z^\alpha(E)\Delta}\phi_{L-1}^\alpha, \tag{2-107}$$

equation (2-105) leads to a set of two matrix equations

$$V_{ca}\phi_{0,a}^\alpha + (E_c - E)e^{-ik_z^\alpha\Delta}\phi_{0,c}^\alpha + U_{ca}e^{-ik_z^\alpha\Delta}\phi_{0,a}^\alpha = 0; \tag{2-108a}$$

$$U_{ac}e^{-ik_z^\alpha\Delta}\phi_{0,c}^\alpha + (E_a - E)e^{-ik_z^\alpha\Delta}\phi_{0,a}^\alpha + V_{ac}e^{-2ik_z^\alpha\Delta}\phi_{0,c}^\alpha = 0 \tag{2-108b}$$

Multiplying the upper equation by $e^{ik_z^\alpha\Delta}$, and the lower one by $e^{2ik_z^\alpha\Delta}$, leads to the final generalized eigenvalue problem of the form

$$\begin{pmatrix} E_c - E & U_{ca} \\ V_{ac} & 0 \end{pmatrix}\begin{pmatrix} \phi_{0,c}^\alpha \\ \phi_{0,a}^\alpha \end{pmatrix} = e^{ik_z^\alpha\Delta}\begin{pmatrix} 0 & -V_{ca} \\ -U_{ac} & -(E_a - E) \end{pmatrix}\begin{pmatrix} \phi_{0,c}^\alpha \\ \phi_{0,a}^\alpha \end{pmatrix}, \tag{2-109}$$

whose solution, for a given energy E, allows to compute the propagators $e^{ik_z^\alpha\Delta}$ and the surface modes ϕ_0^α needed for the computation of the boundary self-energy in equation (2-101).

In order to obtain the matrices from equations (2-102) and (2-103), the eigenvalues and eigenmodes obtained from (2-109) need to be classified into right (+) or left (−) propagating or decaying modes. For the case of a N-band with two-atom basis, there are $N/2$

eigenmodes traveling or decaying to each side, and these can be classified in the following way: propagating states (real k_z) are classified according to the sign of the group velocity v_g in the longitudinal direction, such that positive or negative velocities travel to the right or to the left, respectively. On the other hand, decaying states (complex k_z) are simply classified according to the sign of the imaginary part of the longitudinal wavevector, as decaying to the left ($\Im(k_z) < 0$) or decaying to the right ($\Im(k_z) > 0$).

The computation of the group velocity can be carried out easily by means of the Hellman-Feynman theorem in the following way,

$$v_g^\alpha = \frac{1}{\hbar}\frac{dE}{dk_z}, \qquad \frac{dE}{dk_z} = \left\langle \phi^{\alpha\,*} \left| \frac{d\bar{H}}{dk_z} \right| \phi^\alpha \right\rangle \tag{2-110}$$

Multiplying equation (2-105) at the left by $\phi_{-1}^{\alpha\,*}$, it is easy to see that

$$\bar{H} = e^{-ik_z^\alpha \Delta} t_l + D + e^{ik_z^\alpha \Delta} t_u, \tag{2-111}$$

hence obtaining

$$\frac{d\bar{H}}{dk_z} = i\Delta \left[e^{-ik_z^\alpha \Delta} t_l + e^{ik_z^\alpha \Delta} t_u \right], \tag{2-112}$$

which can be substituted in (2-110) to obtain v_g^α, for each real k_z^α.

Current in the Tight-binding basis

Expressing equation (2-61) in the basis (2-84) one is able to find a formulation for the current density passing from layer $L-1$ to layer L. Here, we present just the result, but a complete demonstration can be found in [10]

$$J_L^{n(p)} = (-)\frac{e}{\hbar\mathcal{A}} \sum_{\mathbf{k}} \int \frac{dE}{2\pi} Tr \left[t_{L,L+1}(\mathbf{k}) G_{L+1,L}^{<(>)}(\mathbf{k}, E) - G_{L,L+1}^{<(>)}(\mathbf{k}, E) t_{L+1,L}(\mathbf{k}) \right] \tag{2-113}$$

where the trace is over orbital indices, and a factor of two still needs to be added in the spinless case.
The particle conservation law stated in (2-60), may now be written as

$$0 = J_L^n - J_{L-1}^n = \frac{e}{\hbar\mathcal{A}} \sum_{\mathbf{k}} \int \frac{dE}{2\pi} \mathrm{Tr} \left[\{ \Sigma^R G^< + \Sigma^< G^A - G^R \Sigma^< - G^< \Sigma^A \}_{L,L} \right]. \tag{2-114}$$

Omitting the energy integration in (2-113) we obtain an expression for the energy resolved current density

$$J_L^{n(p)}(E) = (-)\frac{e}{\hbar\mathcal{A}}\sum_{\mathbf{k}} Tr\left[t_{L,L+1}(\mathbf{k})G^{<(>)}_{L+1,L}(\mathbf{k},E) - G^{<(>)}_{L,L+1}(\mathbf{k},E)t_{L+1,L}(\mathbf{k})\right] \tag{2-115}$$

Additionally, as stated in [18], we present a second definition for the divergence of the electron current density[5]

$$\frac{dJ_L}{dz}(E) = \frac{e}{\hbar\mathcal{A}\Delta}\sum_{\mathbf{k}} Tr\left[\{\Sigma^{<}(\mathbf{k},E)G^{>}(\mathbf{k},E) - G^{<}(\mathbf{k},E)\Sigma^{>}(\mathbf{k},E)\}_{L,L}\right], \tag{2-116}$$

which is a very useful formula to compute the individual contributions of the scattering and coherent currents, by replacing the self energies $\Sigma^{\gtrless}$ by the corresponding scattering self-energy $\Sigma^{s,\gtrless}$ or the boundary self-energy $\Sigma^{b,\gtrless}$, respectively.

2.7.2. $\mathbf{k}\cdot\mathbf{p}$ model and hamiltonian representation

The $\mathbf{k}\cdot\mathbf{p}$ model is a multi-band model, in which electrons moving in a crystalline structure are described by a wavefunction which is expanded around a particular point of interest $\mathbf{k}_0$, which is typically located in the band edge of direct bandgap semiconductors. This method was firstly introduced by Bardeen and Seitz [20], and it has become very popular due to its relative simplicity and the fact that its able to accurately describe the band diagram of direct bandgap semiconductors close to the band edges, where the wavevector $\mathbf{k}$ deviates by a small amount from the considered point $\mathbf{k}_0$.

In our case, a real-space $\mathbf{k}\cdot\mathbf{p}$ basis is chosen, in which the FEM basis $\{t_i(z)\}$ of peak-shaped functions centered at z_i, is applied to discretize the computational (1D) domain along the perpendicular growth direction z in which the symmetry has been broken. The $\mathbf{k}\cdot\mathbf{p}$ basis function are then written in the following manner [18],

$$\phi_{\nu\mathbf{k}}(\mathbf{r}) = \frac{1}{\sqrt{A}}t_i(z)e^{i\mathbf{k}\cdot r_{||}}u_{m0}(\mathbf{r}), \tag{2-117}$$

where $\nu = (i,m)$ are the space (i) and band (m) indices combined, $\mathbf{k}$ is the transversal component of the wavevector, $u_{m0}(\mathbf{r})$ is the zone center Block function of band m, A denotes the cross sectional area and $r_{||}$ is the 2D position vector over the planes transversal to the z-axis.

[5] When the factor e in (2-116) is not included, the formula represents a scattering rate (units $m^{-3}s^{-1}eV^{-1}$). In fact, particular scattering self-energies can be used to compute the *spectrally resolved scattering rate* (*optical generation rate* for the case of photons).

The noninteracting Hamiltonian matrix elements in the $\mathbf{k}\cdot\mathbf{p}$ basis are found from equation (2-46b), which under some assumptions (e.g. axial approximation) can be demonstrated to depend on empirical parameters. We will not present here the complete derivation of the Hamiltonian, since it is already well documented in the literature [21], but simply present the parameters that will be used for the subsequent simulations, which for the case of a 8×8 $\mathbf{k}\cdot\mathbf{p}$ Hamiltonian are given in table **2-3**.

Table 2-3: $\mathbf{k}\cdot\mathbf{p}$ material parameters for AlSb, InAs, GaSb and InSb, taken from [22].

Parameters	AlSb	InAs	GaSb	InSb
E_g	2.386	0.42	0.81	0.235
m_c/m_0	0.13	0.0224	0.0412	0.0135
γ_1	4.15	19.4	11.84	32.4
γ_2	1.28	8.545	4.25	13.3
γ_3	1.75	9.17	5.01	15.15
Δ	0.65	0.38	0.81	0.81
E_p	18.7	21.5	22.4	23.3

On the other hand, the overlap matrix expressed in basis (2-117) is different from the identity, as in the previous case, due to the fact that the finite element basis functions $t_i(z)$ have non-negligible overlap. Introducing the coarse-graining assumption [18]

$$\int d\mathbf{r}\, t_i(z)t_j(z)\, u^*_{m0}(\mathbf{r})u_{n0}(\mathbf{r}) \approx \int dz\, t_i(z)t_j(z)\, A\,\frac{1}{\Omega}\int_\Omega d\mathbf{r}'\, u^*_{m0}(\mathbf{r}')u_{n0}(\mathbf{r}') \tag{2-118}$$

The overlap matrix is written as follows,

$$\begin{aligned} M_{\nu\mu} &= \int d\mathbf{r}\,\phi^*_{\nu\mathbf{k}}(\mathbf{r})\phi_{\mu\mathbf{k}}(\mathbf{r}) = \frac{1}{A}\int d\mathbf{r}\, t_i(z)t_j(z)\, u^*_{m0}(\mathbf{r})u_{n0}(\mathbf{r}) \\ &\approx \int dz\, t_i(z)t_j(z)\,\delta_{mn} \end{aligned} \tag{2-119}$$

where $\nu=(i,m)$, $\mu=(j,n)$, Ω is the volume of one unit cell, and the orthogonality condition of the Bloch functions was used $\frac{1}{\Omega}\int_\Omega u_{m0}u_{n0}=\delta_{mn}$.

Boundary self-energy in the $\mathbf{k}\cdot\mathbf{p}$ basis

In the case of $\mathbf{k}\cdot\mathbf{p}$ basis, finding the boundary self-energy requires again to solve the complex band structure problem of the isolated leads. It can be demonstrated [23, 19] that the lead Hamiltonian can be written as a second order polynomial of the transversal wavevector k_z

$$\bar{H} = H^{(0)} + H^{(1)}k_z + H^{(2)}k_z^2 \tag{2-120}$$

which, together with the Schrödinger equation (2-104), transforms the complex band structure problem into a generalized eigenvalue problem for k_z and the surface mode ϕ^α

$$\begin{pmatrix} 0 & \mathbb{1} \\ H^{(0)} - E\mathbb{1} & H^{(1)} \end{pmatrix} \begin{pmatrix} \phi^\alpha \\ k_z^\alpha \phi^\alpha \end{pmatrix} = k_z^\alpha \begin{pmatrix} \mathbb{1} & 0 \\ 0 & -H^{(2)} \end{pmatrix} \begin{pmatrix} \phi^\alpha \\ k_z^\alpha \phi^\alpha \end{pmatrix}. \tag{2-121}$$

The boundary self-energies can be found using the following equations [23, 19] ,

$$\Sigma_{1,1}^{RB} = -H^{(2)}\,[\phi^-] K_z^- [\phi^-]^{-1} + \frac{i}{2} H^{(1)} \tag{2-122a}$$

$$\Sigma_{N,N}^{RB} = -H^{(2)}\,[\phi^+] K_z^+ [\phi^+]^{-1} + \frac{i}{2} H^{(1)} \tag{2-122b}$$

where $[\phi^\pm]$ is a matrix which has the left (ϕ^-) or right (ϕ^+) propagating (decaying) eigenvectors organized in its columns, and the matrix $K_z^\pm$ is defined in as follows

$$K_z^\pm = \begin{pmatrix} k_z^{1\pm} & & 0 \\ & \ddots & \\ 0 & & k_z^{N_\alpha \pm} \end{pmatrix}, \tag{2-123}$$

N_α is the total number of modes k_z^α with energy E, and $\pm$ designates right or left propagating (decaying) eigenvalues of (2-121).

For an N-band model, we will obtain $2N$ solutions for (2-121) which can be classified depending on the nature of the modes (propagating or decaying) in the same way as was done for the tight binding case (see section 2.7.1). In this case, the derivative of the Hamiltonian with respect to the longitudinal wavevector is obtained from (2-120) as

$$\frac{d\bar{H}}{dk_z} = H^{(1)} + 2H^{(2)} k_z^\alpha. \tag{2-124}$$

Chapter 3

Numerical Results

3.1. Numerical considerations and choice of simulation parameters

Despite being a very powerful method for the simulation of nanoscale optoelectronic devices, the NEGF very computationally demanding. If we for example consider a small resistor structure of 100 nm length, composed of a given material with an average lattice constant of $a_{lat} = 0.6$ nm, in the TB basis this would be discretized in about $N_z \approx 330$ layers. Additionally, if a discretization in energy and k-space is chosen such that $N_E = 300$ and $N_k = 50$ points are considered, respectively, within the two-band TB model $N_B = 2$, then each single Green's function or self-energy will be composed of $(N_B \times N_z)^2 \times N_E \times N_k = 6.534 \times 10^9$ complex numbers. This simple example is useful to see how intensive the NEGF method is, both in therms of time, because of all the matrix multiplications and inversions it involves and which should be iterated to convergence, and in terms of memory, this considering that at least $G^<$, G^R, $\Sigma^<$ and Σ^R should be stored at each iteration, all of them having the above calculated size. Hence, all the examples showed in this work will be limited to small devices of no more than 80 nm length, in which the bandgaps and applied bias will be small enough to ensure an energy grid of not too many points. Further improvements to the NEGF method, in terms of convergence and memory requirements, will be also discussed at the end of this section.

One key aspect before running the NEGF simulations is choosing appropriately all the simulation parameters, such as ΔE, Δk, k_{max}, and the energy grid boundaries E_{min} and E_{max}. Energy and transverse momentum resolutions, ΔE and Δk respectively, should be chosen small enough to be able to recognize all the spectral features of the simulated device, since spectral quantities are going to be integrated in energy and momentum, but at the same time not so small so they allow a reasonable computation time. In the case of transverse momentum, effects of choosing high values of Δk are evidenced as oscillating peaks in the spectral

quantities. Here we take the value suggested in [10] for this quantity $\Delta k \approx 0.003\pi/\Delta$, with Δ the mesh/monolayer spacing. In the case of the energy resolution, a value of ΔE less than 10 meV seems to give a good compromise between resolution and computation time.

On the other hand, the spectral range (both in energy and transversal momentum) should be chosen so to consider all the important phenomena that is desired to capture within the simulation. Good values for E_{min} and E_{max} are about 0.5 eV below and above the band edge extremas. Finally, values of k_{max} have been suggested in the literature [18, 10], from which $k_{max} \approx 0.14\pi/\Delta$ seems to be a more than reasonable value, hence obtaining an average of $k_{max}/\Delta k \approx 50$ points for the transverse momentum discretization.

Among other parameters that need to be adjusted, the polar optical phonon energy $\hbar\omega_{LO}$ will be assumed to be 40 meV regardless on the material. This assumption apart of simplifying the implementation of the code, will help to avoid Green's function interpolation when computing the polar optical phonon self-energy, by taking ΔE an integer multiple of this quantity, so energy translations of $\hbar\omega_{LO}$ on any point of the grid will be another point in the grid.

As a last remark, it is important to clarify how the convergence of the inner and outer loop will be treated. For the outer loop, Poisson equation will be solved until the potential change $\delta U_k = |\mathbf{U}_k - \mathbf{U}_{k-1}|$ falls below a residual value ϵ_{outer}. Regarding the inner iterations, these will be performed until the relative change in the device current goes below a limiting value ϵ_{inner}, e.i.

$$\frac{|\mathbf{J}_k - \mathbf{J}_{k-1}|}{|\mathbf{J}_k|} < \epsilon_{inner} \tag{3-1}$$

Table **3-1** summarizes all the simulation parameters that will be used in the following simulations.

Table 3-1: Parameters used in the subsequent simulations.

Parameters	Value	Unit
ΔE	5	meV
Δk	0.03	1/nm
k_{max}	1.5	1/nm
N_k	50	
$\hbar\omega_{LO}$	40	meV
D_{aco}	8	eV
ϵ_{inner}	10^{-6}	
ϵ_{outer}	10^{-3}	

3.2. Single quantum well *p*-*i*-*n* LED

The first device considered for this work will be a single quantum well (SQW) *p*-*i*-*n* diode, composed of an intrinsic region with a high bandgap material (barrier made of $Al_{0.3}Ga_{0.7}As$) and a low bandgap material (well made of GaAs), which is sandwiched between two highly doped $Al_{0.3}Ga_{0.7}As$ layers both with a dopant concentration of $N_{d,a} = 10^{19}\,\mathrm{cm}^{-3}$. The total length of the device is approximately 38.5 nm and a transversal area $A = 10\ \mathrm{mm}^2$ is assumed. Device structure with its respective measures is shown in figure **3-1**, and the material parameters used for the simulation are shown in table **3-2**.

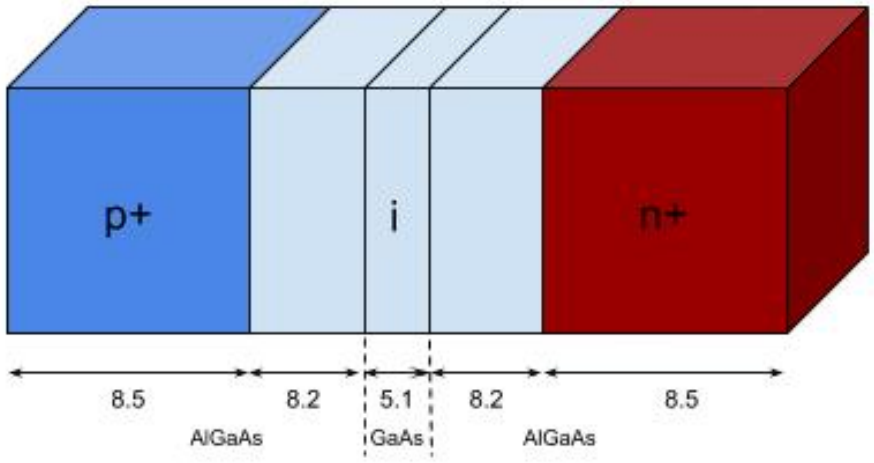

Figure 3-1: *Schematic of the p-i-n diode studied in this section, with all the physical dimensions indicated in nm.*

Table 3-2: Parameters used in the subsequent simulations.

	Parameter	$Al_{0.3}Ga_{0.7}As$	GaAs	Unit
Bandgap energy	E_g	1.77	1.42	eV
Conduction band offset	ΔE_c	0.0	-0.2	eV
Valence band offset	ΔE_v	0.0	0.15	eV
Electron effective mass	m_e	0.0879	0.067	m_0
Hole effective mass	m_h	0.1024	0.082	m_0
static dielectric constant	ϵ	12.2	13.1	ϵ_0
High frequency dielectric constant	ϵ_∞	10.9	10.9	ϵ_0
n-contact doping density	N_d	10^{19}		cm^{-3}
p-contact doping density	N_a	10^{19}		cm^{-3}

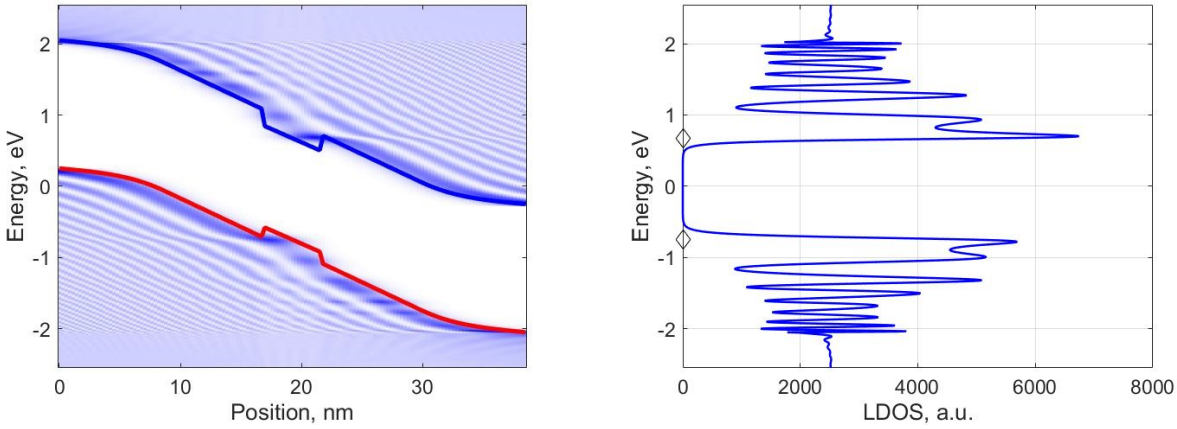

(a) (b)

Figure 3-2: *(a) Local density of states (assuming $k_{||} = 0$) in the ballistic limit, at equilibrium. (b) Cut of the LDOS made at the center of the device, in $x_0 = 19.23$ nm.*

Despite being a very simple example, this kind of structures has been widely investigated in several works [18, 10, 24], and it serves as a good structure to test the capabilities of the NEGF method. Due to the high bandgap of the materials used, simulations using the sp_3s^* model were very resource demanding, so only the sp_z was used to simulate this device. Note also that the bands offsets are included in the Hamiltonian through the potential energy.

3.2.1. Device properties in the ballistic limit

The device above described was first simulated in the ballistic limit, in the absence of any scattering mechanism. The equilibrium band diagram along with the local density of states and the carrier densities are also shown in figures **3-2** and **3-3**, respectively. In the LDOS, the contribution of the transversal wavevectors is not displayed, e.i. $k_{||} = 0$.

Wave functions injected from the contact are partially reflected at the junction and form an interference pattern which is visible along both figures in **3-2**. In the case of 3.2(b), a cut made at $x_0 = 19.23$ nm is displayed, were the interference oscillations are shown to decrease until the continuum region is reached. The two big peaks near the band edge correspond to the confined states that are formed due to the presence of the well, and the energy difference between the fist level in the conduction band and the one in the valence band is approximately 1.55 eV. This fact will be used in the next simulations to exploit the applicability of this device as a photodiode.

Figure **3-4** shows the ballistic spectral current computed for the *p-i-n* device at $V_{bias} = 1.5$ V. In this case continuous horizontal lines are seen along the device length, because states injected by one contacts travel through the device without suffering any energetic

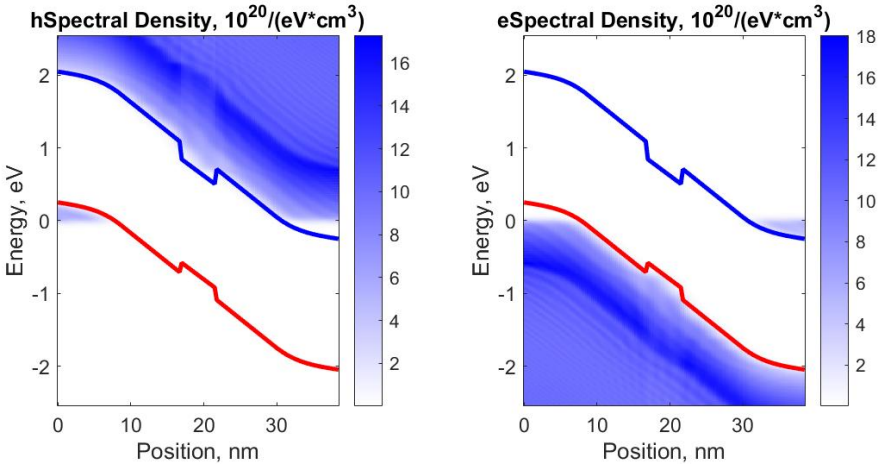

Figure 3-3: *Spectral distribution of carriers along the device, electrons at the right and holes at the left.*

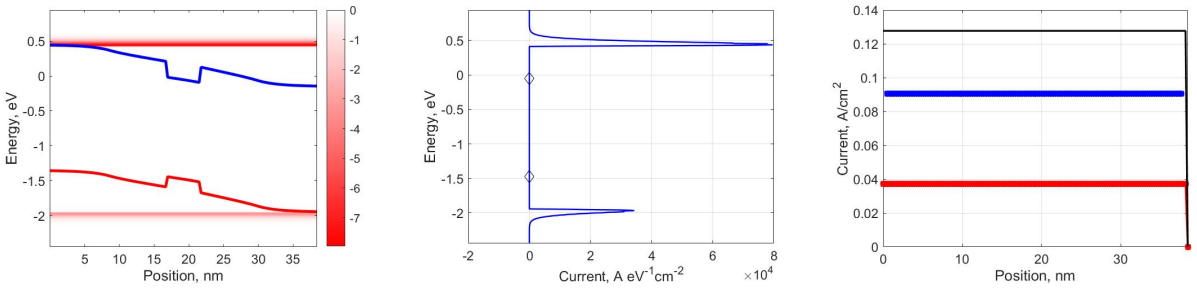

(a) (b) (c)

Figure 3-4: *(a) Spectral current ($A\,eV^{-1}cm^{-2}$) at $V_{bias} = 1.5$ V, in the coherent limit. (b) Cut of the spectral current made at the center of the device, in $x_0 = 19.23$ nm. (c) Electron (blue), hole (red) and total (black) current along the device.*

redistribution process (scattering), hence conserving their same energy as they leave the device at the other contact. This fact can also be noticed in a cut made at any position along the device, e.g. figure 3.4(b) shows a cut made at $x_0 = 19.23$ nm, where two sharp peaks of current are seen, one in the conduction band (electron current) and one in the valence band (hole current). Moreover, injection of carriers can only happen at energies were no reflexion can occur, e.i. above the conduction band maximum and below the valence band minimum. Finally, 3.4(c) shows the total current along the device, with the corresponding contributions of electrons and holes. The ballistic current is constant at every position for both electrons and holes, as imposed by the conservation law stated in (2-114).

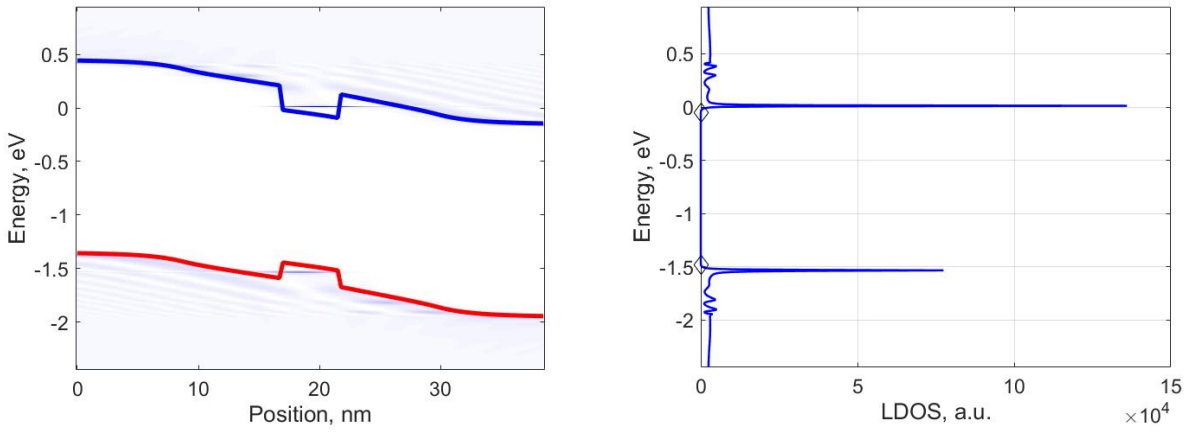

(a) (b)

Figure 3-5: *(a) Local density of states (assuming $k_{||} = 0$) at $V_{bias} = 1.5$ V. (b) Cut of the LDOS made at the center of the device, in $x_0 = 19.23$ nm.*

3.2.2. Device properties including scattering mechanisms

When scattering mechanisms are included in the simulation, several changes can be appreciated in the results obtained. Figure **3-5** shows the LDOS for the device at $V_{bias} = 1.5$ V, and it can be noticed that when the device is close to flat band, the effect of confinement becomes more visible as in 3.5(b) we can observe that the confined state within the well have become very sharp. Due to the reduced dimensions of the device, optical phonon scattering effects cannot be well appreciated in the simulation, as shown in figure 3.6(a) where the spectral distribution of the current flowing trough the device closely resembles that of the ballistic device. However, when the current at the boundaries is plotted, some changes can be observed in the spectral distribution of current components. Figure 3.6(b) displays a cut of the spectral current at the boundaries where carriers are absorbed, and a typical step behavior is noticed due to optical phonon emission as carriers travel through the device. Acoustic phonon scattering result in a slight broadening of the spectra, and successive emission of optical phonons creates these steps in the spectral current, each of these separated by the optical phonon energy $\hbar\omega_{LO} = 40$ meV. Successive scattering with optical phonons have in general the effect of spreading the current distribution, generating satellite peaks of current, which would be much more appreciable in a longer device.

Acoustic and optical phonon scattering conserve the current as can be appreciated in figure 3.6(c) when again the computed current is constant along the device for both electrons and holes. It worth to mention that in general, just the total current is conserved, and not for both electrons and holes; which is particularly the case of the illuminated device, where photogenerated carriers in the well travel to opposite contacts, hence producing an

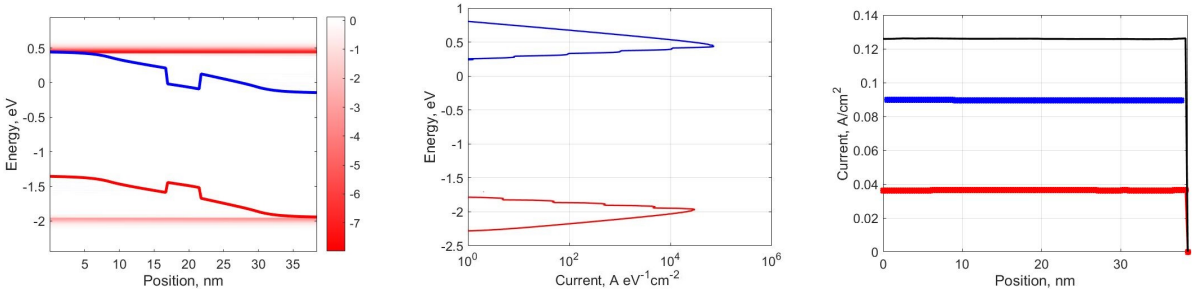

(a) (b) (c)

Figure 3-6: *(a) Spectral current ($A\,eV^{-1}cm^{-2}$) at $V_{bias} = 1.5$ V. (b) Cut of the spectral current made at the contact-device boundary where carriers are absorbed, $x_0 = 38.5$ nm for electrons (blue) and $x_0 = 0$ nm for holes (red). The current is displayed in logarithmic scale. (c) Electron (blue), hole (red) and total (black) current along the device.*

asymmetric flux of carriers at each side.

When illuminating the device, electrons in the valence band can be excited and promoted to the conduction band, producing a net current flux through the device, or *photocurrent*. To study this behavior, the device was illuminated using a monochromatic light source with intensity 10 kW/m^2. Figure **3-7** shows the spectral distribution of current flowing through the device, for different values of the photon energy $\hbar\omega_{op}$. In this case, the device is biased with a voltage $V_{bias} = 1.3$ V, which is a value just below the onset of the diode (the drift current in this case is negligible compared with the induced photocurrent), and the photon energy was varied around 1.55 eV, which is the energy difference between the confined states in the QW, as shown in figure 3.7(d). For $\hbar\omega_{op} = 1.45$ eV, it can be seen that the induced photocurrent is very small, since this energy is not enough to excite the states with the peak in the LDOS, and just the lowest QW states are excited. Lower photon energies induce a negligible photocurrent or are not absorbed at all. On the other hand, when $\hbar\omega_{op} = 1.55$ eV is used, just transitions between the states indicated in figure 3.7(d) are excited, and the resulting photocurrent is very sharp and narrow in energy. Finally, further increasing the photon energy, as done in figure 3.7(c), produces a broadened spectrum of photocurrent, due to excitation of states far away from the gap, spectrum which can be broadened even more as carriers are relaxed due to phonon scattering.

We can further observe where the absorption of photons is taking place, by plotting the divergence of the spectral current from the electron-photon self-energy, or *spectral optical rate* (number of photons absorbed/emitted per unit of time, volume and energy), using equation (2-116). Figure **3-8** shows the spectrally resolved optical rate originated by electron-photon scattering. It can be noticed that the absorption of photons take place just in the well region, and the energies in which absorption take place correspond to those observed above where

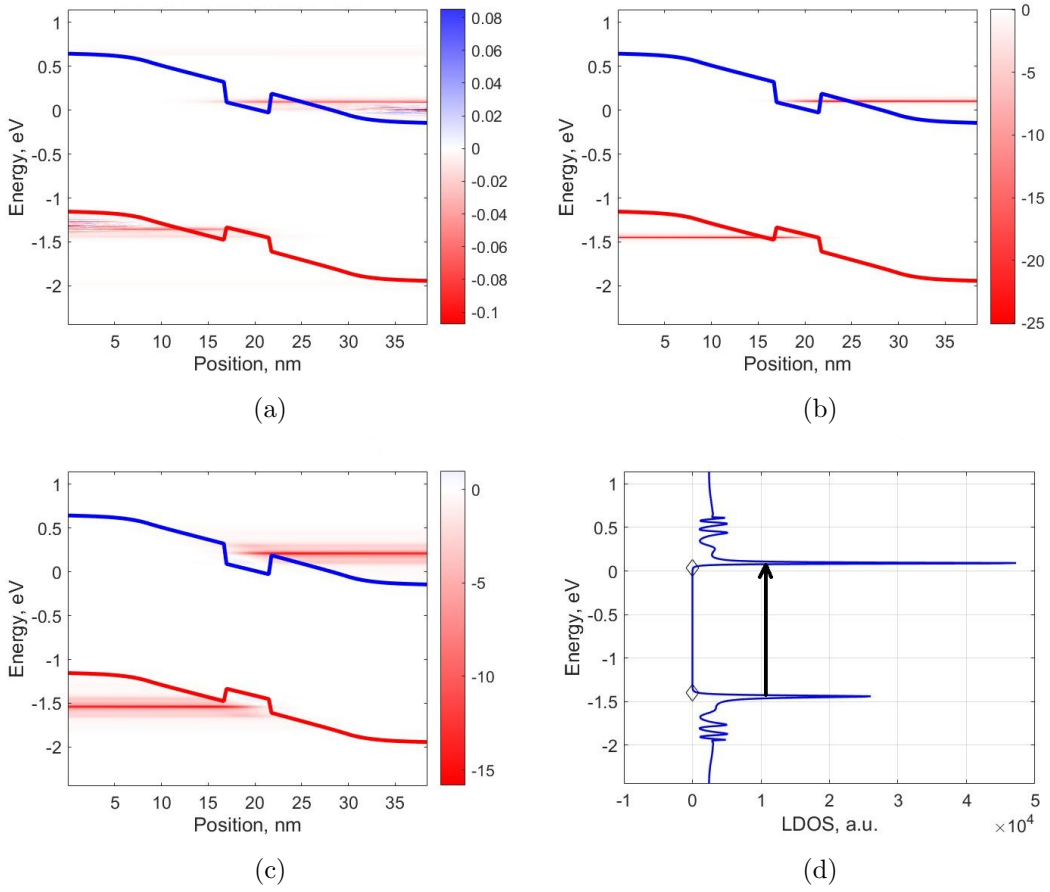

Figure 3-7: *Spectral current ($A\,eV^{-1}cm^{-2}$) at $V_{bias} = 1.3$ V for different values of the energy of the incoming photons: (a) $\hbar\omega_{op} = 1.45$ eV, (b) $\hbar\omega_{op} = 1.55$ eV, and (c) $\hbar\omega_{op} = 1.75$ eV. (d) Cut of the LDOS made at the center of the device, in $x_0 = 19.23$ nm, with the transition between the confined levels indicated.*

the current was flowing. For the case $\hbar\omega_{op} = 1.45$ eV exposed in figure 3.8(a), the absorption takes place between the lowest well levels but the number of transitions is small compared with other two cases and the induced photocurrent is almost negligible, whether for higher photon energies, the spectral range of transition from the valence to the conduction band is wider, hence producing a broadened current spectra.

To conclude the study of this device, we show the extraction efficiency as computed by the following equation [24]

$$\eta_{ext} = \frac{J_{SC}}{J_{abs}}, \tag{3-2}$$

where J_{SC} is the short-circuit photocurrent, and J_{abs} is the bias dependent photocurrent

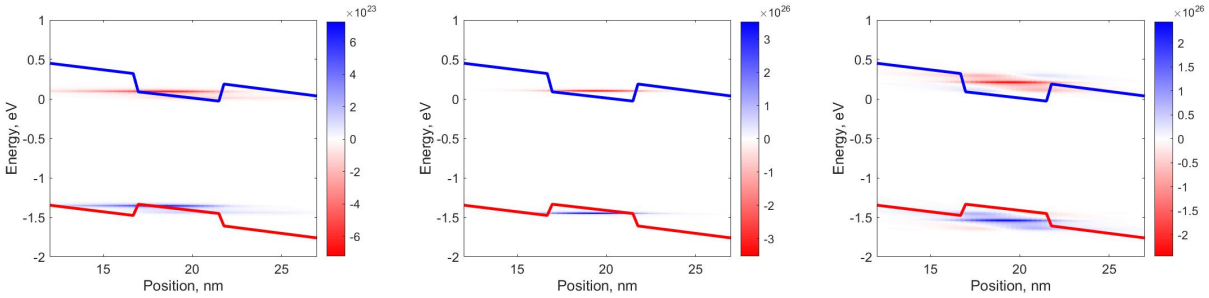

(a) (b) (c)

Figure 3-8: *Spectral optical rate for different photon energies: (a) $\hbar\omega_{op} = 1.45\ eV$, (b) $\hbar\omega_{op} = 1.55\ eV$, and (c) $\hbar\omega_{op} = 1.75\ eV$.*

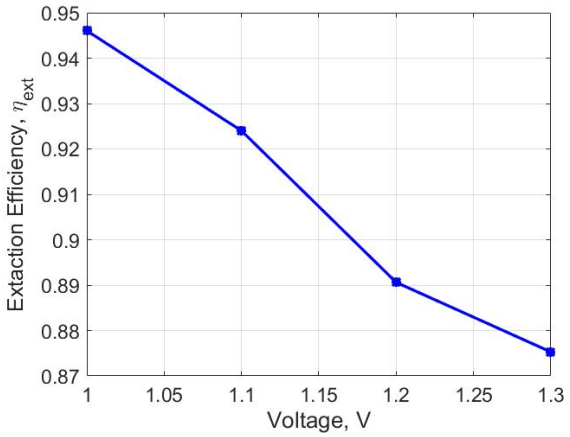

Figure 3-9: *Extraction efficiency η_{ext} as a function of the bias voltage, for the SQW device illuminated with a monochromatic source with $\hbar\omega_{op} = 1.55\ eV$.*

cmputed as $J_{abs} = J_{tot} - J_{Dark}$.

The extraction efficiency is a measure to describe the carrier scape in the device, e.i. how easy is to remove the generated pair from the active area. A decreasing dependence is observed in figure **3-9** between η_{ext} and the applied bias, in accordance with the results shown in [24] for a similar structure. In fact, increasing positively the bias, decreases the built-in field inside the SQW, which works in a detrimental manner for the carrier extraction. On the other hand, higher built-in field help to attract free carriers to the contact in a more effective way, decreasing the probability this carriers recombine before leaving the device.

3.3. Type-two superlattice absorber

As a second example, a type-II superlattice (T2SL) absorber will be analyzed using the NEGF method in the tight-binding basis. This kind of structure is very important for opto-electronic applications as a photodetector, and it has been studied many times before in the literature. Its applications in the mid-infrared (mid-IR) range have been demostrated using inter-band transitions due to the effective badgap that is formed between the quantized levels of the superlattice. Moreover, its ability to tune easily the gap by varying the SL period make it a versatile and precise device to detect a wide range of wavelengths. Some results regarding the absorption spectra of a similar structure are shown by *Qiao et al.* in [25], where the study is made with a $\mathbf{k}\cdot\mathbf{p}$ approach, under periodic (PBC) and Dirichlet boundary conditions (DBC), instead of our open boundary conditions (OBC) as imposed by the boundary self-energies. A further, more complex device using this structure is investigated by *Tian et al.* in [26].

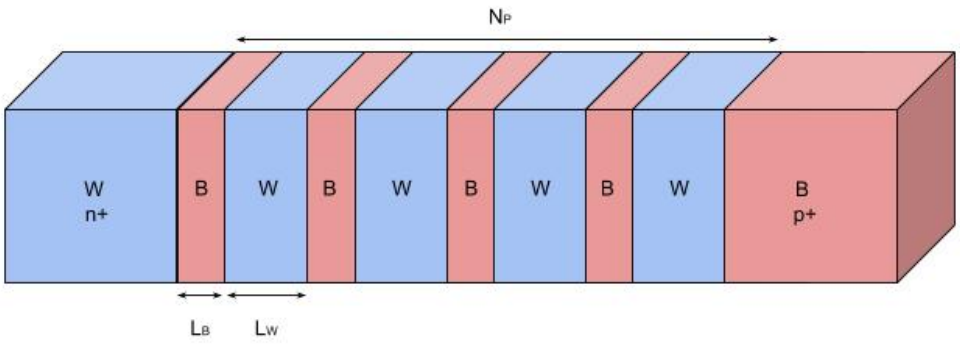

Figure 3-10: *Schematic of the T2SL photodetector studied in this section.*

The structure is an approximately 31 nm Type-II SL, composed of N_p periods of *well* (W) and *barrier* (B) layers made of undoped InAs and GaSb, respectively, and which are sandwiched between two highly doped contacts with $N_a = 10^{17}$ cm^{-3} and $N_d = 10^{18}$ cm^{-3}. The unbalance in the doping levels is just a tool to achieve flat band conditions with no applied bias. The device layout is shown in figure **3-10**, where the dimensions L_B, L_W, and the number of periods were not specified as they will be varied to show some properties of the device. Simulation parameters are also presented in table **3-3**.

Figure **3-11** shows the band structure and the dispersion relation of the energy bands with repsect to the transversal momentum $k = |\mathbf{k}_{||}|$, in a 5 period superlattice with $L_W = 3.65$ nm and $L_B = 1.52$ nm, computed using the TB sp_z model under both PBC and OBC. As expected, in figure 3.11(b) the periodicity of the structure has created evenly spaced (in energy) minibands along the structure, in accordance to what is shown in [25], and each miniband is composed of four sub-bands, with an effective bandgap of 0.388 eV. On the

Table 3-3: Parameters used in the T2SL simulations.

	Parameter	InAs	GaSb	Unit
Bandgap energy	E_g	0.42	0.81	eV
Conduction band offset	ΔE_c	-0.95	0.0	eV
Valence band offset	ΔE_v	-0.56	0.0	eV
Electron effective mass	m_e	0.0224	0.041	m_0
Hole effective mass	m_h	0.0224	0.052	m_0
static dielectric constant	ϵ	15.15	15.7	ϵ_0
High frequency dielectric constant	ϵ_∞	12.3	14.4	ϵ_0
n-contact doping density	N_d	10^{18}		cm^{-3}
p-contact doping density	N_a		10^{17}	cm^{-3}

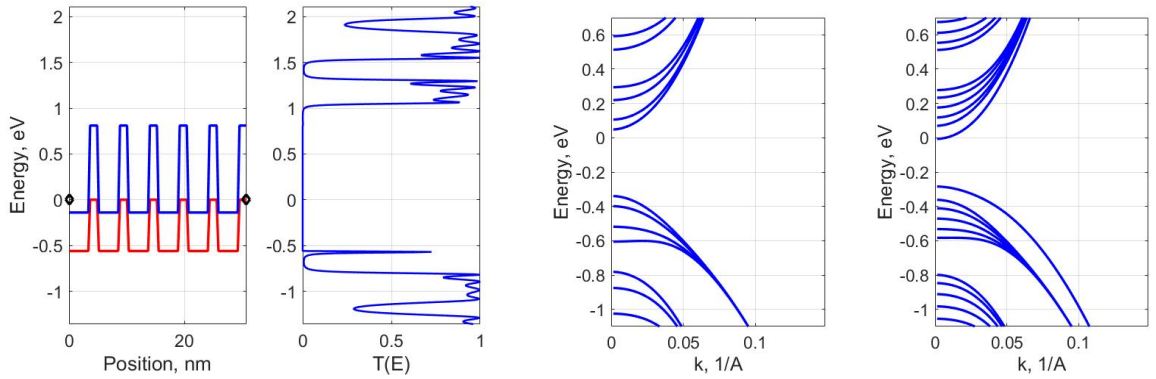

(a) (b) (c)

Figure 3-11: *(a) Band diagram of the T2SL structure, with the left to right transmission probability at the right side. Contact Fermi levels are marked with diamonds. The energy dispersion is also shown, computed with (b) PBC and (c) OBC.*

other hand, when attaching the finite periodic structure to the infinite leads, e.i. imposing OBC, we experience, among the main differences, the appearance of one more band on each miniband, and two new bands also show up inside the main gap, which decrease the effective bandgap of the structure to about 0.277 eV. As we will show later, this two bands are an effect of the contacts attached to the structure, but they are not visible within the periodic part of the device, hence giving an effective gap of approximately 0.42 eV for the device with OBC. This energy correspond to a wavelength in the order of 2.96 μm which make the device suitable to detect wavelengths in the mid-IR light range.

Figure **3-12** shows the LDOS along the device, with a cut on the middle of the structure shown on the right. Here the minibands are clearly visible, and the sub-bands have been labeled with the symbols c_1-c_5 (c_2 and c_4 are not shown, but correspond to the small peaks in

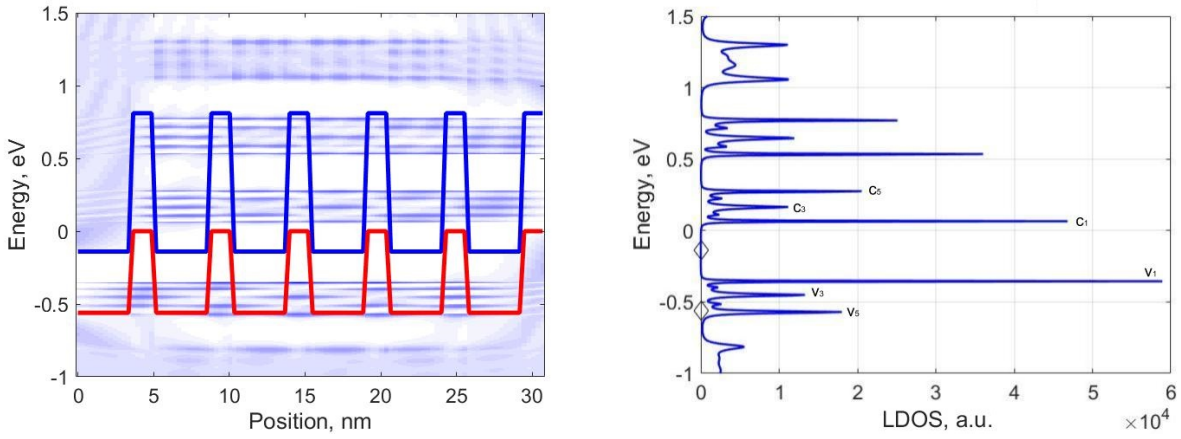

(a) (b)

Figure 3-12: *(a) Local density of states (assuming $k_{||} = 0$) at equilibrium. (b) Cut of the LDOS made at the center of the device, in $x_0 = 15.35$ nm.*

between c_{1-3-5}) for the ones in the conduction miniband and v_1-v_5 for the valence miniband. As it will be shown in a moment, miniband formation occur due to the superposition and coupling of the localized levels of the wells, hence giving rise to peaks in the density of states which coincide with the number of periods included in the structure (also with the number of subbands on each miniband). In fact, the effective bandgap of the device can be tunned by changing the well thicknesses (conduction and valence band wells), hence moving the position of the ground states of the wells. Due to the effect of the open boundaries and interaction with phonons, localized states appear like broadened peaks, since carriers in those states are not confined but posses a finite lifetime, and further resonances can be observed higher in the LDOS due to the presence of the wells, which give rise to additional minibands.

At this point, different transitions can be tested by illuminating the SL structure, and finally the photocurrent response of the device can be obtained. Figure **3-13** shows the spectral current on the SL for different values of the incoming photon energies, using as illuminating source monochromatic light with intensity 10 kW/m^2. First we considered a small value of $\hbar\omega_{op} = 0.1$ eV, which is enough to promote transitions form c_1 to c_3, but due to the small population of the sub-band c_1, just a small resulting photocurrent is observed, in figure 3.13(a). Moreover, absorption only takes place near the n-contact (left side) where this band has a higher concentration of electrons.

For the case of figure 3.13(b), a photon energy of $\hbar\omega_{op} = 0.28$ eV was used, close to the value of the energy gap observed in figure 3.11(c), and some current can be seen to traverse the SL, with a discontinuity in the spectral lines close to the right contact, suggesting that photon absorption takes place there. In fact, this behavior is confirmed when observing the spectral

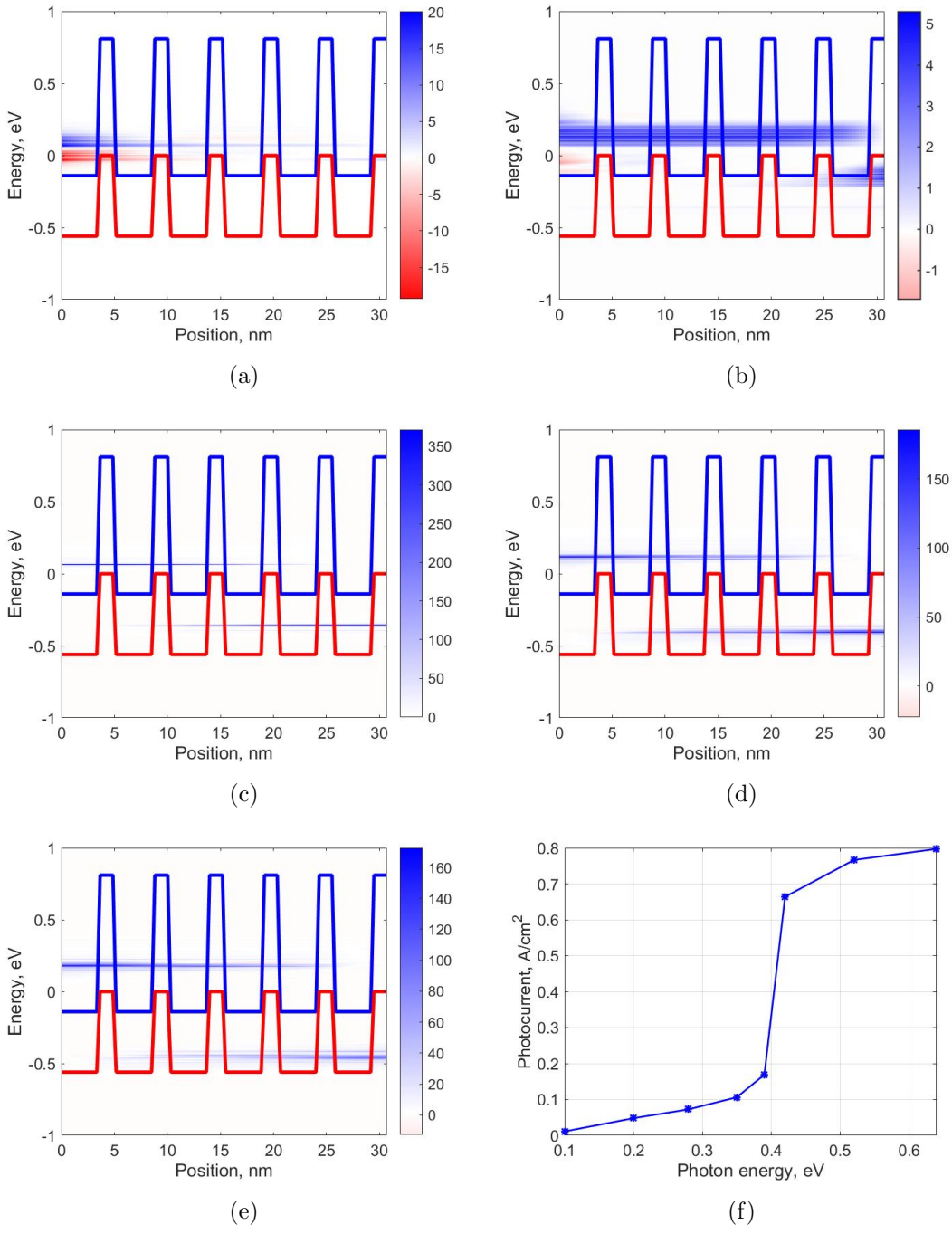

Figure 3-13: *Spectrally resolved photogenerated current ($A\,eV^{-1}cm^{-2}$) for the device at zero bias for different photon energies: (a) $\hbar\omega_{op} = 0.1\ eV$, (b) $\hbar\omega_{op} = 0.28\ eV$, (c) $\hbar\omega_{op} = 0.42\ eV$, (d) $\hbar\omega_{op} = 0.52\ eV$, and (e) $\hbar\omega_{op} = 0.64\ eV$. (f) Photogenerated current as a function of the incoming photon energy.*

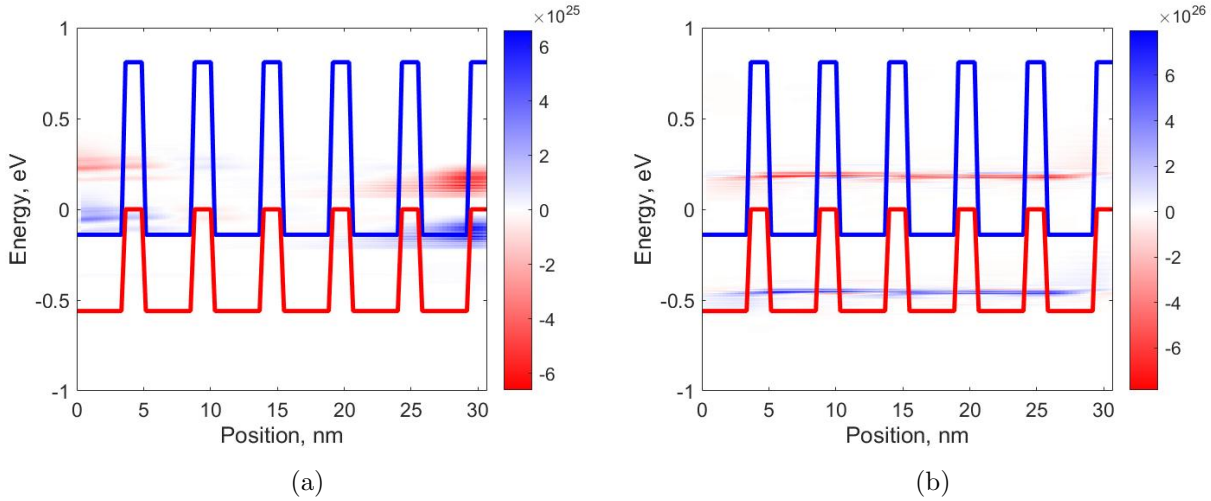

Figure 3-14: *Spectral optical rate at: (a)* $\hbar\omega_{op} = 0.28\ eV$ *and (b)* $\hbar\omega_{op} = 0.64\ eV$.

optical rate which is plotted in 3.14(a), where the places where absorption takes place are shown to be the regions close to the contacts, which are affected by the bulk density of states at this two sides and hence producing the observed extra bands plotted in 3.11(c). However, this energy does not correspond to the absorption edge of the structure as observed in figure 3.13(f), being the photocurrent still small due to absorption of photons limited to a small portion of the hole structure.

Finally, values of $\hbar\omega_{op} = 0.42, 0.52, 0.64$ eV were used to observe transitions from valence to conduction miniband, and the spectral current in those cases can be observed in figures 3.13(c), 3.13(d) and 3.13(e), respectively. This energy values correspond to the transitions v_1-c_1 in the case of 0.42 eV, v_1-c_3 in the case of 0.52 eV and v_1-c_5 or v_3-c_3 in the case of 0.64 eV, as they can be clearly seen in the location of the spectral lines of current. As shown in figure 3.14(b), where the spectral optical rate at 0.64 eV is plotted, the absorption of photons takes place though the entire superlattice structure, as opposed to what was observed in 3.14(a). The obtained photocurrent as a function of the incoming photon energy is also plotted in figure 3.13(f), where an increasing behavior of the photocurrent can be observed with increasing photon energy. As expected, the current has a step increase once the photon energy is equal to 0.42 eV, which correspond to the energy gap, and starts to become constant once the photon energy is high enough to cover the entire conduction miniband, e.i. no more transitions will occur at higher photon energies. This behavior just reflect the density of states participating on the optical transitions.

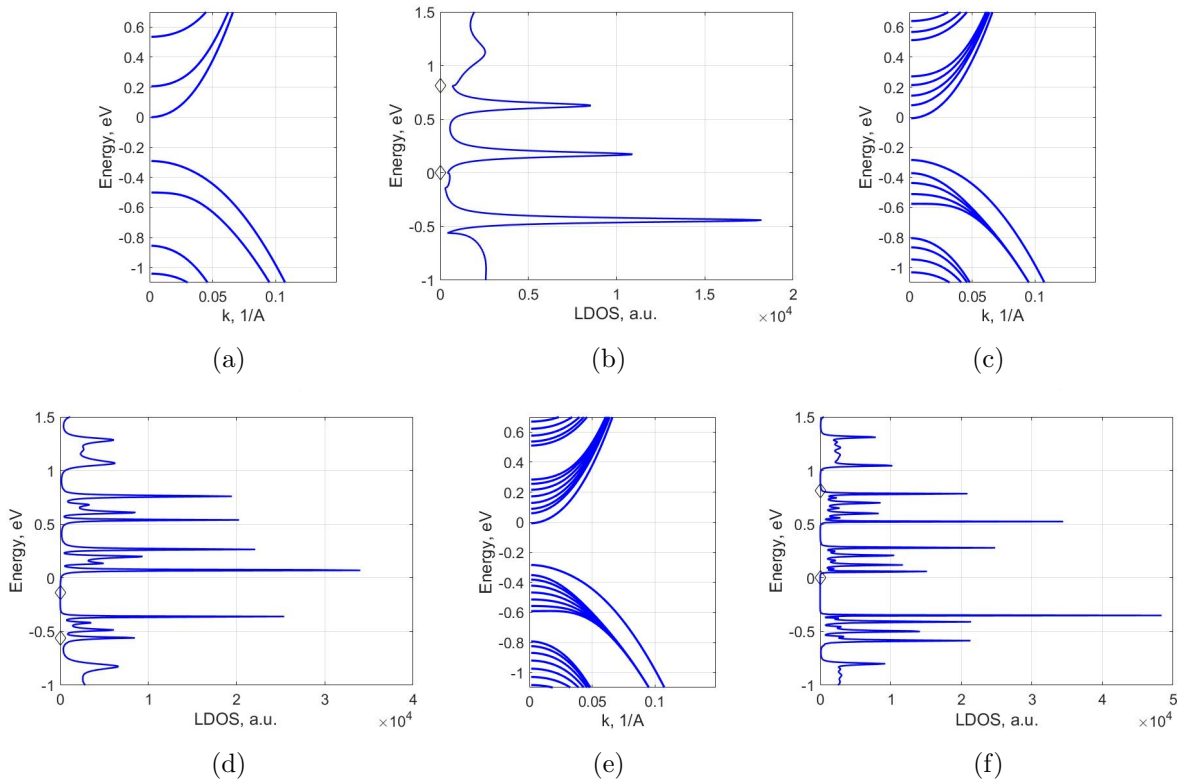

Figure 3-15: *Energy dispersion and LDOS ($k_{||} = 0$) at the middle of the structure for the T2SL with different number of periods: (a) and (b) $N_p = 1$, (c) and (d) $N_p = 4$, and (e) and (f) $N_p = 7$.*

3.3.1. Effect of geometrical parameters on the SL

Deeper understanding of this structure can be obtained by varying its geometrical parameters and observing the spectral quantities. As a first example, miniband formation can be seen when observing at the LDOS as the number of periods in the superlattice is increased. Each InAS-GaSb period produces a well for both conduction and valence band, and confined states are formed inside the well (See figure 3.15(b), where two confined states reside in the conduction band well, whereas there is just one in the valence band well). When attaching this structure to open boundaries, this states are not confined anymore, but acquire a finite width corresponding to a finite carrier lifetime, since this carriers can now scape through the open contacts. Away from the well top energy, the density of states resembles that of the continuum, with some resonances corresponding to further states arising from the well below.

As seen in figure 3.15(d), adding more periods to the superlattice results in an equal increase in the number of peaks on each miniband, which is consequence of the coupling of the

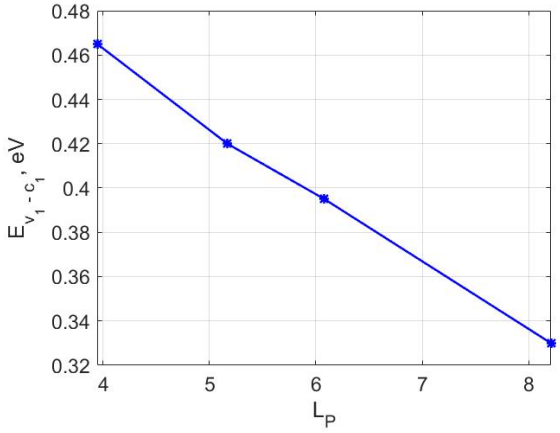

Figure 3-16: *Energy gap between valence and conduction minibands as a function of the period length L_P in nm. The ratio L_B/L_W is kept constant and equal to 4/9.*

confined states of the different wells. On figure 3.15(f), where the structure has 7 periods, the minibands are clearly formed, with sharp edges at the sides. It can be noticed that both, the v_1-c_1 energy (energy between first peaks on valence and conduction band) and the miniband widths are almost not modified as the number of periods increase. As mentioned before, this is a consequence of the fact that the well width is kept constant in this case, therefore, the spectral location of the quasi-bond states inside the well is not modified.

On the other hand, by increasing (decreasing) the well widths, the the position of the minibands can be moved to lower (higher) energies, hence changing the effective gap and in this way tunning the cutoff wavelength absorbed by the SL absorber. One example of this is shown in figure **3-16**, where the absorber v_1-c_1 gap is changed by varying the period length L_P, maintaining the constant the ratio $L_B/L_W \approx 4/9$. In this way, an increase in the period length produce an increment in the barrier and well lengths, therefore moving the ground levels to lower energies as shown in the decremental behavior of the graph.

3.4. Tunneling junction

Tunneling junctions (TJ) are important structures used in solar cells to match electron and hole currents from heterojunction subcells that are connected in series. The matching of these currents is made by means of interband tunneling and recombination of carriers, phenomenon which will be studies in this last example using the NEGF approach, within the TB sp_z band model. In particular, two structures were studied: a bulk TJ made of a heavily doped $In_{0.52}Al_{0.33}Ga_{0.15}As$ p-n ($N_{a,d} = 10^{19} cm^{-3}$) junction attached to doped $In_{0.52}Al_{0.33}Ga_{0.15}As$ and $In_{0.53}Ga_{0.47}As$, p and n contacts, respectively; and a double quantum well TJ (DQWTJ) which consist of the same structure of the bulk TJ, with two wells made of $In_{0.53}Ga_{0.47}As$

inserted in the *p-n* junction region. These structures, which are shown in figure **3-17**, were studied experimentally by *Lumb et al.* in [27] and subsequently tested with the NEGF approach by *Aeberhard* in [28]. They constitute a very good example to test our NEGF implementation in order to observe phonon-assisted tunneling, as the structure of these devices is made such that energetic states available for tunneling are unaccessible for ballistic carriers coming from the contacts.

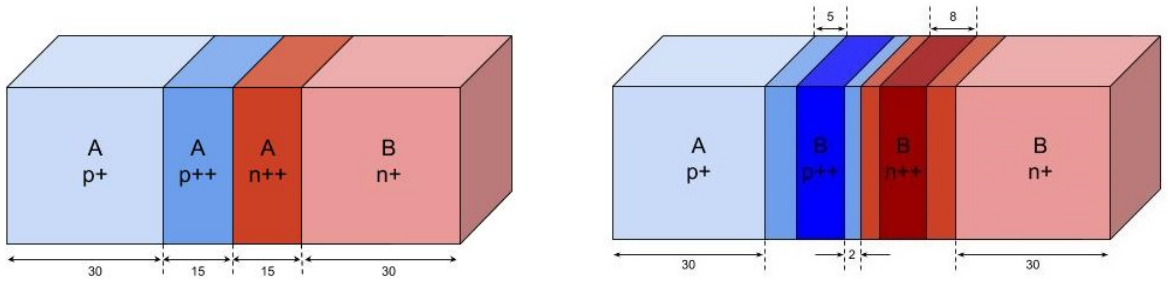

(a) (b)

Figure 3-17: *Schematic layout of the structures studied in this section: (a) Bulk TJ (b) DQWTJ. Physical dimensions are given in nm.*

Table 3-4: Parameters used in the tunnel junctions simulations.

	Parameter	InAlGaAs	InGaAs	Unit
Bandgap energy	E_g	1.18	0.74	eV
Conduction band offset	ΔE_c	0.3	0.0	eV
Valence band offset	ΔE_v	-0.14	0.0	eV
Electron effective mass	m_e	0.065	0.041	m_0
Hole effective mass	m_h	0.087	0.052	m_0
static dielectric constant	ϵ	13.2	14.2	ϵ_0
High frequency dielectric constant	ϵ_∞	10.7	11.0	ϵ_0
n-contact doping density	N_d		2×10^{17}	cm^{-3}
p-contact doping density	N_a	2×10^{17}		cm^{-3}

Figures 3.18(a) and 3.18(b) show the band diagrams, along with the local density of states ($k_{||} = 0$) at 0.06 V and 0.16 V bias voltage, for both the bulk TJ and the DQWTJ, respectively. High built-in field induced at the *p-n* junction interface in 3.18(a) produce a pronounced band bending which in turn generate confined states at the vicinity of the junction. The presence of open boundaries broaden the spectrum this states, generating quasi-bond states due to a finite scape probability acquired by the confined carriers. Such states, both in

valence and conduction band, overlap in energy and are suitable to produce interband tunneling current. However, they are not accessible from contact states, so phonon relaxation is needed for carriers to be able to reach this energy levels. As seen from figure **3-18**, which also shows the spectrally resolved electron-phonon scattering rate for both TJ structures at 1.6 V and 3.1 V bias, respectively; most of the phonon scattering events occur within the potential wells formed by doping induced band bending, as ballistic carriers injected from the contacts relax until they reach the lowest well levels and subsequently tunnel to the other band. Once they tunnel, optical phonon absorption give them enough energy to scape to the other contact, hence generating a net current. This behavior make imperative to include (optical) phonon scattering in the simulation in order to accurately analyze the device, as a oversimplified ballistic approach would underestimate the current due to the vanishingly small ballistic energy overlap at small (positive) bias.

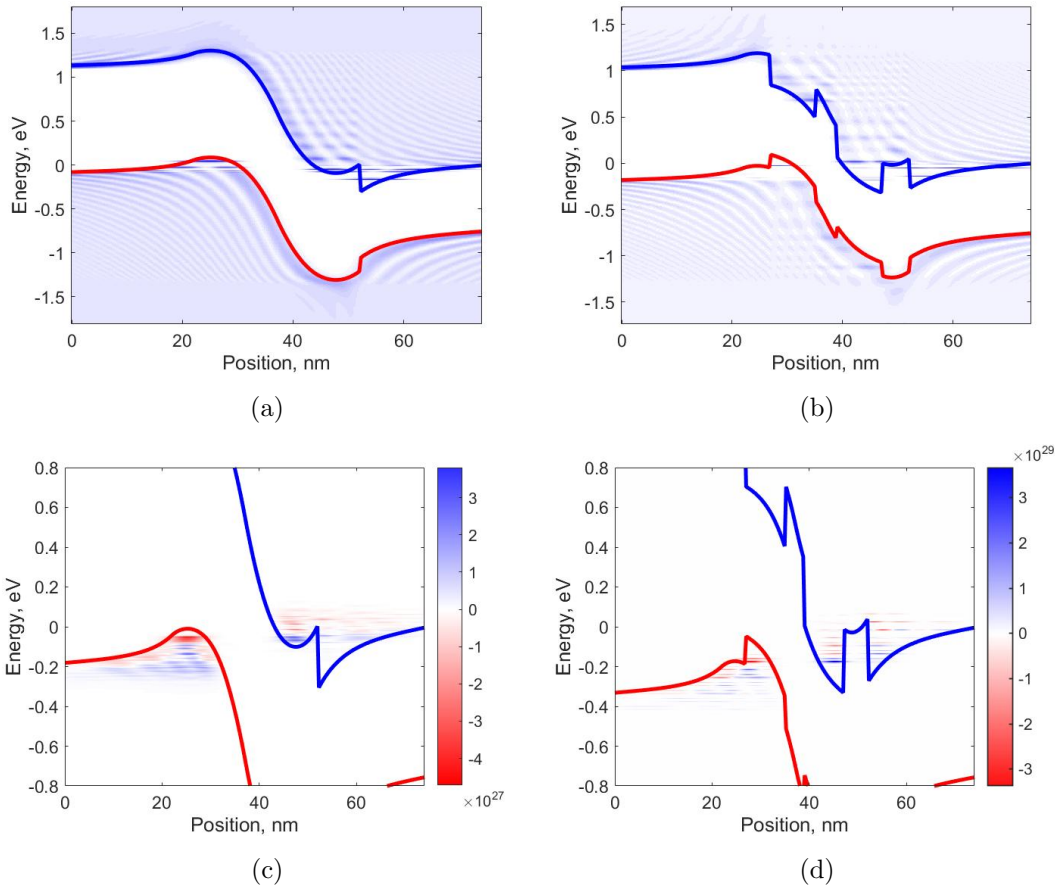

Figure 3-18: *Spectrally resolved local density of states ($k_{||} = 0$) for (a) Bulk TJ at $V_{bias} = 0.06$ V and (b) DQWTJ at 0.16 V. Spectrally resolved electron-phonon scattering rates ($cm^{-3}s^{-1}eV^{-1}$) for (a) the bulk TJ at $V_{bias} = 1.6$ V, and (b) the DQWTJ at $V_{bias} = 3.1$ V.*

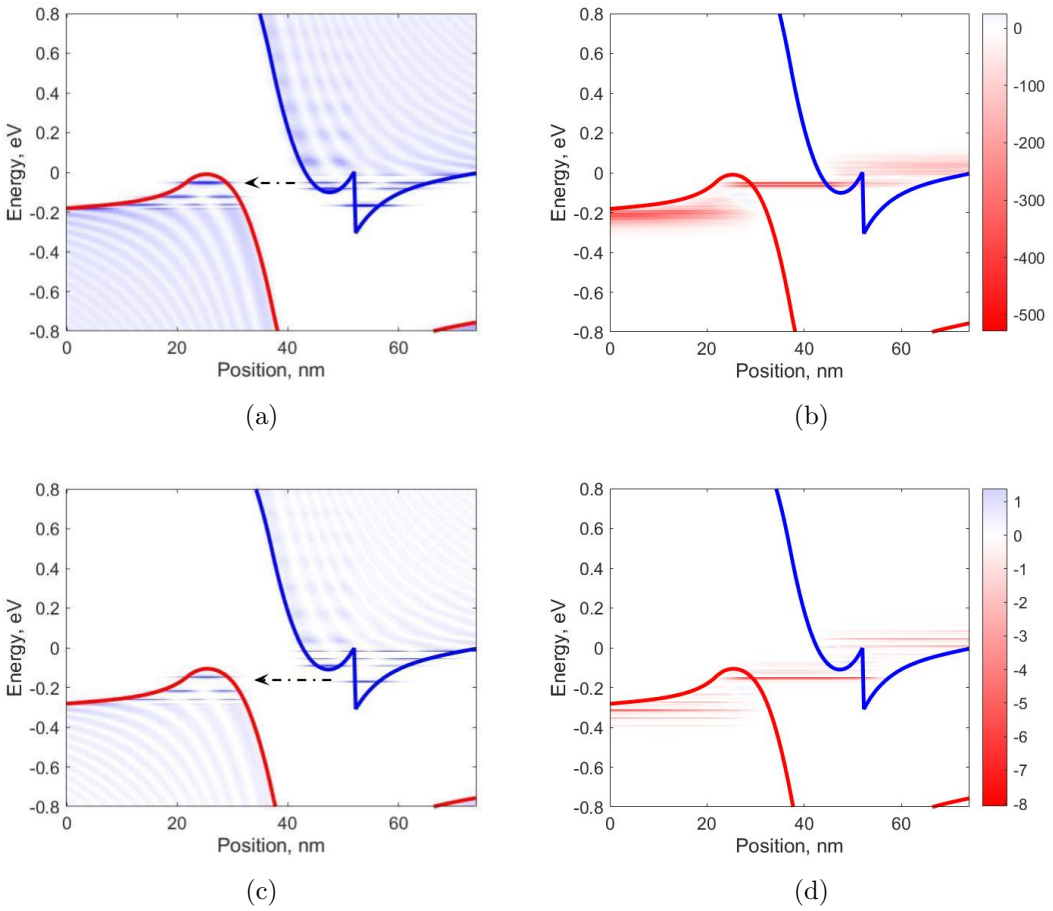

Figure 3-19: *Local density of states ($k_{||} = 0$) and spectrally resolved current density ($A\,cm^{-2}eV^{-1}$) for the bulk TJ structure at: (a) and (b) $V_{bias} = 0.16$ V, (c) and (d) $V_{bias} = 0.26$ V.*

When applying a small positive bias to the bulk TJ structure, a small energy overlap still exist to produce tunneling current. Moreover, localization of the energy levels within the wells in the vicinity of the junction suggest a resonant behavior of the current, when the applied bias is such that this levels align. Figure **3-19** shows the bulk TJ under applied bias of 1.6 and 2.6 V. In 3.19(a) bottom well levels are aligned (an arrow designates the aligned levels) and a net tunneling current traverses the device through this energy. Further increasing the bias to 2.6 V in 3.19(c), we see that the bottom level of the triangular well at the heterojunction interface is now aligned with the top level in the valence band, with a net current flowing through this energy. Some current is also observed coming from the bottom subband of the conduction band well, through phonon-assisted tunneling. The current observed in this case is smaller compared to the case with smaller bias because the energy overlap has decreased, limiting the energy range in which tunneling can occur; and also carriers coming from the

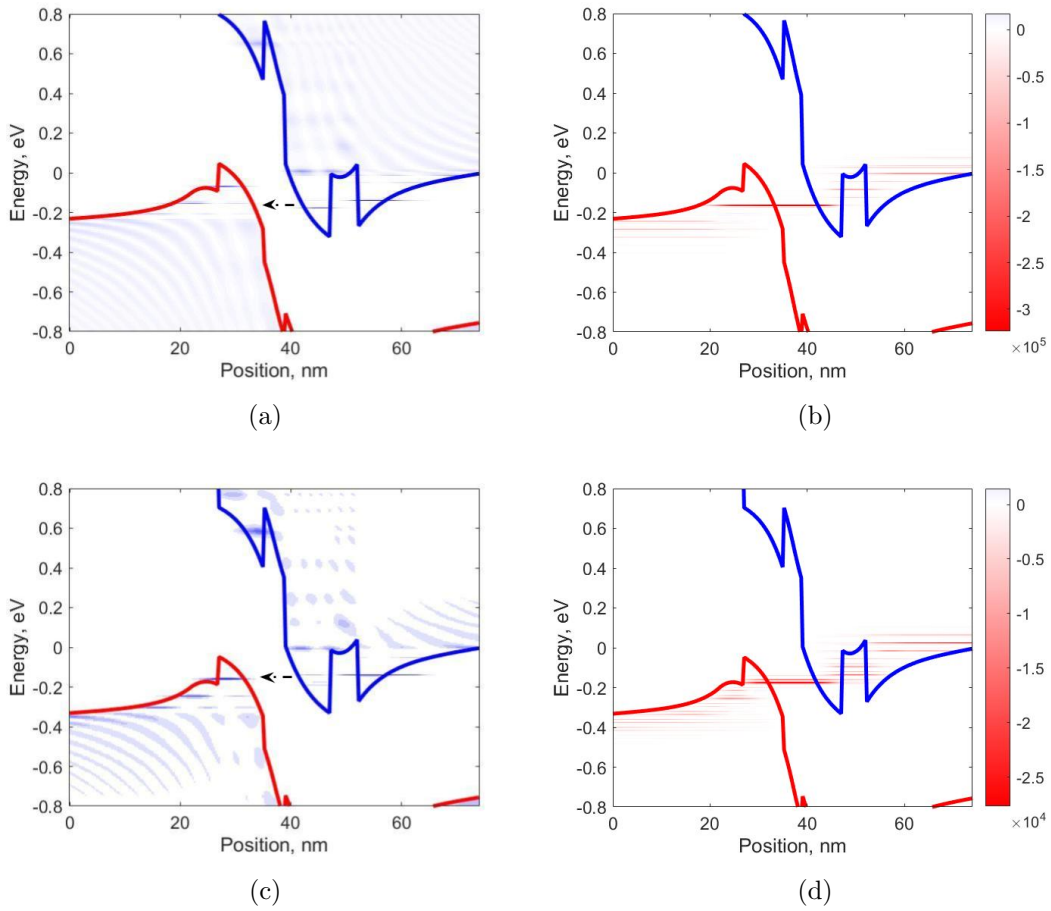

Figure 3-20: *Local density of states ($k_{||} = 0$) and spectrally resolved current density ($A\,cm^{-2}eV^{-1}$) for the DQWTJ structure at: (a) and (b) $V_{bias} = 0.21$ V, (c) and (d) $V_{bias} = 0.31$ V.*

n-contact and tunneling through the triangular well level have to traverse a longer barrier thickness, decreasing their transmission probability. Increasing further the bias, produces no direct tunneling, so the remaining current is due to phonon-assisted tunneling, and it decreases exponentially as the voltage keeps growing.

In the case of the DQWTJ, conduction is dominated by the presence of the quantum well levels, and increased current peaks can be observed due to confinement enhanced localization of the levels. It is also remarkable from this structure that the presence of the wells increase energy overlapping and decrease the thickness of the tunneling barrier. As a result, a higher net current traverses the device withing a longer bias range before the net overlapping vanishes. The response of the device when a bias is applied can be observed in figure **3-20**, where the local desnity of states and the spectral current are plotted for two values of the applied bias. In both cases, transport of electrons from the conduction band occur

mainly through the triangular well level to the second QW subband, and succesive phonon relaxation to the first well subband. When a 2.1 V bias voltage is applied, electrons tunnel to the second QW subband in the valence band, while when increasing the voltage to 3.1 V, they tunnel to the topmost well level in the valence band. Orders of magnitude of the tunneling current are much higher than in the previous case.

It is also remarkable form the spectral current plots for both Bulk TJ and DQWTJ that current transport is manly done through narrow lines instead of a broadened current spectra, even at the contacts (where the density of states resembles that of the bulk, therefore allowing carriers to propagate in a continuous spectra). This is due to the energetically narrow bands present in the well structures (specially in the case of the DQWTJ) through which current is transported between conduction and valence bands. Such narrow distribution of current suffer sequential scattering events with optical phonons, that in turn generate spectral lines of current through the device separated in energy by $\hbar\omega_{LO}$ spaces. Further analysis of this structures can be found in [24], in which the absorption spectra of both TJ structures is analyzed, but this discussion goes beyond the scope of this work.

3.5. Improving the NEGF model

3.5.1. Reduced order model

Computational complexity of the NEGF model make the use of multiband models a challenging task, due to the huge amount of memory required and the exponential number of arithmetic operations that need to be performed. In this section we propose a novel approach to solve this problem, based on the low rank approximation (LRA) method, which basically consist in projecting the the Green's functions (Dyson's and Keldysh equations) into a lower-order suitable basis set. The basis functions should resemble the eigenstates of the nanostructure that is going to be analyzed, and should be orthogonal so that they will not increase the computational complexity in the calculation of scattering self-energies. Such a basis set can be obtained for example by finding the eigenstates of the noninteracting Hamiltonian $\mathbf{H}_0$, and then moving to a orthogonal basis set by diagonalizing the position operator (this is the exact procedure used to find maximally localized Wannier functions [29]). In order to reduce the dimension of the final basis, just a subset of eigenstates of the noninteracting Hamiltonian is selected, covering energies within a range that span all the conductive channels in the conduction/valence band (several k_BT above and below the highest and lowest leads chemical potentials, respectively). We will call *near* basis function referring to those spanning the subset of interest, and *remote* basis functions, to those not included in the definition of the reduced basis set.

Previous attempts have been made before in implementing the LRA method to improve

NEGF computations [30] obtaining very good results in terms of time and memory optimization. However, the main issue of this approach is that neglecting a subset of the mode space produce an incomplete representation of the system, specially in the case of the boundary self-energy, as some information is discarded in order to simplify the computation (some of the bulk modes from $\mathbf{H}_0$, present in the definition of the boundary self-energy, may be lost). The main consequence of this is that the current conservation is violated, even in the ballistic case, presenting fluctuations that are clearly visible, specially at the device contacts. The approach we will describe solves this issue by a folding procedure, similar to what is employed in real space to eliminate leads from the simulation domain. The idea is to fold the *remote* basis functions, and in this way, at some extent, take into account its influence in the device properties.

To apply our reduce order model the procedure will be divided in some steps we will describe below. First, the problem-matched (orthogonal) basis functions should be computed, from which we start from our original finite basis $\{\phi_\nu(\mathbf{r})\}$[1] (of dimension N) and compute the eigenvalues of the noninteracting Hamiltonian $\mathbf{H}_0 = \mathbf{H}(\mathbf{k} = \mathbf{0})$, by solving the Schrödinger equation

$$\mathbf{H}_0\psi_i = \mathbf{M}E_i\psi_i. \tag{3-3}$$

with $\mathbf{M}$ the overlap matrix as defined in (2-38), $i = 1 \dots N$ is an integer labeling the eigenvalues E_i.

When $\mathbf{M} \neq \mathbb{1}$ ($\mathbf{k}\cdot\mathbf{p}$ case), Löwdin symmetric orthogonalization procedure should be applied before solving the system, in order to transform the generalized eigenvalue problem (3-3) into a standard eigenvalue problem, by defining[2] $\mathbf{R} = \mathbf{M}^{1/2}$ and $\mathbf{S} = \mathbf{M}^{-1/2}$, hence obtaining

$$\mathbf{H}_0'\psi_i' = E_i\psi_i', \quad \mathbf{H}_0' = \mathbf{S}\mathbf{H}_0\mathbf{S},\ \psi_i' = \mathbf{R}\psi_i. \tag{3-4}$$

This step eliminates the need of having two representations (covariant and contravariant, see chapter 2.2) for the Green's functions and self-energies due to the non-orthogonality of the basis. The eigenstates ψ_i' should be subsequently partitioned into remote and near basis sets, according to the proximity of their respective eigenvalue E_i to some value E_0 lying in the middle of the energy range considered. Hence, we will end up with two new sets: the near basis set $\{\psi_i'\}_n$ with n_{eig} elements (n_{eig} should be properly chosen such that enough eigenenergies are included in the near set, so they span an energy range covering few k_BT above/below the highest/lowest chemical potential at the contacts), and the remote basis

[1] This basis functions refer to planar orbitals (2-84) in the case of tight binding, or finite-element zone center Bloch functions (2-117), in the case of $\mathbf{k}\cdot\mathbf{p}$.

[2] Remember that matrix $\mathbf{M}$ is symmetrical. Moreover, in a finite element discretization, such as $\mathbf{k}\cdot\mathbf{p}$, this matrix is real. Therefore, $\mathbf{M}$ is diagonalizable and its square root is well defined. In fact, it can be easily found by taking the square root of the diagonal matrix.

set $\{\psi_i'\}_r$ with $N - n_{eig}$ elements. Define also the matrices $\mathbf{T}_n$ and $\mathbf{T}_r$, which contain in their columns the vectors from near and remote basis sets, respectively.

We now proceed to diagonalize the position operator in both near and remote basis representation to obtain maximally localized basis functions $\psi_{n,j}^{ML}$ and $\psi_{n,l}^{ML}$ such that

$$\hat{\mathbf{X}}_n \psi_{n,j}^{ML} = x_{n,j}\, \psi_{n,j}^{ML}, \quad \hat{\mathbf{X}}_n = \mathbf{T}_n^\dagger \mathbf{S} \hat{\mathbf{X}} \mathbf{S} \mathbf{T}_n, \tag{3-5a}$$

$$\hat{\mathbf{X}}_r \psi_{r,l}^{ML} = x_{r,l}\, \psi_{r,l}^{ML}, \quad \hat{\mathbf{X}}_r = \mathbf{T}_r^\dagger \mathbf{S} \hat{\mathbf{X}} \mathbf{S} \mathbf{T}_r, \tag{3-5b}$$

where $j = 1 \ldots n_{eig}$, $l = 1 \ldots N - n_{eig}$. The position operator $\hat{\mathbf{X}}$ (in the original basis) has been moved to the Löwdin basis through the symmetric multiplication with matrix $\mathbf{S}$, and then to either near or remote basis through transformation matrices $\mathbf{T}_n$ or $\mathbf{T}_r$, respectively.

In our new set of maximally localized basis functions $\{\psi_{n,j}^{ML}\}$, the new coordinate system is given by the eigenvalues of the position operator $x_{n,j}$. By taking transformation matrices $\mathbf{P}_n$ and $\mathbf{P}_r$, which contain in their columns vectors $\psi_{n,j}^{ML}$ and $\psi_{r,j}^{ML}$, respectively, a transformation matrix $\mathbf{Q}_n = \mathbf{S}\mathbf{T}_n\mathbf{P}_n$ ($\mathbf{Q}_r = \mathbf{S}\mathbf{T}_r\mathbf{P}_r$) can be defined, moving from the original basis to the maximally localized near (remote) basis. At this point, boundary self-energies and noninteracting Green's function should be moved to the near basis before starting the NEGF inner loop. In order to take into account the effect of the remote basis in the simulation, the remote basis can be folded into the near one in a similar way as was done for the boundary self-energies in (2-66). To see this, consider the following transformation[3]

$$\begin{pmatrix} \mathbf{Q}_n^\dagger \\ \mathbf{Q}_r^\dagger \end{pmatrix} \mathbf{A} \begin{pmatrix} \mathbf{Q}_n & \mathbf{Q}_r \end{pmatrix} = \begin{pmatrix} \mathbf{Q}_n^\dagger \mathbf{A} \mathbf{Q}_n & \mathbf{Q}_n^\dagger \mathbf{A} \mathbf{Q}_r \\ \mathbf{Q}_r^\dagger \mathbf{A} \mathbf{Q}_n & \mathbf{Q}_r^\dagger \mathbf{A} \mathbf{Q}_r \end{pmatrix} = \begin{pmatrix} \mathbf{A}_n & \mathbf{A}_{nr} \\ \mathbf{A}_{rn} & \mathbf{A}_r \end{pmatrix}, \tag{3-6}$$

with $\mathbf{A} = E\mathbf{M} - \mathbf{H} - \mathbf{\Sigma}^{RB}$ the inverse of the noninteracting Green's function (in the original real-space basis), $\mathbf{A}_n$ and $\mathbf{A}_r$ in the near and remote basis, repectively.

The term $\mathbf{A}_r$ and the cross terms $\mathbf{A}_{nr}$ and $\mathbf{A}_{rn}$ can be used to fold the influence of the remote basis, by defining an extra (remote) self-energy term in the following way

$$\mathbf{\Sigma}^{R,r} = \mathbf{A}_{nr} \mathbf{A}_r \mathbf{A}_{rn}, \tag{3-7}$$

so that the effect of the remote basis terms is taken into account in an effective way. For the noninteracting Green's function in the near basis we finally obtain

$$\mathbf{G}^{R,n} = \left[\mathbf{A}_n - \mathbf{\Sigma}^{R,r} \right]^{-1}. \tag{3-8}$$

From this point on the procedure follows as usual, scattering self-energies are calculated in the near basis. At the last step, the Green's functions should be transformed back to the

[3]Note that the matrix product here is well defined. $\mathbf{Q}_n$ is a $N \times n_{eig}$ matrix, $\mathbf{Q}_r$ is $N \times N - n_{eig}$ and $\mathbf{A}$ is $N \times N$.

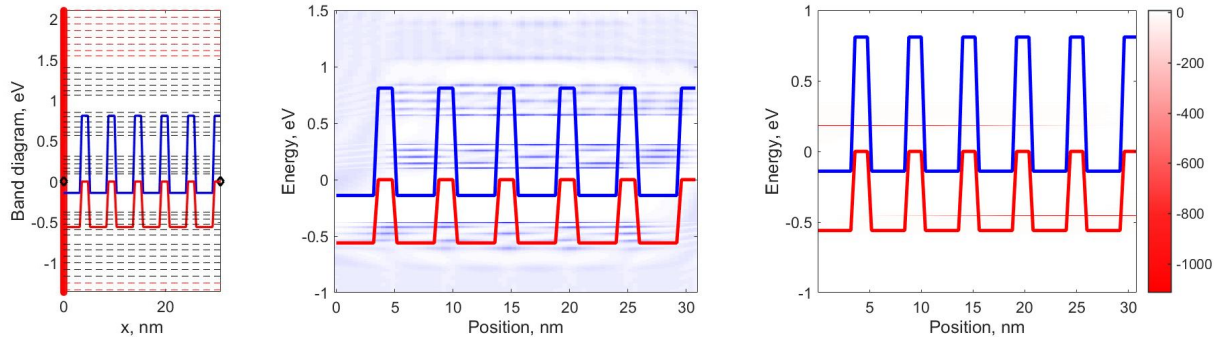

(a) (b) (c)

Figure 3-21: *(a) Band structure of the five-period SL at zero bias, with the eigenenergies of the noninteracting Hamiltonian $\boldsymbol{H}_0$ (dashed lines). Energies belonging to the near (remote) basis are shown in black (red). (b) LDOS at vanishing transverse momentum ($k_{||} = 0$). (c) Spectrally resolved photocurrent density, for the device illuminated with monochromatic light of $\hbar\omega_{op} = 0.64$ eV. Electron-phonon interactions were not included in this simulation.*

real space basis in order to be able to compute physical observables, as the basis functions are eigenstates of the position operator, interpretation of the results becomes difficult in the reduced-order space. The reduced order model here described proved to be very efficient, reducing the computation time and memory requirements and allowing analysis of big structures, difficult to analyze before. Figure **3-21** shows the results of a simulation performed with the ROM ($n_{eig} = 30$) using a 2×2 $\mathbf{k} \cdot \mathbf{p}$ basis. The simulation was performed on the five-period T2SL described in the previous section, with a monochromatic light source of $\hbar\omega_{op} = 0.64$ eV illuminating the device. As can be seen when comparing figures 3.21(b) and 3.12(a), the results are very similar. In this case, just electron-photon interactions were considered, and figure 3.21(c) reveals that the simulation was able to reproduce the v_1-c_5 obtained previously with the full TB model in figure 3.13(e) at this same photon energy. Additionally, figure 3.21(a) shows the energy eigenmodes of the noninteracting Hamiltonian (dashed lines) with the modes belonging to the near basis plotted in black.

Figure 3.22(a) show a comparison of the total current computed with the real space basis, the ROM and the LRA model. It can be seen that neglecting the effect of the remote basis clearly produce strong variations the computed NEGF current, violating current conservation. On the other hand the present approach (ROM) is capable of approximating with very good agreements the full real basis simulation while reducing the computation time. This is seen in figure 3.22(b) where the time per inner iteration is plotted for a 20 iteration inner loop with both real basis and ROM. With the ROM the time per iteration was reduced by a factor of approximately 10, and it can be further reduced by setting n_{eig} to lower values (3.21(a) shows that the energy range spanned by the eigenenergies of the near basis is fairly enough

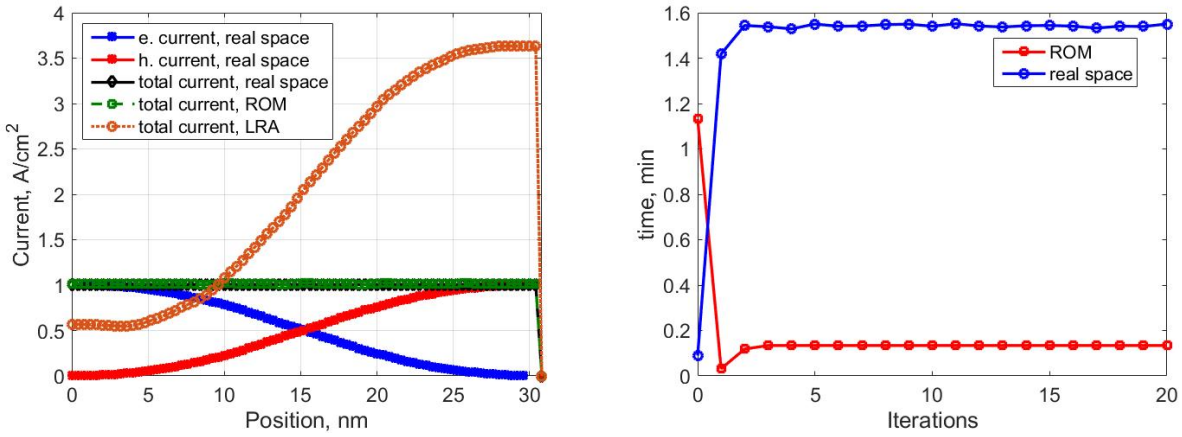

(a) (b)

Figure 3-22: *(a) Total current computed in the real space basis, in the present ROM approach and with the LRA approach proposed in [30]. (b) Comparison of the computation time spent with both real space and modal basis, to perform 20 inner iteration.*

to cover the energy range of interest, so this parameter can be further slightly reduced).

3.5.2. Pulay mixing method to improve inner loop convergence

Apart from the many issues arising from the computational complexity of the NEGF approach, another major problem is the one related with the convergence of the results. Being the Dyson's equation (2-44) a nonlinear equation, convergence in many cases can be very slow or even not guaranteed, so the method applied to solve this equation can greatly impact in the final computation time.

Solving the Dyson's equation by means of the inner loop is equivalent to solving the fixed point problem

$$\mathbf{G}^R = f(\mathbf{G}^R, \mathbf{G}^<)^4, \quad \mathbf{G}^< = g(\mathbf{G}^R, \mathbf{G}^<), \tag{3-9}$$

where f and g are nonlinear functions that compress all the dependencies on scattering self-energies, Dyson's and Keldish equations contained in the inner loop.

In the way the NEGF algorithm is implemented, the previous problem is solved by the *fixed point iteration* method (FPI), in which output Green's function for at iteration k is computed as the simple evaluation of the function f at the previous iteration, e.i. $\mathbf{G}^R_k = f(\mathbf{G}^R_{k-1}, \mathbf{G}^<_{k-1})$.

[4]Remember that only two of the Green's functions are indepenedent. Dependence here is written just in terms of G^R and $G^<$, but could be equivalently written in terms of G^A and $G^>$.

Although FPI is simple, it can result very slow in many cases and it worth to look for better options that can improve the performance of the algorithm.

The Pulay mixing method, also called *direct inversion in the iterative subspace* (DIIS), was first proposed by Peter Pulay in [31, 32], in order to improve convergence in SCF minimization problems for quantum chemistry, specifically in the procedure of minimization of the energy functional to find ground states of a quantum system. Nevertheless, its use has extended to solving vector equations, and some attempts have been done to use it in the solution of the Dyson's equation for particular cases of the interaction self-energies, like the case exposed by *Thygesen et al.* in [33], in which the solution is restricted to the GW self-energy for molecular transport. For our case, we will take the approach followed by *Banerjee et al.* in [34], in which a periodic Pulay mixing scheme is proposed by alternating periodically between FPI and conventional Pulay mixing.

We start considering equations (3-9) for which we want to find a solution, and for simplicity we define vectors $\mathbf{g}^R$ and $\mathbf{g}^<$ which result from the projection of the four-dimensional $\mathbf{G}^{R,<}$ matrices into $\mathbb{R}^M$, with $M = N \times N \times N_k \times N_E$, such that

$$\{\mathbf{G}^{R,<}(\mathbf{k}_l, E_n)\}_{i,j} \rightarrow \{\mathbf{g}^{R,<}\}_{i+N\times j+N_k\times l+N_E\times n}, \tag{3-10}$$

with $i, j = 1 \dots N$, $l = 1 \dots N_k$, $n = 1 \dots N_E$.

The residual functions are defined in the following way

$$r(\mathbf{g}^R, \mathbf{g}^<) = f(\mathbf{g}^R, \mathbf{g}^<) - \mathbf{g}^R, \quad \bar{r}(\mathbf{g}^R, \mathbf{g}^<) = g(\mathbf{g}^R, \mathbf{g}^<) - \mathbf{g}^<. \tag{3-11}$$

where we have assumed that equation (3-9) is also valid for the M-dimensional vectors $\mathbf{g}^{R,<}$.

The main idea of Pulay mixing is to combine the Green's functions at iteration k with the ones of the previous m iterations in order to find an optimal value $\mathbf{g}^R_{k+1}$ that minimizes the quantities $||r_{k+1}||$ and $||\bar{r}_{k+1}||$, with m called the size of the mixing memory. Since all the variables are now vector quantities, the previous norm is well defined as the typical 2-norm of a vector such that $||\mathbf{g}^R|| = \sqrt{(\mathbf{g}^R)^* \cdot \mathbf{g}^R}$.

On each iteration, the new[5] Green's function will be computed as

$$\mathbf{g}^R_{k+1} = \mathbf{g}^R_k + C_k f_k \tag{3-12}$$

with

[5]Here, for new Green's function we refer to the input Green's function that will be used to compute the scattering self-energies, which are then used to recompute the Green's function being this the result of the evaluation of the function f.

$$C_k = \begin{cases} \alpha\mathbb{1} & if \quad \frac{k+1}{p} \notin \mathbb{N} \\ \\ \alpha\mathbb{1} - (\mathbf{R}_k + \alpha\mathbf{F}_k)\Gamma_k & if \quad \frac{k+1}{p} \in \mathbb{N} \end{cases} \tag{3-13}$$

$\mathbf{R}_k$ and $\mathbf{F}_k$ are $M \times m$ matrices denoting the iterate and residual histories, defined in the following way

$$\mathbf{R}_k = [\Delta\mathbf{g}^R_{k-m+1} \quad \Delta\mathbf{g}^R_{k-m+2} \ \ldots \ \Delta\mathbf{g}^R_k], \qquad \mathbf{g}^R_k = \mathbf{g}^R_k - \mathbf{g}^R_{k-1} \tag{3-14a}$$

$$\mathbf{F}_k = [\Delta r_{k-m+1} \quad \Delta r_{k-m+2} \ \ldots \ \Delta r_k], \qquad \Delta r_k = r_k - r_{k-1} \tag{3-14b}$$

α is the damping parameter, p is the period of the Pulay mixing, and $\Gamma_k \in \mathbb{R}^M$ is the vector of optimal coefficients that minimize the next iteration residual $||r_{k+1}||$, which can be shown to be the solution of the matrix equation

$$\mathbf{F}^\dagger_k\mathbf{F}_k\Gamma_k = \mathbf{F}^\dagger_k f_k. \tag{3-15}$$

It can be seen from (3-13) that Pulay mixing is applied whenever the iteration is a multiple of the period p. Classical Pulay is obtained the parameter $p = 1$ and FPI when $p \to \infty$. Its also important to mention that the matrix $\mathbf{F}^\dagger_k\mathbf{F}_k$ become singular in many cases after few iterations, so some rows need to be removed in order to solve equation (3-15). Singular Value Decomposition (SVD) results to be very useful in this case to selectively remove the rows corresponding to the smallest singular values. The algorithm is summarized in figure **3-23**, and should be applied to both $\mathbf{g}^R$ and $\mathbf{g}^<$.

The main drawback present in this convergence scheme is that four new matrices need to be stores (two for $\mathbf{g}^R$ and two for $\mathbf{g}^<$), whose dimension can become very large depending on the value of M (which in turn depend on the spatial dimension of the device, energy and momentum discretization), and the amount of memory m that is desired to store. In fact, the more past values one store, the bigger the memory requirements of this approach, but as it will become clear in a while, this does not mean better convergence properties, but depend on the specific problem that is going to be solved. A value of $m = 3$ seems to be in general a good choice for the Pulay memory. Taking into account the previous consideration, a simple example is required to test the validity of this approach, and it can be extended after to more complex setups. In this case we chose to consider a simple quantum well *n-i-n* structure (see figure **3-24**) with few point to run a NEGF simulation for a single energy $E_p = 0.7$ eV and momentum $\mathbf{k}_p = (15 \times 10^6, 0)$ m^{-1}. Concerning the self-energy included, the *momentum relaxing Golizadeh self-energy* ($d_m = 10^{-2}$ eV^2) was used due to its simplicity. The Golizadeh self-energy is a phenomenological approach first

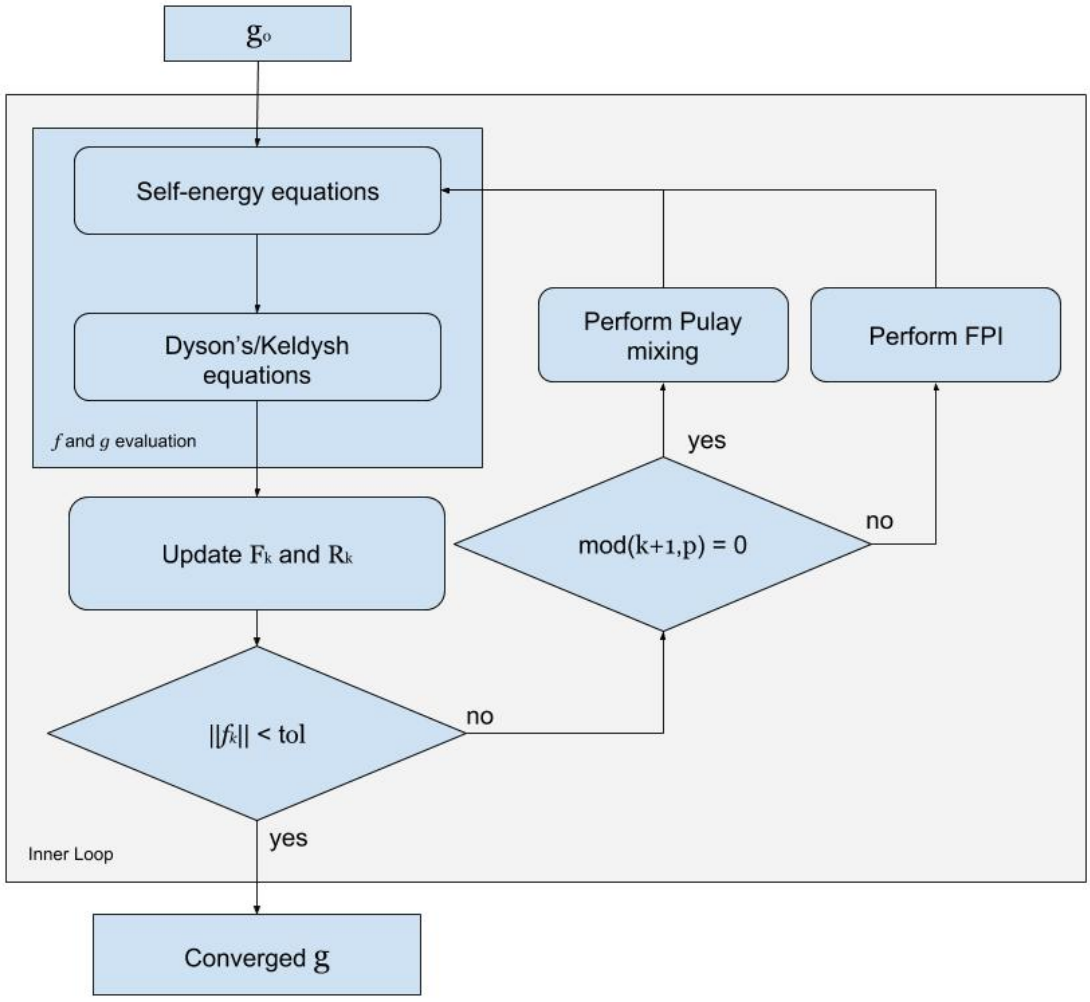

Figure 3-23: *Computational scheme of the periodic Pulay mixing method applied to the inner loop.*

introduced by *Golizadeh and Datta* [35] to model phase or momentum relaxing scattering situations. Retarded and lesser/greater components of the self-energy can be written in the following way [35, 18]

$$\Sigma^{(p)R} = d_p \mathbf{M}\mathbf{G}^R\mathbf{M}, \quad \Sigma^{(p)\lessgtr} = d_p \mathbf{M}\mathbf{G}^{\lessgtr}\mathbf{M} \tag{3-16a}$$

$$\Sigma^{(m)R} = d_m \sum_{\gamma} \{\mathbf{M}\}_{\alpha,\gamma}\{\mathbf{G}^R\}_{\gamma,\gamma}\{\mathbf{M}\}_{\gamma,\beta}, \quad \Sigma^{(m)\lessgtr} = d_m \{\mathbf{M}\}_{\alpha,\gamma}\{\mathbf{G}^{\lessgtr}\}_{\gamma,\gamma}\{\mathbf{M}\}_{\gamma,\beta} \tag{3-16b}$$

where p and m denote pure phase relaxing or phase and momentum relaxing scattering, respectively, and $d_{p,m}$ is the scattering strength that has units of square energy.

The main advantage of Golizadeh self-energy is that decouples Green's functions from at

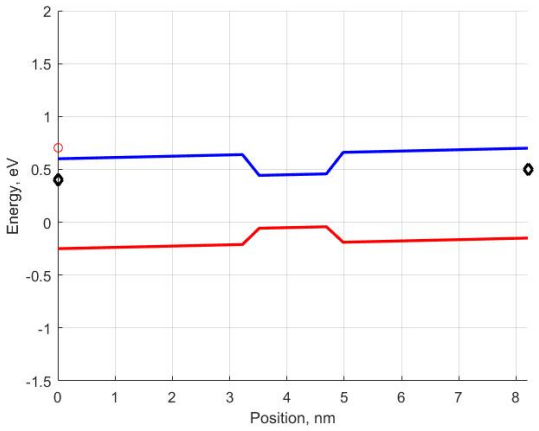

Figure 3-24: *Example device used for the NEGF simulation with Pulay optimization. Contact Fermi levels are labeled with a diamond ($\mu_L = 0.4$ V, $\mu_R = 0.5$ V), and the single energy used for the calculation is marked with a red circle at the left side. The structure is under a small applied bias of 0.1 V.*

different energies (which is not the case of photon/phonon scattering), and does not require to perform sums over momentum, hence allowing to perform computation at particular energy and momentum values. The parameters used for this simulation are shown in table **3-5**.

Table 3-5: Parameters used in the example problem for Pulay mixing.

	Parameter	Barrier	Well	Unit
Bandgap energy	E_g	0.85	0.5	eV
Conduction band offset	ΔE_c	0.0	0.2	eV
Valence band offset	ΔE_v	0.0	0.15	eV
Electron effective mass	m_e	0.0879	0.067	m_0
Hole effective mass	m_h	0.1024	0.082	m_0
static dielectric constant	ϵ	12.2	13.1	ϵ_0
High frequency dielectric constant	ϵ_∞	10.9	10.9	ϵ_0

Periodic Pulay mixing proved to be in general much better than the simple FPI convergence. Several combinations of parameters can be made, with respect to the choice of α, m and p, and not necessarily more memory m implies better convergence (see figure 3.25(a)). The damping parameter α can be chosen to either improve convergence ($\alpha \approx 1$) or make it slower ($\alpha < 1$), something that can be useful in problems in which convergence cannot be achieved with normal FPI (NEGF simulations does not have in general this issue provided that a proper initial Green's function is chosen).

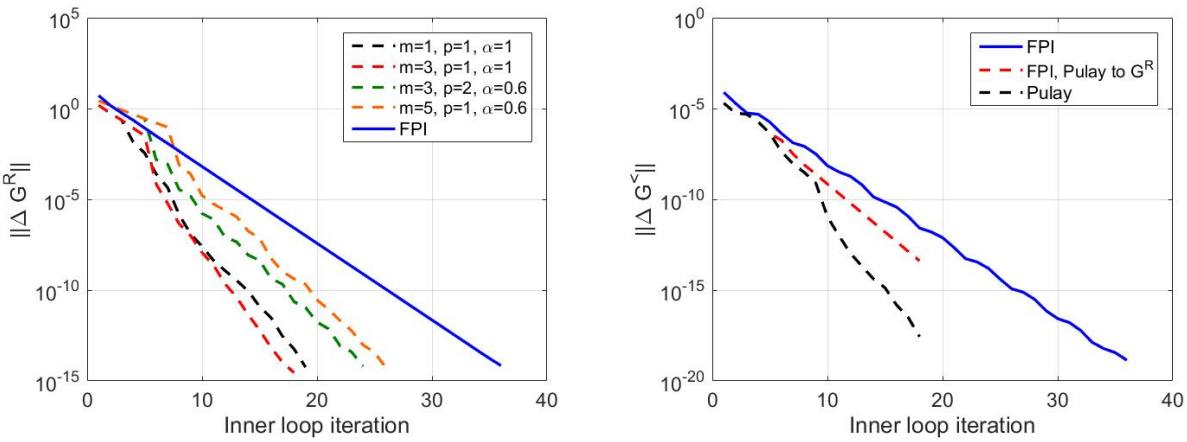

(a) (b)

Figure 3-25: *(a) Convergence of the periodic Pulay mixing for various choices of the parameters, compared with the FPI convergence. (b) Convergence of* $\boldsymbol{G}^<$ *with FPI applied to both* $\boldsymbol{G}^R$ *and* $\boldsymbol{G}^<$ *(blue), FPI applied to* $\boldsymbol{G}^<$ *when Pulay mixing is applied to* $\boldsymbol{G}^R$ *(red) and Pulay mixing applied to both Green's functions (black). In all the cases* $\alpha = 1$, $m = 3$ *and* $p = 1$.

It is also important to note that its necessary to keep track of the convergence of both G^R and $G^<$, since convergence of one does not imply the convergence of the other, as they are independent. This is the case of Golizadeh self-energy, since the manner in which this self-energy is defined make G^R independent of $G^<$, but $G^<$ is always related to the value of G^R through the Keldysh equation. When applying periodic Pulay just to G^R, this becomes clear, as $G^<$ take more iterations to converge compared to the case when Pulay mixing is applied to both at the same time (see figure 3.25(b), notice that the stopping criteria is taken with $||\Delta \mathbf{g}^R|| < tol$, hence $\mathbf{g}^<$ does not necessarily converge when the loop stops). Overall, convergence and the choice of the parameters depend on the specific problem that is going to be solved, particularly in the self-energies that are included for the computation. Further study needs to be performed in this field with more complex self-energies in order to asses the improvements given by the Pulay method.

Chapter 4

Conclusions and Outlook

In this thesis, a first step was taken by defining a strong and solid theory to describe nanostructured devices. The theoretical framework offered by the NEGF formalism results powerful due to its capability to couple carrier transport and optoelectronic phenomena into a set of self-consistent equations. Moreover, it provides a reliable tool to model realistic devices that has not been achieved before by CAD tools, since it relies on nonequilibrium quantum statistical mechanics without the use of fitting parameters, but just parameters describing the geometrical, electrical and optical characteristics of the constituent materials of the nanostructure. However, the fact that is very accurate comes with the disadvantage of its high computational burden, which make it unpractical to simulate structures longer than few hundreds of nanometers. There is also a degree of freedom in choosing the basis set that will be used to discretize the set of equations of the NEGF algorith, and two of the most popular were documented here: the tight binding approach in which eigenfunctions of the nanostructure are written as linear combination of planar orbitals, and the $\mathbf{k} \cdot \mathbf{p}$ approach, in which wavefunctions are written as sum of zone center Bloch functions, combined with a finite element discretization of the space. Tight binding results to be more accurate in the sense that is an atomistic model, capable of performing full-Brillouin zone simulation, though it is more resource demanding since imposes a spatial discretization corresponding with the atomic layers of the nanostructure. On the other hand, $\mathbf{k} \cdot \mathbf{p}$ gives freedom in the choice of the spatial discretization, but restricting the simulation to a range in reciprocal space close to the center minimum, because of how the basis set is constructed.

Several examples were studied to test the present implementation of the NEGF algorithm. First, a quantum well *p*-*i*-*n* diode was simulated with variated bias and illumination conditions. Study of the spectrally resolved density of states allowed to observe interference patterns produced by the superposition of incoming and reflected electron wavefuctions. The presence of the well noticeably affected the energetic distribution of the state pattern. It was also particularly useful to recognize the energies in which quasi-confined states were located, helping to detect transitions in which the absorption, and therefore the photocur-

rent increased, due to the increment in the availability of possible optical transitions. The spectrally resolved current density was also used to study this device, showing a predominantly ballistic behavior of carrier transport due to the extremely reduced dimensions, with optical phonon scattering producing an almost imperceptible broadening of the spectral distribution of current transmitting channels. Extreme contacts doping created a pronounced band bending and a strong built-in electric field, which favored escape of carriers from the well at low bias voltage. This was observed when the device was illuminated with photon energies slightly above the absorption edge, where escape of electrons and holes from the well was done mainly through Fowler-Nordheim tunneling and less due to thermal emission. Broadening of quasi-confined levels was also larger at low bias, showing a smaller lifetime of the carriers confined in the wells. Increasing photon energy made also possible for electrons to reach higher energy subbands, in which escape was mainly through emission above the barrier. In general, the study of this structure was useful to understand how photogenerated carriers escape from a quantum well, and how this escape is favored by the applied bias.

As a second example, a type-II superlattice absorber was analyzed, mainly focusing on observing the miniband formation process and the different optical transitions available for incoming photons af variated energy. Again the observation of the spectrally resolved local density of states and current density served to understand the device behavior. Unlike the previous structure quantum wells were deep for the electrons to easily scape by thermal emission. Nevertheless, proximity of the wells allowed the quasi-bond states to couple, producing continuous states along the structure that served as scape channels for photogenerated electrons. Geometrical parameters of the structure were variated showing that the effective bandgap of the absorber can be changed regardless of the real gap of the two constituent materials, and the structure can be used to detect light in the mid-IR range.

As a last example, we perform a rigorous approach for the simulation of interband tunneling, where direct and phonon assisted components are included into the analysis. A Bulk, heavily doped tunnel junction was simulated, in which strong band bending created quasi-confined states close to the junction, and energy overlapping gave the possibility for electrons to directly tunnel from conduction to valence band. Inclusion of phonon scattering was shown to be necessary for electrons to reach available tunneling channels and hence obtain realistic results. For small bias, current present a resonant behavior due to alignment of confined levels in valence and conduction band, and at some point, further increase in the current leads the device to a negative differential resistance (NDR) region, because of the small band overlapping. Inclusion of a double quantum well inside the junction showed to increase the performance of the device, by decreasing the effective barrier length and increasing the overlapping range. Moreover, quasi-bond states in the wells created stronger current peaks compared to the bulk case and increased the NDR performance. This structure showed to be suitable for coupling of electron and hole currents in multi-solar cells arrays.

A final part was presented including two methods to enhance the performance of the present implementation of the NEGF algorithm. The first method consisted in a novel approach to reduce the high computational burden of NEGF, based on the *low rank approximation* method, called reduced order model. The method consist in the reduction of the discretization basis used in the NEGF simulation by selectively choosing a subset of the eigenfunction of the noninteracting Hamiltonian, and then moving the NEGF equations to this new basis. The basis functions are used to diagonalize the position operator in order to obtain maximally localized, orthogonal basis functions, and an extra self-energy term is included in the simulation to account for the set of discarded basis function. This model was used to simulate the type-II superlattice, obtaining good agreement with previously obtained results and showing a decrease of 10 times in the time per inner iteration. Further decrease in the simulation time can be achieved by slightly reducing the basis size. The model proved also to be superior to the LRA model since is capable of reducing the computation time without violating current conservation.

The second approach consisted in a implementation of the Pulay method adapted to the present work, with the goal of improving convergence properties of the inner loop. The method, originally presented for minimization of vectorial equations, was adapted to the matrix equations used in the NEGF algorithm, and tested with a simple self-energy model, showing god result respect to the typical fixed point iteration performed to solve the inner loop. So far, convergence have been achieved with half the number of iterations for the tested examples, and with smaller values of the residual achieved. Further works are being tested for complex structures with realistic phonon and photon self-energies.

In general, the present implementation showed to be a reliable approach to simulate planar structures with arbitrary band alignment and bias conditions. However, further mechanisms need to be added in order to address in a more realistic way the simulation of optoelectronic devices. In future works, effects like alloy disorder and complex self-energy like nonradiative recombination processes are expected to be implemented. With the help of the provided methods for the algorithm improvement, complex structures will be simulated within a more realistic, multi-band approach.

Appendix A

Carrier interaction with photons and phonons

In this sections the derivation of the electron-photon self energy is presented, based on what is exposed in [36] and the results presented in [37]. The derivation will be restricted to the case of an orthogonal basis, e.i. tight binding, but a similar procedure for the $\mathbf{k}\cdot\mathbf{p}$ case is presented in [18]. Interaction with phonons is analogous and should be obtained in a similar way.

A.1. Interaction Hamiltonian and perturbation expansion

Interaction of electrons with photons and phonons (and, in a more general sense, with boson), is described by the following perturbation Hamiltonian in second quantization [10],

$$H^i(t) = \sum_{\nu,\mu}\sum_{\mathbf{k},\mathbf{q}} \mathbf{M}_{\nu,\mu}(\mathbf{k},\mathbf{q})\hat{c}^\dagger_{\nu,\mathbf{k}}(t)\hat{c}_{\mu,\mathbf{k}-\mathbf{q}_{||}}(t)\left[\hat{b}_{\mathbf{q}}(t)+\hat{b}^\dagger_{-\mathbf{q}}(t)\right] \tag{A-1}$$

where $\mathbf{k}$ is the transversal electron wavevector, $\mathbf{q}$ is the 3D photon wavevector, $\nu=(\alpha,L)$, $\mu=(\alpha',L')$ for the case of tight binding; $\hat{b}^\dagger_{\mathbf{q}}$ and $\hat{b}_{\mathbf{q}}$ are the bosonic creation and annihilation operators, respectively; $\hat{c}^\dagger_{\nu,\mathbf{k}}$ and $\hat{c}_{\nu,\mathbf{k}}$ are the fermionic creation and annihilation operator written in our finite basis, respectively, and $\mathbf{M}(\mathbf{k},\mathbf{q})$ is the coupling matrix between bosons and fermions.

The perturbation Hamiltonian in (A-1) should be inserted in (2-4) and the exponential term expanded in a series, providing a perturbative expansion of the Green's function for interactions of the photon/phonon-electron type. The second order contribution term of the expansion reads (first order terms vanish as they are proportional to $\langle b\rangle = \langle b^\dagger\rangle = 0$)

$$G^{(2)}(\mathbf{r},t;\mathbf{r}',t') = \left(\frac{-i}{\hbar}\right)^3 \frac{1}{2} \langle \hat{T}_C \left\{ \int_C ds \int_C ds' H^i(s) H^i(s') \hat{\Psi}_{H_0}(\mathbf{r},t) \hat{\Psi}^\dagger_{H_0}(\mathbf{r}',t') \right\} \rangle \tag{A-2}$$

where the equilibrium ensemble average has been dropped for simplicity $\langle \dots \rangle \equiv \langle \dots \rangle_0$. Taking into account expressions (2-34a) and (2-34b) for the field operators $\hat{\Psi}_{H_0}$ and $\hat{\Psi}^\dagger_{H_0}$ in the (orthogonal) basis $\{\phi_\nu(\mathbf{r})\}$, the Green's function in the specified basis gives

$$\begin{aligned} G^{(2)}_{\nu,\mu}(\mathbf{k},t,t') &= \left(\frac{-i}{\hbar}\right)^3 \frac{1}{2} \langle \hat{T}_C \left\{ \int_C ds \int_C ds' H^i(s) H^i(s') \hat{c}_{\nu,\mathbf{k}}(t) \hat{c}^\dagger_{\mu,\mathbf{k}}(t') \right\} \rangle \\ &= \left(\frac{-i}{\hbar}\right)^3 \frac{1}{2} \langle \hat{T}_C \left\{ \int_C ds \int_C ds' \sum_{\nu_1,\nu_2} \sum_{\mu_1,\mu_2} \sum_{\mathbf{k}_1,\mathbf{k}_2} \sum_{\mathbf{q}_1,\mathbf{q}_2} \mathbf{M}_{\nu_1,\mu_1}(\mathbf{k}_1,\mathbf{q}_1) \right. \\ &\quad \times \mathbf{M}_{\nu_2,\mu_2}(\mathbf{k}_2,\mathbf{q}_2) \left[\hat{b}_{\mathbf{q}_1}(s) + \hat{b}^\dagger_{-\mathbf{q}_1}(s) \right] \left[\hat{b}_{\mathbf{q}_2}(s') + \hat{b}^\dagger_{-\mathbf{q}_2}(s') \right] \\ &\quad \left. \times \hat{c}^\dagger_{\nu_1,\mathbf{k}_1}(s) \hat{c}_{\mu_1,\mathbf{k}_1-\mathbf{q}_{1||}}(s) \hat{c}^\dagger_{\nu_2,\mathbf{k}_2}(s') \hat{c}_{\mu_2,\mathbf{k}_2-\mathbf{q}_{2||}}(s') \hat{c}_{\nu,\mathbf{k}}(t) \hat{c}^\dagger_{\mu,\mathbf{k}}(t') \right\} \rangle. \end{aligned} \tag{A-3}$$

Now, we can apply Wick-Matsubara theorem to factor the electron field operators product. The photon operator product become [36]

$$\begin{aligned} &\langle \hat{T}_C \left\{ \left[\hat{b}_{\mathbf{q}_1}(s) + \hat{b}^\dagger_{-\mathbf{q}_1}(s) \right] \left[\hat{b}_{\mathbf{q}_2}(s') + \hat{b}^\dagger_{-\mathbf{q}_2}(s') \right] \right\} \rangle \\ &= \langle \hat{T}_C \left\{ \hat{b}_{\mathbf{q}_1}(s) \hat{b}^\dagger_{-\mathbf{q}_2}(s') \right\} \rangle + \langle \hat{T}_C \left\{ \hat{b}_{\mathbf{q}_2}(s') \hat{b}^\dagger_{-\mathbf{q}_1}(s) \right\} \rangle \\ &= \langle \hat{T}_C \left\{ \hat{b}_{\mathbf{q}_1}(s) \hat{b}^\dagger_{\mathbf{q}_1}(s') \right\} \rangle + \langle \hat{T}_C \left\{ \hat{b}_{-\mathbf{q}_1}(s') \hat{b}^\dagger_{-\mathbf{q}_1}(s) \right\} \rangle, \end{aligned} \tag{A-4}$$

where products involving two creators or two annihilators vanish from the sum. In (A-4) we have used that, due to the absence of interactions, the photon modes should be conserved, giving

$$\langle \hat{T}_C \left\{ \hat{b}_{\mathbf{q}_1}(s) \hat{b}^\dagger_{-\mathbf{q}_2}(s') \right\} \rangle \propto \delta_{\mathbf{q}_1,-\mathbf{q}_2}. \tag{A-5}$$

with $\delta_{\mathbf{q}_1,-\mathbf{q}_2}$ the Kronecker delta function.

There are two possible ways of factorizing the electron operator product in (A-3) which are equivalent, canceling out the factor 1/2. Choosing one of this factorizations one obtains [10, 36]

$$
\begin{aligned}
&\langle \hat{T}_C \left\{ \hat{c}^\dagger_{\nu_1,\mathbf{k}_1}(s)\hat{c}_{\mu_1,\mathbf{k}_1-\mathbf{q}_{1||}}(s)\hat{c}^\dagger_{\nu_2,\mathbf{k}_2}(s')\hat{c}_{\mu_2,\mathbf{k}_2-\mathbf{q}_{2||}}(s')\hat{c}_{\nu,\mathbf{k}}(t)\hat{c}^\dagger_{\mu,\mathbf{k}}(t') \right\}\rangle \\
&= -\langle \hat{T}_C \left\{ \hat{c}_{\nu,\mathbf{k}}(t)\hat{c}^\dagger_{\nu_1,\mathbf{k}_1}(s) \right\}\rangle \langle \hat{T}_C \left\{ \hat{c}_{\mu_2,\mathbf{k}_2-\mathbf{q}_{2||}}(s')\hat{c}^\dagger_{\nu_2,\mathbf{k}_2}(s') \right\}\rangle \langle \hat{T}_C \left\{ \hat{c}_{\mu_1,\mathbf{k}_1-\mathbf{q}_{1||}}(s)\hat{c}^\dagger_{\mu,\mathbf{k}}(t') \right\}\rangle \\
&\quad + \langle \hat{T}_C \left\{ \hat{c}_{\nu,\mathbf{k}}(t)\hat{c}^\dagger_{\nu_1,\mathbf{k}_1}(s) \right\}\rangle \langle \hat{T}_C \left\{ \hat{c}_{\mu_1,\mathbf{k}_1-\mathbf{q}_{1||}}(s)\hat{c}^\dagger_{\nu_2,\mathbf{k}_2}(s') \right\}\rangle \langle \hat{T}_C \left\{ \hat{c}_{\mu_2,\mathbf{k}_2-\mathbf{q}_{2||}}(s')\hat{c}^\dagger_{\mu,\mathbf{k}}(t') \right\}\rangle \\
&= -i\hbar G^0_{\nu,\nu_1}(\mathbf{k};t,s)\delta_{\mathbf{k},\mathbf{k}_1}\, i\hbar G^0_{\mu_2,\nu_2}(\mathbf{k}_2;s',s')\delta_{\mathbf{k}_2-\mathbf{q}_{2||},\mathbf{k}_2}\, i\hbar G^0_{\mu_1,\mu}(\mathbf{k};s,t')\delta_{\mathbf{k}_1-\mathbf{q}_{1||},\mathbf{k}} \\
&\quad + i\hbar G^0_{\nu,\nu_1}(\mathbf{k};t,s)\delta_{\mathbf{k},\mathbf{k}_1}\, i\hbar G^0_{\mu_1,\nu_2}(\mathbf{k}_2;s,s')\delta_{\mathbf{k}_1-\mathbf{q}_{1||},\mathbf{k}_2}\, i\hbar G^0_{\mu_2,\mu}(\mathbf{k};s',t')\delta_{\mathbf{k}_2-\mathbf{q}_{2||},\mathbf{k}}. \qquad \text{(A-6)}
\end{aligned}
$$

where we have used the definition of the noninteracting Green's function defined in equation (2-15) (expressed in our finite basis)

$$
G^0_{\nu,\mu}(\mathbf{k},t,t') = -\frac{i}{\hbar}\langle \hat{T}_C \left\{ \hat{c}_{\nu,\mathbf{k}}(t)\hat{c}^\dagger_{\mu,\mathbf{k}}(t') \right\}\rangle. \qquad \text{(A-7)}
$$

Finally, defining the noninteracting boson Green's function

$$
D_0(\mathbf{q};t,t') = -\frac{i}{\hbar}\left[\langle \hat{T}_C \left\{ \hat{b}_{\mathbf{q}}(t)\hat{b}^\dagger_{\mathbf{q}}(t') \right\}\rangle + \langle \hat{T}_C \left\{ \hat{b}_{-\mathbf{q}}(t')\hat{b}^\dagger_{-\mathbf{q}}(t) \right\}\rangle \right], \qquad \text{(A-8)}
$$

and inserting (A-6) and (A-8) in (A-3) (with $\mathbf{q}_1 = -\mathbf{q}_2 = \mathbf{q}$), gives the final result

$$
\begin{aligned}
G^{(2)}_{\nu,\mu}(\mathbf{k},t,t') &= \int_C ds \int_C ds' \sum_{\nu_1,\nu_2}\sum_{\mu_1,\mu_2}\sum_{\mathbf{k}_2,\mathbf{q}} \mathbf{M}_{\nu_1,\mu_1}(\mathbf{k},\mathbf{q})\mathbf{M}_{\nu_2,\mu_2}(\mathbf{k}_2,-\mathbf{q})\, i\hbar D_0(\mathbf{q};s,s') \\
&\quad \Big[-G^0_{\nu,\nu_1}(\mathbf{k};t,s)\, G^0_{\mu_2,\nu_2}(\mathbf{k}_2;s',s')\, G^0_{\mu_1,\mu}(\mathbf{k};s,t')\delta_{\mathbf{k}_2+\mathbf{q}_{||},\mathbf{k}_2}\delta_{\mathbf{k}-\mathbf{q}_{||},\mathbf{k}} \\
&\quad + G^0_{\nu,\nu_1}(\mathbf{k};t,s)\, G^0_{\mu_1,\nu_2}(\mathbf{k}_2;s,s')\, G^0_{\mu_2,\mu}(\mathbf{k};s',t')\delta_{\mathbf{k}-\mathbf{q}_{||},\mathbf{k}_2}\delta_{\mathbf{k}_2+\mathbf{q}_{||},\mathbf{k}} \Big] \\
&= \int_C ds \int_C ds' \sum_{\nu_1,\nu_2}\sum_{\mu_1,\mu_2} \Bigg[\sum_{\mathbf{k}_2,q_z} -G^0_{\nu,\nu_1}(\mathbf{k};t,s)\, i\hbar D_0(q_z;s,s')\, \mathbf{M}_{\nu_1,\mu_1}(\mathbf{k},q_z) \\
&\quad \times G^0_{\mu_2,\nu_2}(\mathbf{k}_2;s',s')\, \mathbf{M}_{\nu_2,\mu_2}(\mathbf{k}_2,-q_z)\, G^0_{\mu_1,\mu}(\mathbf{k};s,t') \\
&\quad + \sum_{\mathbf{q}} G^0_{\nu,\nu_1}(\mathbf{k};t,s)\, i\hbar D_0(\mathbf{q};s,s')\, \mathbf{M}_{\nu_1,\mu_1}(\mathbf{k},\mathbf{q})\, G^0_{\mu_1,\nu_2}(\mathbf{k}-\mathbf{q}_{||};s,s') \\
&\quad \times \mathbf{M}_{\nu_2,\mu_2}(\mathbf{k}-\mathbf{q}_{||},-\mathbf{q})\, G^0_{\mu_2,\mu}(\mathbf{k};s',t') \Big] \qquad \text{(A-9)}
\end{aligned}
$$

A.2. Electron-photon self-energy

The final expression obtained in (A-9) can be compared with the formal definition of the Dyson's equation (2-63a), leading to the self-energy term

$$\Sigma_{\nu,\mu}(\mathbf{k};t,t') = \underbrace{-i\hbar \sum_{\mathbf{k}',q_z} \mathbf{M}_{\nu,\mu}(\mathbf{k},q_z) \sum_{\nu',\mu'} \int_C ds\, D_0(q_z;t,s)\, G^0_{\mu',\nu'}(\mathbf{k}';s,s)\, \mathbf{M}_{\nu',\mu'}(\mathbf{k}',-q_z)}_{\Sigma^H_{\nu,\mu}(\mathbf{k};t,t)}$$

$$+ \underbrace{i\hbar \sum_{\nu',\mu'} \sum_{\mathbf{q}} D_0(\mathbf{q};t,t') \mathbf{M}_{\nu,\mu'}(\mathbf{k},\mathbf{q})\, G^0_{\mu',\nu'}(\mathbf{k}-\mathbf{q}_{||};t,t') \mathbf{M}_{\nu',\mu}(\mathbf{k}-\mathbf{q}_{||},-\mathbf{q})}_{\Sigma^F_{\nu,\mu}(\mathbf{k},t,t')}. \tag{A-10}$$

The self-energy in (A-10) is composed by the sum of two separate terms. In terms of a Feynman diagrammatic expansion [38, 10] this two terms correspond to the lowest order diagrams, the Hartree self-energy Σ^H (a bubble diagram is clearly recognizable in the bare propagator initiating and ending at the same point) and the Fock self-energy Σ^F. The Hartree self-energy term can be neglected in many cases (it is nonzero for the case of heterostructures) and will not be considered here [36]. In the self consistent Born approximation (SCBA) higher order perturbations terms can be automatically included in the self-energy (A-10) by replacing the noninteracting Green's function G^0 by the exact Green's function G, giving for carrier-photon Fock self-energy

$$\Sigma^F_{\nu,\mu}(\mathbf{k};t,t') = i\hbar \sum_{\nu',\mu'} \sum_{\mathbf{q}} D_0(\mathbf{q};t,t') \mathbf{M}_{\nu,\mu'}(\mathbf{k},\mathbf{q})\, G_{\mu',\nu'}(\mathbf{k}-\mathbf{q}_{||};t,t') \mathbf{M}_{\nu',\mu}(\mathbf{k}-\mathbf{q}_{||},-\mathbf{q}). \tag{A-11}$$

At this point, Lagreth rules can be applied to find lesser, greater and retarded components of the self-energy; and the resulting expression can be Fourier transformed for the steady state formulation, yielding

$$\begin{aligned}
\Sigma^{F\,\lessgtr}_{\nu,\mu}(\mathbf{k},E) &= i\hbar \sum_{\nu',\mu'} \sum_{\mathbf{q}} \int \frac{dE'}{2\pi\hbar}\, D^{\lessgtr}_0(\mathbf{q};E') \mathbf{M}_{\nu,\mu'}(\mathbf{k},\mathbf{q})\, G^{\lessgtr}_{\mu',\nu'}(\mathbf{k}-\mathbf{q}_{||};E-E') \\
&\quad \times \mathbf{M}_{\nu',\mu}(\mathbf{k}-\mathbf{q}_{||},-\mathbf{q}), && \text{(A-12a)} \\
\Sigma^{F\,R}_{\nu,\mu}(\mathbf{k},E) &= i\hbar \sum_{\nu',\mu'} \sum_{\mathbf{q}} \int \frac{dE'}{2\pi\hbar}\, \mathbf{M}_{\nu,\mu'}(\mathbf{k},\mathbf{q}) \left[D^R_0(\mathbf{q};E')\, G^R_{\mu',\nu'}(\mathbf{k}-\mathbf{q}_{||};E-E') \right. \\
&\quad \left. + D^R_0(\mathbf{q};E')\, G^<_{\mu',\nu'}(\mathbf{k}-\mathbf{q}_{||};E-E') + D^<_0(\mathbf{q};E')\, G^R_{\mu',\nu'}(\mathbf{k}-\mathbf{q}_{||};E-E') \right] \\
&\quad \times \mathbf{M}_{\nu',\mu}(\mathbf{k}-\mathbf{q}_{||},-\mathbf{q}), && \text{(A-12b)}
\end{aligned}$$

The equilibrium (steady state) photon Green's function is given by [37]

$$D_0^{\lessgtr}(\mathbf{q},E) = -2\pi i\left[N_{\mathbf{q}}\,\delta(E \mp \hbar\omega_{\mathbf{q}}) + (N_{\mathbf{q}}+1)\,\delta(E \pm \hbar\omega_{\mathbf{q}})\right], \tag{A-13a}$$

$$D_0^{R,A}(\mathbf{q},E) = \frac{1}{E - \hbar\omega_{\mathbf{q}} \pm i\eta} - \frac{1}{E + \hbar\omega_{\mathbf{q}} \pm i\eta}. \tag{A-13b}$$

Substituting (A-13a) and (A-13b) into (A-12b) and (A-12a), and integrating over energy, gives the final result for the lesser, greater and retarded electron-photon self-energies

$$\Sigma^{F\,\lessgtr}(\mathbf{k},E) = \sum_{\mathbf{q}} \mathbf{M}(\mathbf{k},\mathbf{q})\,\left[N_{\mathbf{q}}G^{\lessgtr}(\mathbf{k}-\mathbf{q}_{||},E \mp \hbar\omega_{\mathbf{q}}) + (N_{\mathbf{q}}+1)G^{\lessgtr}(\mathbf{k}-\mathbf{q}_{||},E \pm \hbar\omega_{\mathbf{q}})\right] \times \mathbf{M}(\mathbf{k}-\mathbf{q}_{||},-\mathbf{q}), \tag{A-14a}$$

$$\begin{aligned}\Sigma^{F\,R}(\mathbf{k},E) = \sum_{\mathbf{q}} \mathbf{M}(\mathbf{k},\mathbf{q})\,&\left[(N_{\mathbf{q}}+1)G^{R}(\mathbf{k}-\mathbf{q}_{||},E-\hbar\omega_{\mathbf{q}}) + N_{\mathbf{q}}G^{R}(\mathbf{k}-\mathbf{q}_{||},E+\hbar\omega_{\mathbf{q}})\right.\\ &+\frac{1}{2}\left(G^{<}(\mathbf{k}-\mathbf{q}_{||},E-\hbar\omega_{\mathbf{q}}) - G^{<}(\mathbf{k}-\mathbf{q}_{||},E+\hbar\omega_{\mathbf{q}})\right)\\ &\left.+i\mathcal{P}\left\{\int\frac{dE'}{2\pi}\left(\frac{G^{<}(\mathbf{k}-\mathbf{q}_{||},E-E'}{E'-\hbar\omega_{\mathbf{q}}} - \frac{G^{<}(\mathbf{k}-\mathbf{q}_{||},E-E')}{E'+\hbar\omega_{\mathbf{q}}}\right)\right\}\right]\\ &\times \mathbf{M}(\mathbf{k}-\mathbf{q}_{||},-\mathbf{q})\\ &= \frac{1}{2}\left(\Sigma^{F\,>}(\mathbf{k},E) - \Sigma^{F\,<}(\mathbf{k},E)\right) - i\mathcal{P}\left\{\int dE'\frac{\Sigma^{F\,<}(\mathbf{k},E') - \Sigma^{F\,>}(\mathbf{k},E')}{E-E'}\right\},\end{aligned} \tag{A-14b}$$

where everything have been written in full matrix notation. The integration leading to (A-14b) involves the use of the *Cauchy's principal value theorem* [10].

Bibliography

[1] "International technology roadmap for semiconductor (ITRS) 2.0, executive report," 2013.

[2] P. Vogl and T. Kubis, "The non-equilibrium Green's function method: an introduction," *J. Comp. Electron.*, vol. 9, no. 3, pp. 237–242, 2010.

[3] M. Kira and S. W. Koch, "Many-body correlations and excitonic effects in semiconductor spectroscopy," *Progress Quantum Electron.*, vol. 30, no. 5, pp. 155–296, 2006.

[4] L. V. Keldysh, "Real-time nonequilibrium Green's functions," in *Progress in Nonequilibrium Green's Functions* (M. Bonitz and D. Semkat, eds.), (New Jersey), pp. 4–17, World Scientific, 2003.

[5] E. O. Kane, "The $k \cdot p$ method," in *Physics of III–V Compounds* (R. K. Willardson and A. C. Beer, eds.), vol. 1 of *Semiconductors and Semimetals*, ch. 3, pp. 75–100, New York: Academic Press, 1966.

[6] N. Marzari, A. A. Mostofi, J. R. Yates, I. Souza, and D. Vanderbilt, "Maximally localized wannier functions: Theory and applications," *Rev. Modern Phys.*, vol. 84, no. 4, pp. 1419–1475, 2012.

[7] G. H. Wannier, "The structure of electronic excitation levels in insulating crystals," *Phys. Rev.*, vol. 52, no. 3, pp. 191–197, 2002.

[8] C. Jacoboni, *Theory of Electron Transport in Semiconductors. A Pathway from Elementary Physics to Nonequilibrium Green Functions*. Berlin: Springer-Verlag, 2010.

[9] G. D. Mahan, *Many-Particle Physics*. New York: Kluwer Academic Publishers, 3rd ed., 2000.

[10] U. Aeberhard, *A Microscopic Theory of Quantum Well Photovoltaics*. PhD thesis, Eidgenössische Technische Hochschule Zürich, 2008.

[11] L. P. Kadanoff and G. Baym, *Quantum Statistical Mechanics. Green's Function Methods in Equilibrium and Nonequilibrium Problems*. New York: W. A. Benjamin, 1962.

[12] H. Haug and A.-P. Jauho, *Quantum Kinetics in Transport and Optics of Semiconductors*. Berlin: Springer, 2nd ed., 2008.

[13] N. Vukmirovic, Z. Ikonic, D. Indjin, and P. Harrison, "Quantum transport in semiconductor quantum dot superlattices: Electron-phonon resonances and polaron effects," *Phys. Rev. B*, vol. 76, no. 24, p. 245313, 2007.

[14] P. Vogl, H. P. Hjalmarso, and J. D. Dow, "A semi-empirical tight-binding theory of the electronic structure of semiconductors," *J. Phys. Chem. Solids*, vol. 44, no. 5, pp. 365–378, 1983.

[15] Y. Wei and M. Razeghi, "Modeling of type-II InAs/GaSb superlattices using an empirical tight-binding method and interface engineering," *Phys. Rev. B*, vol. 69, no. 8, p. 085316, 2004.

[16] R. Lake, G. Klimeck, R. C. Bowen, and D. Jovanovic, "Single and multiband modeling of quantum electron transport through layered semiconductor devices," *J. Appl. Phys.*, vol. 81, pp. 7845–7869, Feb. 1997.

[17] L. C. L. Y. Voon and L. R. Ram-Mohan, "Tight-binding representation of the optical matrix elements: Theory and applications," *Phys. Rev. B*, vol. 47, no. 23, pp. 15500–15508, 1993.

[18] S. Steiger, *Modelling Nano-LEDs*. PhD thesis, Eidgenössische Technische Hochschule Zürich, 2009.

[19] Y.-C. Chang and J. N. Schulman, "Complex band structures of crystalline solids: An eigenvalue method," *Phys. Rev. B*, vol. 25, no. 6, p. 3975, 1982.

[20] S. L. Chuang, *Physics of Photonic Devices*. New Jersey: John Wiley & Sons, 2009.

[21] G. Liu and S.-L. Chuang, "Modeling of Sb-based type-II quantum cascade lasers," *Physical Review B. Condensed Matter and Materials Physics*, vol. 65, p. 165220, 2002.

[22] E. H. Li, "Material parameters of InGaAsP and InAlGaAs systems for use in quantum well structures at low and room temperatures," *Physica E*, vol. 5, no. 4, pp. 215–273, 2000.

[23] D. L. Smith and C. Mailhiot, "Theory of semiconductor superlattice electronic structure," *Rev. Modern Phys.*, vol. 62, pp. 173–234, Jan. 1990.

[24] U. Aeberhard, "Photovoltaics at the mesoscale: insights from quantum-kinetic simulation," *J. Phys. D*, vol. 51, no. 32, p. 323002, 2018.

[25] P.-F. Qiao, S. Mou, and S. L. Chuang, "Electronic band structures and optical properties of type-II superlattice photodetectors with interfacial effect," *Opt. Express*, vol. 20, no. 3, p. 2319, 2012.

[26] Z. Tian, R. T. Hinkey, R. Q. Yang, D. Lubyshev, Y. Qiu, J. M. Fastenau, W. K. Liu, and M. B. Johnson, "Interband cascade infrared photodetectors with enhanced electron barriers and p-type superlattice absorbers," *J. Appl. Phys.*, vol. 111, no. 2, p. 024510, 2012.

[27] M. P. Lumb, M. K. Yakes, M. González, I. Vurgaftman, C. G. Bailey, R. Hoheisel, and R. J. Walters, "Double quantum-well tunnel junctions with high peak tunnel currents and low absorption for InP multi-junction solar cells," *Appl. Phys. Lett.*, vol. 100, no. 21, p. 213907, 2012.

[28] U. Aeberhard, "Theoretical investigation of direct and phonon-assisted tunneling currents in InAlGaAs/InGaAs bulk and quantum-well interband tunnel junctions for multijunction solar cells," *Phys. Rev. B*, vol. 87, no. 8, p. 081302, 2013.

[29] S.-C. Lee and A. Wacker, "Nonequilibrium Green's function theory for transport and gain properties of quantum cascade structures," *Phys. Rev. B*, vol. 66, no. 24, p. 245314, 2002.

[30] L. Zeng, Y. He, M. Povolotskyi, X. Liu, G. Klimeck, and T. Kubis, "Low rank approximation method for efficient Green's function calculation of dissipative quantum transport," *J. Appl. Phys.*, vol. 113, no. 21, p. 213707, 2013.

[31] P. Pulay, "Convergence acceleration of iterative sequences. The case of SCF iteration," *Chem. Phys. Lett.*, vol. 73, no. 2, pp. 393–398, 1980.

[32] P. Pulay, "Improved SCF convergence acceleration," *J. Comp. Chem.*, vol. 3, no. 4, pp. 556–560, 1982.

[33] K. S. Thygesen and A. Rubio, "Conserving GW scheme for nonequilibrium quantum transport in molecular contacts," *Chem. Phys. Lett.*, vol. 77, no. 11, p. 11533, 2008.

[34] A. S. Banerjee, P. Suryanarayana, and J. E. Pask, "Periodic Pulay method for robust and efficient convergence acceleration of self-consistent field iterations," *Chem. Phys. Lett.*, vol. 647, pp. 31–35, 2008.

[35] R. Golizadeh-Mojarad and S. Datta, "Nonequilibrium Green's function based models for dephasing in quantum transport," *Phys. Rev. B*, vol. 75, no. 8, p. 081301, 2007.

[36] R. K. Lake and R. R. Pandey, "Non-equilibrium Green functions in electronic device modeling," *arXiv:cond-mat/0607219v1*, 2007.

[37] L. E. Henrickson, "Nonequilibrium photocurrent modeling in resonant tunneling photodetectors," *J. Appl. Phys.*, vol. 91, no. 10, pp. 6273–6281, 2002.

[38] P. Hyldgaard, S. Hershfield, J. H. Davies, and J. W. Wilkins, "Resonant tunneling with an electron-phonon interaction," *Ann. Phys.*, vol. 236, no. 1, pp. 1–42, 1994.